

Fatigue and Fracture Problems in Materials and Welds

Lambertsen, Søren Heide

DOI (link to publication from Publisher):
[10.5278/vbn.phd.engsci.00008](https://doi.org/10.5278/vbn.phd.engsci.00008)

Publication date:
2015

Document Version
Publisher's PDF, also known as Version of record

[Link to publication from Aalborg University](#)

Citation for published version (APA):
Lambertsen, S. H. (2015). *Fatigue and Fracture Problems in Materials and Welds*. Aalborg Universitetsforlag.
<https://doi.org/10.5278/vbn.phd.engsci.00008>

General rights

Copyright and moral rights for the publications made accessible in the public portal are retained by the authors and/or other copyright owners and it is a condition of accessing publications that users recognise and abide by the legal requirements associated with these rights.

- Users may download and print one copy of any publication from the public portal for the purpose of private study or research.
- You may not further distribute the material or use it for any profit-making activity or commercial gain
- You may freely distribute the URL identifying the publication in the public portal -

Take down policy

If you believe that this document breaches copyright please contact us at vbn@aub.aau.dk providing details, and we will remove access to the work immediately and investigate your claim.

FATIGUE AND FRACTURE PROBLEMS IN MATERIALS AND WELDS

**BY
SØREN HEIDE LAMBERTSEN**

DISSERTATION SUBMITTED 2015



AALBORG UNIVERSITY
DENMARK

Fatigue and Fracture Problems in Materials and Welds

Ph.D. Dissertation
Søren Heide Lambertsen

Aalborg University
Department of Civil Engineering - Division for Structures, Materials and
Geotechnics
Sofiendelsvej 9-11
9200 Aalborg, Denmark

Thesis submitted: 26. August, 2015

PhD supervisor: Prof. Lars Damkilde
Aalborg University

PhD committee: Associate Professor Lars Andersen (chairman)
Aalborg Universitet, Denmark

Professor Henrik Myhre Jensen
Aarhus University, Denmark

Professor Göran Sandberg
Lunds Tekniska Högskola, Sweden

PhD Series: Faculty of Engineering and Science, Aalborg University

ISSN (online): 2246-1248

ISBN (online): 978-87-7112-351-7

Published by:
Aalborg University Press
Skjernvej 4A, 2nd floor
DK – 9220 Aalborg Ø
Phone: +45 99407140
aauf@forlag.aau.dk
forlag.aau.dk

© Copyright: Søren Heide Lambertsen

Printed in Denmark by Rosendahls, 2015

Curriculum Vitae

Søren Heide Lambertsen



Professional Experience

June, 2014–today Assistant professor, at Aalborg University Esbjerg with research field in fatigue and fracture mechanics and supervising in finite element analysis, especially in Ansys.

2010–2014 Ph.D. Follow, at Aalborg University Esbjerg with the thesis Title “Fatigue and fracture problems in welded construction and composites”

2009–2010 Plumbing technician, part time at Svend J Schmidt Aps.

2006–2008 Project Consultant Engineer, at ANDRITZ Feed & Biofuel with main focus on designing and optimization of machines in aspect to production of Biofuel.

2005–July/August Industrial technician at Dong energy A/S, maintenance and replacement turbine and high pressure system with main, especially valves in relation to the steam systems.

2004–July/August Industrial technician at Dong energy A/S, maintenance and replacement of the main boiler in relation to the water system.

Education

2008–2010 Master of Science (MSc) in Civil Engineering and Mechanical Design, The Faculties of Engineering, Science and Medicine, Aalborg University Esbjerg, Denmark.

2005–2008 Bachelor of Science (BSc) in Civil Engineering and Mechanical Design, The Faculties of Engineering, Science and Medicine, Aalborg University Esbjerg, Denmark.

2004–2005 Access course to Higher Education Diploma in Engineering at Aalborg University Esbjerg.

2000–2004 Industrial Machine technician, Elsam A/S

Publications

Fatigue Analysis of a Point Absorber WEC subjected to Passive and Reactive Control. A. S. Zurkinden, S. H. Lambertsen, L. Damkilde, Z. Geo, T. Moan Journal of Offshore Mechanics and Arctic Engineering., Accepted manuscript posted May 19, 2015

Fatigue of thin walled tubes in copper alloy CUNI10. Søren Heide Lambertsen, Lars Damkilde and Michael S. Jepsen. Journal of Ships and Offshore Structures.

Experimental Quantification of Metallurgy Changes Induced by Laser Welding in AISI304 Stainless Steel. Lambertsen, Søren Heide; Damkilde, Lars; Ulriksen, Martin Dalgaard. I: Studies in Engineering and Technology,.

Design of Ultra High Performance Fiber Reinforced Concrete Shells. Jepsen, Michael S.; Lambertsen, Søren Heide; Damkilde, Lars. Proceedings of the 26th Nordic Seminar on Computational Mechanics. red. / Anders Logg; Kent-Andre Mardal; André Massing. Simula Research Laboratory, Norway, 2013. s. 96-99.

Estimation of Fatigue Life of Laser Welded AISI304 Stainless Steel T-Joint Based on Experiments and Recommendations in Design Codes. Lambertsen, Søren Heide; Damkilde, Lars; Kristensen, Anders Schmidt; Pedersen, Ronnie. I: World Journal of Mechanics, Vol. 3, Nr. 3, 2013, s. 178-183.

RECOMMENDED PRACTICE DNV-RP-C208 Determination of Structural Capacity by Non-linear FE analysis Methods. Coauthor at DNV Høvik.

Fatigue Analysis of a Wave Energy Converter Taking into Account Different Control Strategies. Zurkinden, Andrew Stephen; Lambertsen, Søren Heide; Damkilde, Lars; Gao, Zhen; Moan, Torgeir. ASME 2013 32nd International Conference on Ocean, Offshore and Arctic Engineering: Ocean Renewable Energy. Vol. 8 American Society of Mechanical Engineers.

Investigation of Patch Coatings Influence on the Stress Intensity Factor for Surface Cracks. Lambertsen, Søren Heide; Jepsen, Michael S.; Damkilde, Lars. Proceedings of the 26th Nordic Seminar on Computational Mechanics: Oslo, 23-25 October.

Structural Modeling and Analysis of a Wave Energy Converter. Andrew Stephen Zurkinden, Søren Heide Lambertsen, Lars Damkilde, Proceedings of the 25th Nordic Seminar on Computational Mechanics.

Awards

Esbjerg Universitetspris, 2012.

Given External courses

FEM Coause in Ansys Workbench at SDU Odense 8. Semester Civil Engineering.

Introduktion and special application in Fatigue and fracture issues at Siemens Wind power Brande.

Abstract

The subject of this thesis is fatigue and fracture mechanics in materials and welds. In the thesis, topics with relation to fracture and fatigue are described. This is done in connection to the conducted scientific work from the Ph.D. process.

The thesis treats four overall subjects, namely 1) fatigue analysis of copper (CuNi10) tubes, 2) fatigue analysis of laser welded T-joints designed in stainless steel (AISI 304), 3) metallurgical investigations of the aforementioned T-joints, and 4) investigations of using coating layer as a patch repairing method for steel and aluminum structures. As an addition, the use of numerical tools, i.e. finite element analysis (FEA), to estimate the low cycle fatigue life in accordance with the new recommendation DNV-RP-C208 is treated. The latter has been included since the author of this thesis has been involved in developing the specific DNV recommendation.

In the fatigue testing of the CuNi10 material, the examined components are pipes, which are usually applied in plate fin-and-tube heat exchangers in ship engines. The purpose of these pipes is to cool down the inlet air when it has been compressed, and thereby ensure that the inlet air is at the right temperature before it goes into the combustion chamber. When an engine starts and stops, dissimilar heating occurs for the pipe and the shell of the exchanger, resulting in straining of the pipes. Therefore, it is of interest to investigate the fatigue resistance of the pipes in a setup similar to the one in the exchanger. To obtain such setup, a glued bushing, which does not introduce stress concentrations, is used to transfer the loading to the pipes. Subsequently, the experimental results are analyzed with statistical evaluation, and in this way, a strain vs life curve is developed. Finally, an evaluation of the thermal straining-induced damage of the pipes are conducted.

The fatigue life of laser welded T-joints of stainless steel, in a thin-walled application often used in pumps, is investigated as in the case of the copper pipes. In this T-joint case, the fatigue life is evaluated by developing a stress vs life curve. The experimentally obtained result is compared with fatigue lives found using two recommendations. Furthermore, the joint is investigated with respect to the laser welded-induced metallurgical changes

to clarify the transformation that occurs by this specific welding method and the following loading. In this investigation, different methods, in the form of Lichtenegger and Bloech color etching, ferritescope, X-ray diffraction (XRD) and Vickers hardness, are employed.

In some industries, patch repairing is used to slow down crack growth and hereby avoid replacement of damaged components. It is examined whether this repairing method can be utilized as a patch coating on steel and aluminum components to effectively extend the fatigue life of these components.

Resumé

Denne afhandling omhandler udmattelse og revnemekanik i materialer og svejsninger. I selve afhandlingen gennemgås revne- og udmattelsesfænomener, og der refereres til den udførte forskning i forbindelse med Ph.D.-forløbet.

Afhandlingen omhandler overordnet set fire emner; henholdsvis 1) udmattelsesanalyse af kobberør (CuNi10), 2) udmattelsesanalyse af svejste T-samlinger konstrueret i rustfrit stål (AISI 304), 3) metallurgiske undersøgelser af de førnævnte T-samlinger og 4) undersøgelser af brugen af coating som revneforsinkelseslag for stål- og aluminiumsstrukturer. Ydermere behandles brugen af numeriske metoder, i form af finite element-analyse (FEA), til at estimere korttidsudmattelse i overensstemmelse med den nyeste norm DNV-RP-C208. Det sidstnævnte er medtaget, eftersom forfatteren af indeværende afhandling har været involveret i udviklingen af denne specifikke DNV-norm.

I udmattelsestestene af CuNi10 anvendes et rørprofil, som typisk bruges i luftladekøleren i visse skibsmotorer. Formålet med disse rør er at køle luften, efter den er blevet komprimeret, hvorved den optimale indgangstemperatur for driften af motoren opnås. Når selve motoren og kølesystemet startes eller stoppes, opvarmes rørene og motoren forskelligt, hvorfor der introduceres tøjninger i strukturen, i særdeleshed i rørene. Derfor ønskes rørenes udmattelsesstyrke undersøgt i en opsætning, som svarer til den aktuelle konfiguration. Til denne opsætning anvendes en limet bøsning, hvorved belastningerne overføres gennem forskydning, således der kun dannes ubetydelige spændingskoncentrationer. Resultatet af disse udmattelsestests analyseres ved hjælp af statistisk evaluering. Herved opstilles en tøjnings-levetidskurve, og på denne baggrund vurderes den udmattelseskade, der er genereret ved de cykliske belastninger hidrørende temeperatursvingningerne ved start og stop.

Der er udført eksperimenter for at fastlægge udmattelseslevetiden for T-svejsesøm udført ved brug af lasersvejsning i AISI 304. Her er undersøgelserne fokuseret på en tyndpladet T-konfiguration, der eksempelvis anvendes i pumpelebere. I analogi til forsøget med kobberørene analyseres udmattelsesdata, og der opstilles S-N-kurver for de pågældende konfigura-

tioner. De frembragte forsøgsresultater sammenlignes med to normer, og herved gives en reference i forhold til udmattelseslevetiden. Yderligere undersøges de metallurgiske reaktioner, som følger af laser-svejsningsprocessen, samt hvilken type af transformationer, der sker ved den efterfølgende udmattelsesbelastning. Til denne undersøgelse anvendes forskellige metoder; i form af Lichtenegger og Bloech-farveætsning, ferritskop, røntgendiffraktion (XRD) samt Vickers hårdhed.

Inden for bestemte industrier anvendes patch-reparationer til at udsætte eller undgå udskiftninger af komponenter, hvori revner er under udvikling. Denne reparationsmetode undersøges i forhold til anvendeligheden af coating på stål- og aluminiumskonstruktioner, hvor hensigten er at forlænge udmattelseslevetiden.

Contents

Curriculum Vitae	iii
Abstract	vii
Resumé	ix
Thesis Details	xv
Acknowledgements	xvii
1 Consideration about design and fatigue life	1
1 Introduction	1
2 Fatigue life, reliability and cost	1
3 Fatigue problems in practice	3
4 Estimation of the fatigue life	5
2 Theoretical fracture Mechanics	7
1 Historical review and invention of the first fracture mechanics theory	7
2 The energy criterion for cracks	9
3 Stress intensity factor	11
4 The crack tip stress field	13
5 Stress intensity factor by path or volumen integral	15
6 The equivalent stress intensity factor	16
3 Applied Fracture Mechanics	19
1 Cracks in materials and use of a fracture mechanics approach .	19
1.1 Fracture failure in structures and components	20
2 Phase 1: Crack initiation	24
2.1 Redistribution of dislocations and its influence on crack initiation	25
2.2 Slip bands and crack initiation in AISI 304	25
2.3 K_{th} according to BS7910	27

3	Phase 2: Crack growth	28
3.1	Crack growth by Paris' law	28
3.2	Crack grow direction	30
3.3	Environmental impacts on the crack growth rate	30
3.4	Metallurgical effects in the crack growth rate	31
3.5	The influence from the mean stress level and crack closing effect	32
4	Fracture toughness K_c , K_{Ic}	34
4.1	Estimation of the fracture toughness by V-notch testing	38
4	Fatigue in materials and estimation of the S-N curve	41
1	Introduction to Fatigue	41
2	Estimation of the fatigue life for non-welded materials	44
3	Fatigue life estimation by norms	51
4	Load Categorization in case of fatigue estimation	53
5	Fatigue in polymers and composites	54
5.1	The fatigue properties of polymers and environmental effect	56
5	Fatigue in steel and welds	59
1	Impact from welds on steel structures	59
2	Welding influence on the metallurgy in steel	60
2.1	Grain growth introduced by welding	61
2.2	Hydrogen cracks introduced by welds	62
3	Imperfection introduced by the welding process	63
3.1	Imperfection in laser welded joints of AISI 304	64
4	Improvement of the fatigue property in case of imperfections	64
5	Residual stresses in welds	67
6	Residual stresses and their impact on the S-N curve	69
6	Determination of structural capacity by non-linear FEA methods	71
1	Introduction to fatigue estimation by FEA	71
1.1	Local plastic strain and nonlinear material	71
1.2	Fatigue damage generated by plastic strain	73
1.3	Details of estimation by DNV-RP-C208	73
2	Low cycle fatigue analysis of tubular joint subjected to out-of-plane loading	74
2.1	The setup of the brace and chord model	74
2.2	Strain level obtained by the FE model of the brace and chord model	78
3	Low cycle fatigue analysis of other structural details	80
3.1	Example: estimation of the low cycle fatigue life for a plate with a circular hole	80

Contents

7 Conclusion	85
References	87
A Fatigue of thin walled tubes in copper alloy CuNi10	99
B Experimental Quantification of Metallurgy Changes Induced by Laser Welding in AISI304 Stainless Steel	107
C Estimation of Fatigue Life of Laser Welded AISI304 Stainless Steel T-Joint Based on Experiments and Recommendations in Design Codes	119
D Investigation of Patch Coatings Influence on the Stress Intensity Factor for Surface Cracks	127

Thesis Details

Thesis Title: Fatigue and Fracture Problems in Materials and Welds
Ph.D. Student: Søren Heide Lambertsen
Supervisors: Professor Lars Damkilde, Aalborg University

The main body of this thesis consists of the following papers.

- [A] Søren Heide Lambertsen, Lars Damkilde, Michael S. Jepsen, "Fatigue of thin walled tubes in copper alloy CuNi10," *Ships and Offshore Structures*, Accepted: 25. Nov 2014 Published online: 1. April 2015.
- [B] Søren Heide Lambertsen, Lars Damkilde, Martin Dalgaard Ulriksen, "Experimental Quantification of Metallurgy Changes Induced by Laser Welding in AISI 304 Stainless Steel," *Studies in Engineering and Technology*, vol. 1, no. 2, pp. 21–28, 2013.
- [C] Søren Heide Lambertsen, Lars Damkilde, Anders Schmidt Kristensen, Ronnie Refstrup Pedersen, "Estimation of Fatigue Life of Laser Welded AISI304 Stainless Steel T-Joint Based on Experiments and Recommendations in Design Codes.," *World Journal of Mechanics*, vol. 3, no. 3, pp. 178–183, 2013.
- [D] Søren Heide Lambertsen, Michael S. Jepsen, Lars Damkilde, "Investigation of Patch Coatings influence on the Stress intensity Factor for Surface Cracks," *Proceedings of the 26th Nordic Seminar on Computational Mechanics*, pp. 210–213, 2013.

In addition to the main papers, the following publications have also been made.

- [1] Michael S. Jepsen, Søren Heide Lambertsen, Lars Damkilde, "Design of Ultra High Performance Fiber Reinforced Concrete shells," *Proceedings of the 26th Nordic Seminar on Computational Mechanics*, pp. 96–99, 2013.
- [2] Andrew S. Zurkinden, Søren Heide Lambertsen, Lars Damkilde, Zhen Gao and Torgeir Moan, "Fatigue Analysis of a Wave Energy Converter

Taking Into Account Different Control Strategies," *ASME 2013 32nd International Conference on Ocean, Offshore and Arctic Engineering: Ocean Renewable Energy*, vol. 8 American Society of Mechanical Engineers, 2013.

- [3] Andrew S. Zurkinden, Søren H. Lambersten, and Lars Damkilde, "Structural Modeling and Analysis of a Wave Energy Converter," *Proceedings of the 25th Nordic Seminar on Computational Mechanics*, 2012.

This thesis has been submitted for assessment in partial fulfillment of the Ph.D. degree. The thesis is based on the submitted or published scientific papers which are listed above. Parts of the papers are used directly or indirectly in the extended summary of the thesis. As part of the assessment, co-author statements have been made available to the assessment committee and are also available at the Faculty. The thesis is not in its present form acceptable for open publication but only in limited and closed circulation as copyright may not be ensured.

Acknowledgements

This thesis represents the summary of my work at the Department of Civil Engineering at Aalborg University. I am thankful to many individuals who supported me during my time as a Ph.D. fellow. This time has been lucrative in forms of scientific and personal challenges, and it has been exciting to get further knowledge about the worlds of science and practicing engineering.

A special thanks to my supervisor, Professor Lars Damkilde, for his constant support and guidance throughout the process of writing this thesis. In the process of the scientific work, he has provided steady support, shared his invaluable experience and provided timely advice. I am honored to had been given the opportunity to do this Ph.D work under a good research environment.

Furthermore, thanks are given to DNV GL for allowing me to stay abroad at their headquarters in Oslo, Norway. In particular, thanks to Arne Fjeldstad for, respectively, introducing me to their approach and appertaining challenges regarding fatigue and fracture mechanics and consistent guidance even after the stay in Oslo. Also, thanks to Force Technology for providing equipment and general knowledge.

Many colleagues have contributed to this thesis. I gratefully appreciate the help and support from Martin Dalgaard Ulriksen, Michael Sandholm Jepsen, Anders Schmidt Kristensen and Ronnie Refstrup Pedersen.

Finally, thanks to my family and particular my wife, Birgitte, for patience and a tolerant acceptance of the long hours of work.

Chapter 1

Consideration about design and fatigue life

1 Introduction

Fatigue problems arise in many industries, and as such they compose a crucial factor when it comes to designing reliable structures, products and components. Needless to say, the design engineer has to pay attention to this in the design phase. Consequently, research concerning investigation and improvement of the fatigue resistance is carried out world-wide in almost all structural and mechanical engineering fields, both well-established and newly commenced ones. For instance, in the relatively new field of wave energy systems, great focus is dedicated to investigate the fatigue resistance since the harsh environment and high number of load cycles yield adverse fatigue life conditions, see e.g. [42, 94, 95]. Attention has been paid to wave energy systems, such as the Wavestar machine depicted in fig. 1.1, in order to improve the fatigue life of the structural components. Additionally, attention has been paid to clarify the material properties, particularly the fatigue resistance. Here, testing of these properties focuses on setups that imitate the applications and hereby reduce the distinction between testing and using of the material. Examples of such studies can be found in [47, 48] and [49] where laser welds and pipes of CuNi10 are investigated.

2 Fatigue life, reliability and cost

In the design phase of structures and structural components, the governing factor is the balance between quality and cost. The quality relates directly to the fatigue resistance as high quality materials and manufacturing often pro-



Fig. 1.1: Structural detail of Wavestar energy system, subjected to high cyclic loadings at the connection of the hydraulic cylinder and the hollow steel arm.

vide enhanced reliability of the expected fatigue life. This balance between quality and cost is stressed out in [42] where the float structure of the Wavestar energy system, see Figure 1.1, is redesigned in Ultra High Performance Fiber Reinforced Concrete [41] in order to be more cost-effective, and yet still maintain structural integrity for the expected fatigue life.

Another example of fatigue life estimation-based designs is the driving system in a car. Here, all the components are designed in compliance with a specific fatigue life which is often based on a distance measure, e.g. transmission systems typically past 300.000 km before failure occurs. Figure 1.2 shows a failure of a tooth in such transmission system. Generally, the driving system contains many sub-components which are exposed to fatigue loading, hence increasing the risk of fatigue failure. Consequently, quality control is essential in the attempt to comply with a specific life for all of the involved components. However, these controls of, i.a., welds and materials will also lead to an increase in general production costs, thus emphasizing the tradeoff in structural designs.

Besides the direct costs related to structural design, some indirect, yet often very critical, costs can also arise. For instance, downtime of a production line due to fatigue; if just one of the processes is down in a production line, a potential risk for a complete breakdown of the production is present. If this breakdown occurs in the production line, the downtime can be several days. Often, it is the procurement of spare parts and not the reparation itself that

3. Fatigue problems in practice



Fig. 1.2: A tooth interior fatigue fracture of a gear failure.

constitutes the main part of the downtime. Such delays occur because spare parts are not always available, thus making it necessary to order them from a remote warehouse. This will generate a loss in productivity which, of course, is inexpedient. Some industries, in particular those where new products are frequently released, are very sensitive to a variation in the quantity produced in a production line. In these industries, the quantity of products in stock is low, thus a continuous production flow is essential. Accordingly, the sale is more dependent on the reliability of the production line and fluctuations in the production volume. An example is the electronic industry in which many new products are introduced to the market every day.

3 Fatigue problems in practice

Obviously, fatigue failure in structures or components is undesirable. A fatigue failure occurs rapidly and often spreads the damage to other parts. This is the nature of fatigue failure, and it is difficult to discover before it gets critical. Failure is especially unwanted in cases where the risk of human casualties is present, e.g. in the aviation industry. Here, failure is extraordinary critical and therefore various efforts are made in order to satisfy the required safety. Components are checked frequently such defects or crack initiation can be discovered in time. Particularly, the main structure and the engine of an airplane are important, so for these parts, an extraordinary high level of inspection is conducted [15]. This results in high structural reliability and

extremely low probability of failure, but also substantial costs.



Fig. 1.3: Fatigue failure in a Boeing 737-200 from Aloha Airlines Flight 243 which operated near Hawaii. "Winnipeg Free Press, Saturday, May 21, 1988".

Despite the comprehensive precautionary measures in the aviation industry, numerous fatigue-triggered flight disasters have occurred. As an example, the disaster of Airplane Aloha Airlines Flight 243 where a sizeable part of the airplane fractured during a flight at an altitude of several thousand meters. Figure 1.3 shows the airplane with passengers just after landing. Clearly illustrating the complexity of fatigue, the failure was caused by, respectively, corrosion in the glue interface, small cracks, exceptionally many take-offs and an inspection level which was not adjusted to the actual number of take-offs, namely 89090 flight cycles. The fatigue damage was generated by oscillation in the air pressure between the outside and inside of the cabin. This oscillation occurs in all modern airplane, but in this case, the number of pressure variations was unusually high due to the many takes-off. This combined with other factors, particularly environmental ones, caused the damage to be so comprehensive. The flight operated in regions with high concentration of salt which initiated onset of corrosion damages in the glue layer of the assembly details.

Previously, fatigue failures in airplanes have been known from cases where nearly the whole airplane fractured. To prevent this from keep on happening, engineers have designed the airplanes in such a way that a fracture should only damage a limited area. Specifically, this is sought by employing so-called Tear straps, see Figure 1.4, which are fuselages that should prevent cracks from growing through the whole structure. These fuselages consist of two or three rows of holes in square-formed sections, hence if a crack starts to grow, it will only fracture in the square sections. This means that

4. Estimation of the fatigue life

damage is controlled, having only limited effect on the structural safety [86]. However, although being equipped with these Tear straps, Airplane Aloha Airlines Flight 243 did in fact experience damages in much of the structure. This was due to many small cracks in the fuselages; cracks which, as previously mentioned, were initiated by harsh environmental conditions and got to spread from one section to another. Normally, these cracks would have been caught in the inspections, but in the present case, the inspection level was not adjusted to the number of take-offs.

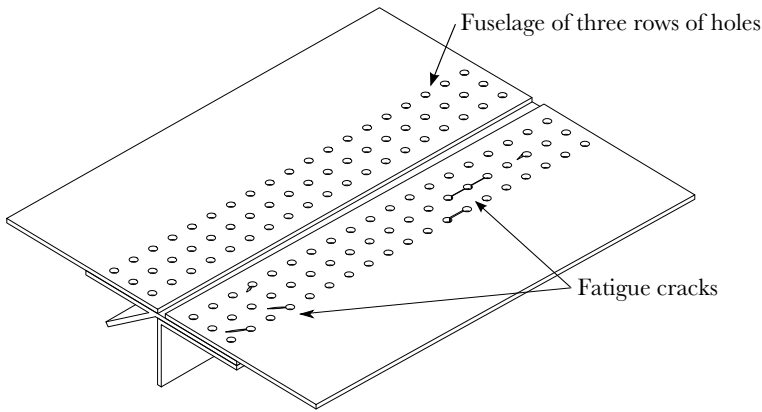


Fig. 1.4: Assembly detail in an airplane with tear strap in the connection.

The failure in the presented case happened since several factors were not modified or included in the assessment of the expected fatigue life. Overall, the design, loading and inspection are essential for the estimation, and if these three factors were reconsidered when changing the route for the airplane, the risk for fracture was minimized.

4 Estimation of the fatigue life

The disaster of Airplane Aloha Airlines Flight 243 clearly emphasizes the importance of including all significant factors in the fatigue considerations. However, in order to do so, the mechanisms behind fatigue-induced structural failure must be understood fully, which is not the case at present. Research is still going on to achieve this and at present, several methods are accepted as valid approaches for estimation of the fatigue life of a component or a structure. Common for these methods is that the estimation of the fatigue life is based on assumptions which take into account the variation in design case and the uncertainty in the understanding of fatigue failure mechanisms.

The most frequently applied method for fatigue estimations is the S-N curve approach, in which many of the complex mechanisms are contained and hereby, in a relatively simple way, included in the total fatigue life estimation. The S-N method is applicable in many standard design cases. However, since the method is relatively simple, some uncertainties exist. For the standard cases, these uncertainties are covered by use of high safety margins, which result in structural oversizing. For more advanced and complex design cases, the S-N method is inapplicable since the uncertainties are not fully covered only by use of high safety margins.

Generally, fatigue estimation is divided into two scenarios, namely low cycle and high cycle fatigue. Here, the low cycle fatigue is estimated relatively precise, whereas the high cycle fatigue is rather imprecise since significant fluctuations occur in the fatigue life, primarily due to the crack initiation phase which is very sensitive towards the characteristics of the surface, e.g. metallurgy variations, micro cracks, surface roughness and residual stresses. Unlike the low cycle fatigue, where this initiation phase is past rapidly, the majority of the life for high cycle fatigue is the initiation.

Chapter 2

Theoretical fracture Mechanics

1 Historical review and invention of the first fracture mechanics theory

In 1921, A.A. Griffith, an English engineer, investigated the strength of materials [31]. Although the aim of this research was to determine the strength of materials, A.A. Griffith established the first step of fracture mechanics. In the investigation, he discovered that flaws have a significant influence on the material strength, leading to a discrepancy between the theoretical strength and the values obtained in experimental testing. In general, the theoretical strength was significantly higher than what was observed in the laboratory. The experiments were carried out with soda glass since this material is brittle and contain extraordinary few flaws. The findings from these experiments were compared with a theoretical strength, derived by using the strength of the atomic bonds for a perfect crystal [54]. The value of the strength was obtained by introducing a separation model for the material based on the atomic forces. This model is relatively simple for soda glass due to its brittle nature.

fig. 2.1 illustrates the separation of atoms and also the force response. Here, d_0 is the intra-atomic distance when the material is in a state of equilibrium [54]. When adding a force to the atoms, a separation is initiated. As the force increases to some extent, the separation continues, hence yielding an atomic distance of d_1 . When d_1 is exceeded, the force decreases. In the first part of the separation, the stiffness will be equal to the modulus of elasticity, but as further separation occurs, the stiffness decreases. Based on such separation assumption, the maximum theoretical tension strength, σ_{\max} , and

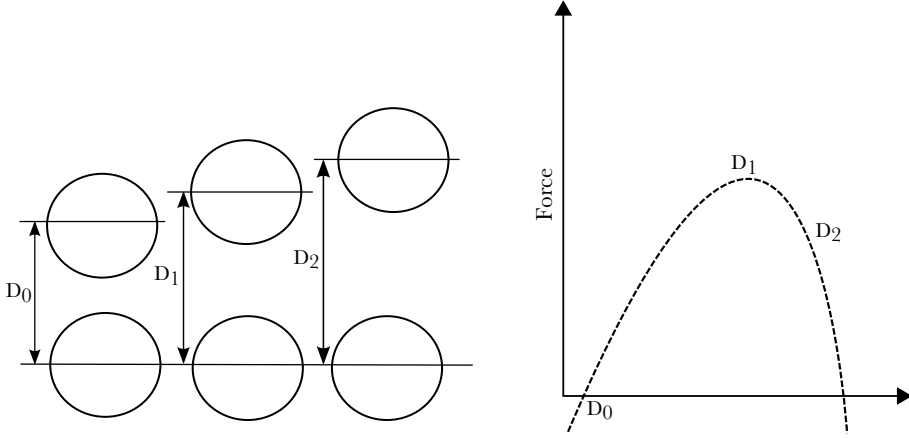


Fig. 2.1: Illustration of the separation force.

the maximum theoretical shear strength, τ_{\max} , can then be computed by

$$\sigma_{\max} = \sqrt{\frac{E\gamma_s}{d_0}} \cong \frac{E}{\pi} \quad (2.1)$$

and

$$\tau_{\max} \cong \frac{G_m}{2\pi} \approx \frac{E}{17}, \quad (2.2)$$

in which E , γ_s and G_m are the modulus of elasticity, the surface energy and the shear modulus, respectively. Thus, based on eq. (2.1), typical structural steel, e.g. S355JR, should have a strength of approximately 70000 MPa. This value is, however, far beyond what is found in experiments. As a result, the theoretical strength is obviously insufficient in the estimation of material strength. This is due to the influence of other factors, such as the presence of internal material flaws, which greatly reduce the material strength.

Griffith investigated what kind of impact these imperfections has on the strength of soda glass. Through experiments, he discovered that the stress level at which failure will occur, σ_f , relates directly to the length of the material flaw, a , by [84]

$$\sigma_f \sqrt{a} \approx C, \quad (2.3)$$

for which it was later shown that the constant C is an indication of material toughness and that a failure depends on an energy balance.

2 The energy criterion for cracks

Through his experiments, Griffith also formulated an energy criterion which is applicable for describing why a crack becomes unstable. The criterion is based on the strain energy releasing when a crack grows an incremental length, plus the strain energy consumption required to generate new crack surfaces. In fig. 2.2, it is seen how the stress-relaxed area increases as energy is released due to crack growth.

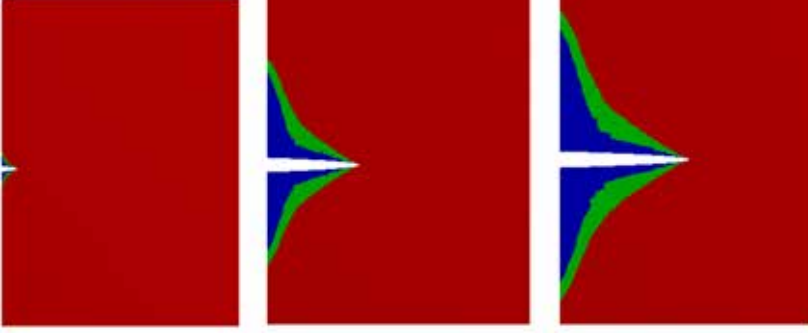


Fig. 2.2: Illustration of the increment of the stress-released area around a crack tip.

The amount of strain energy contained in a particular zone can be calculated by use of

$$U_a = -V \frac{\sigma^2}{2E}, \quad (2.4)$$

where V is the area, or volume in case of three-dimensionality, of the stress-released region, while σ is the stress acting in the material. As the size of the crack increases, the stress-released region will naturally increase non-linearly.

As mentioned earlier, strain energy is consumed when new crack surfaces are generated. Specifically, these surfaces are generated through atom separation. The amount of energy required to create new crack surfaces can be calculated by use of

$$U_s = 4\gamma_s A, \quad (2.5)$$

with γ_s being the surface energy and A the area of the generated crack surface, which is multiplied by four, i.e. two for each crack, as two surfaces will appear when a crack is generated. From eq. (2.5), it is seen how the consumed energy is directly proportional to the crack size. In fig. 2.3, the

amount of energy released and consumed is illustrated for the scenario of increase in crack size.

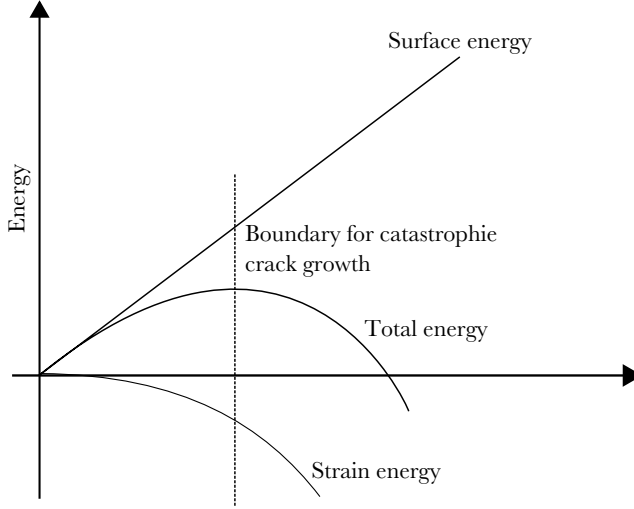


Fig. 2.3: Schematic illustration of the rates of energy change with crack extension.

Evidently, the surface energy increases linearly, while the released strain energy increases non-linearly. Consequently, at a specific crack length and stress state, an incremental crack growth will yield a larger strain energy release than surface energy consumption. This will result in an unstable crack which Griffith categorized as fracture. This critical state is reached when

$$U_a = U_s \Leftrightarrow V \frac{\sigma^2}{2E} = 4\gamma_s A, \quad (2.6)$$

which, in the case of a center crack, can be rewritten into [68]

$$\frac{dU_a}{da} + \frac{dU_s}{da} = 0 \Rightarrow \sigma\sqrt{a} = \sqrt{\frac{4\gamma_s E}{\pi}}. \quad (2.7)$$

The former expression in eq. (2.7) states the equilibrium obtained when the released and consumed energy is equal.

The outlined theory is based on the assumption that no plastic zone is formed in front of the crack. However, almost every material has some level of plasticity, hence there is a clear distinction between this theory and what truly happens in the zone in front of the crack. Despite the assumption of no plasticity, G.R. Irwin showed that his theory yields a good approximation when the plastic zone at the crack tip is relatively small [22]. In cases where

3. Stress intensity factor

the aforementioned zone is large, elastic-plastic fracture mechanics (EPFM) must be employed.

3 Stress intensity factor

Based on Griffith's energy approach, G.R. Irwin formulated the stress intensity factor, K , and subsequently showed that this is related to the strain energy release rate, also known as the crack driving force, G , through

$$G = 2\lambda = \frac{K^2}{E'}, \quad (2.8)$$

where λ is the surface tension. It is noticed that the letters K and G were specifically chosen by Irwin to honour one of his co-workers, J.A. Kies, and Griffith [85].

It is common to use the stress intensity factor when studying the stress fields around a crack, as this factor describes how intensive the stresses are in this area. This is described further in section 4. When it comes to fracture mechanics, K is often used to assess the severity of a certain crack. As described further in chapter 3 this assessment is based on a predefined threshold and critical values of K .

When loading a crack, the three different loading modes illustrated in fig. 2.4 can occur. Each of the three modes has a stress intensity factor, K_j where $j = 1, 2, 3$. Normally, K_1 , which relates to the opening failure mode, is considered to be the most important one, and therefore K_2 and K_3 are often not considered. This will also be the case in the present thesis. For expressions regarding K_2 and K_3 , the reader is referred to [79].

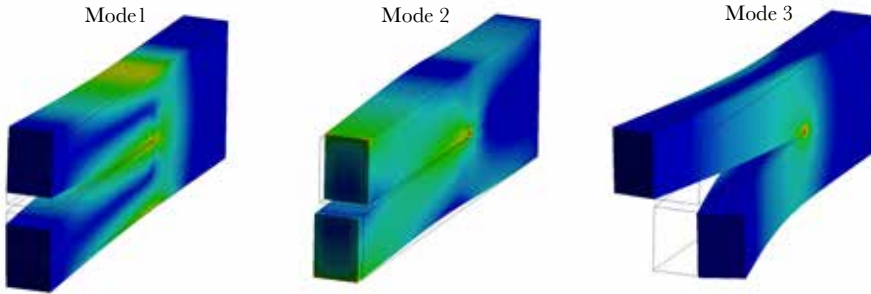


Fig. 2.4: Basic modes of crack loading.

In case of a center crack, K_1 can be calculated by

$$K_1 = \sigma \sqrt{\pi a} f\left(\frac{a}{w}\right), \quad (2.9)$$

where σ is the far field stress, a is half of the total crack length, and the function $f(\frac{a}{w})$ is related to the size of the crack, a , and the width of the component in question, w . The stress intensity factor is not affected significantly by the crack if $a \ll w$. Besides the crack length to width ratio, it is also well known that the geometric nature of the component in question may affect f . Therefore, it is necessary to include this when calculating the stress intensity factor.

In case of a center crack, f can be derived by the simple expression

$$f\left(\frac{a}{w}\right) = \sqrt{\frac{2w}{\pi a} \tan \frac{\pi a}{2w}} \quad (2.10)$$

or the comprehensive, yet more precise, expression

$$f\left(\frac{a}{w}\right) = \left(1 - 0.025 \left(\frac{a}{w}\right)^2 + 0.06 \left(\frac{a}{w}\right)^4\right) \sqrt{\sec \frac{\pi a}{2w}}. \quad (2.11)$$

In the case of an edge crack, the analogous expressions for K_1 is

$$K_1 = 1.12\sigma\sqrt{\pi a} f\left(\frac{a}{w}\right), \quad (2.12)$$

while f becomes

$$f\left(\frac{a}{w}\right) = 1.122 - 0.231 \left(\frac{a}{w}\right) + 10.550 \left(\frac{a}{w}\right)^2 - 21.710 \left(\frac{a}{w}\right)^3 + 30.382 \left(\frac{a}{w}\right)^4 \quad (2.13)$$

or

$$f\left(\frac{a}{w}\right) = \sqrt{\frac{2w}{\pi a} \tan \frac{\pi a}{2w}} \frac{0.752 + 2.02 \frac{a}{w} + 0.37(1 - \sin \frac{\pi a}{2w})^3}{\cos \frac{\pi a}{2w}}. \quad (2.14)$$

The deviations in f for an edge crack and a center crack is, as stated, due to the influence of geometry. This is illustrated in fig. 2.5 where it is evident that an edge crack quickly becomes critical. It is noticed that the general solutions for other crack loading conditions can be found in [79].

The stress intensity factor can also be computed by use of the displacement of the crack surfaces; displacements which, e.g., can be derived through an finite element analysis (FEA). By means of the displacement of the point near the crack front, the stress intensity factor can be calculated as [67]

$$K_1 = \frac{x_d E}{2} \sqrt{\frac{\pi}{2r}}, \quad (2.15)$$

4. The crack tip stress field

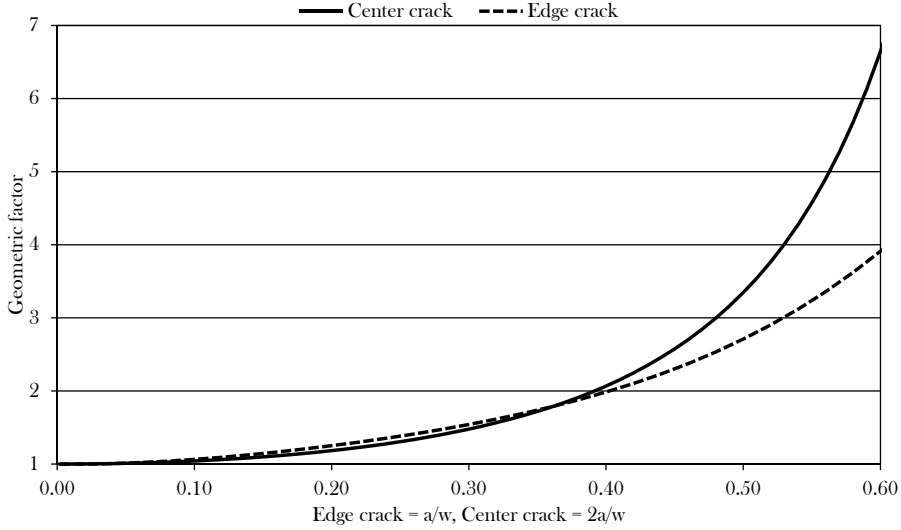


Fig. 2.5: Boundary effect on the stress intensity for an edge and a center crack.

in which x_d and r are the displacement of the crack face nodes from the crack center line and the distance from the crack tip to the reference node on the crack, respectively. Today, this approach is, however, not often used. Instead, when it comes to FEA, the J-integral is most frequently applied, see section 5.

4 The crack tip stress field

As described in section 3, it was G.R. Irwin who introduced the stress intensity factor as a way to represent the stress field around a crack. It is worth noticing that other related contributions were made before Irwin introduced the stress intensity factor, see e.g. [40, 66]. For instance, the first theoretical work was based on representing the crack as a narrow ellipse. Here, the stress concentration factor can be found as

$$\sigma_{\max} = \sigma_{\text{app}} \left(1 + 2\sqrt{\frac{a}{\rho}} \right) \quad (2.16)$$

where σ_{app} is the far field stress while ρ is the geometrical form factor. If $\rho \rightarrow 0$, an actual crack is mimicked validly sine the curvature radius of the ellipse becomes correspondingly small.

In practice, the crack curvature depends on the metallurgical composition. In general, brittle materials have smaller crack tip radius than ductile materi-

als [65]. In a very brittle material, such as soda glass, the radius of the crack tip is about 1 nm, while it for tougher materials, e.g. construction steel, can be around 7 μm . With these small scales, eq. (2.16) becomes inadequate when working with engineering stresses and strains since these are not applicable on an atomic level. In these cases, the singularity stress field approach proposed by Irwin should be employed [40]. Here, it is assumed that the crack tip is infinitely small, i.e. a singularity, such the stresses at the tip become infinitely large, as seen in fig. 2.6. The stress field can be described by

$$\sigma_y = \frac{K_1}{\sqrt{2\pi r_\sigma}}, \quad (2.17)$$

with r_σ being the distance from the crack tip to the point in which σ_y should be evaluated. The complete stress field can be derived from

$$\begin{Bmatrix} \sigma_x \\ \sigma_y \\ \tau_{xy} \end{Bmatrix} = \frac{K_1}{\sqrt{2\pi r_\sigma}} \frac{1}{4} \begin{Bmatrix} 3 \cos \frac{\theta}{2} + \cos \frac{5\theta}{2} \\ 5 \cos \frac{\theta}{2} + \cos \frac{5\theta}{2} \\ -\sin \frac{\theta}{2} + \sin \frac{5\theta}{2} \end{Bmatrix}, \quad (2.18)$$

where θ is the angle relative to the crack plane. eq. (2.18) can also be ex-

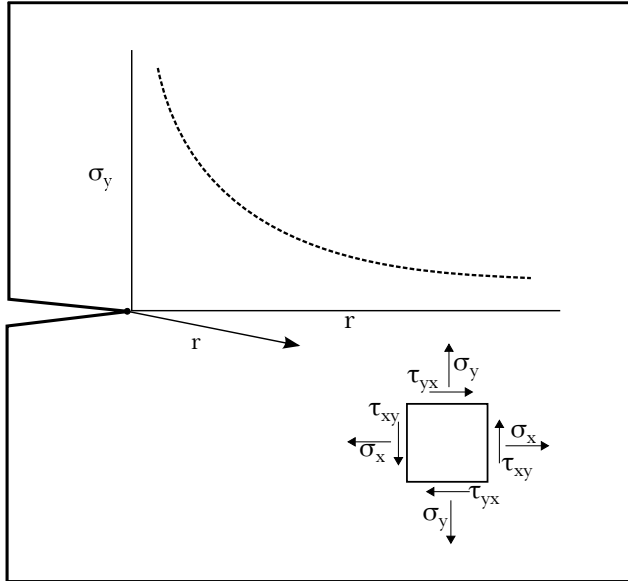


Fig. 2.6: Illustration of the stress field around a crack tip.

5. Stress intensity factor by path or volumen integral

pressed with regards to principal stresses,

$$\begin{Bmatrix} \sigma_1 \\ \sigma_2 \\ \sigma_3 \\ \sigma_3 \end{Bmatrix} = \frac{K_1}{\sqrt{2\pi r}} \begin{Bmatrix} \cos \frac{\theta}{2} (1 + \sin \frac{\theta}{2}) \\ \cos \frac{\theta}{2} (1 - \sin \frac{\theta}{2}) \\ 2\nu \cos \frac{\theta}{2} \\ 0 \end{Bmatrix} \begin{matrix} \text{"plane strain"} \\ \text{"plane stress"} \end{matrix} \quad (2.19)$$

with ν being the Poisson's ratio.

5 Stress intensity factor by path or volumen integral

It is possible to compute the stress intensity factor by use of other methods than the one described in section 3. One of these methods is the J-integral, which is widely applied when dealing with FE-based analyses. Another advantage is that the J-integral is usable in cases of elastic plastic fracture mechanics (EPFM) [61].

The integral is a path-independent, energy-based line integral given by

$$J = \int_{\Gamma} (W dy - T_i \frac{\Delta u_i}{\Delta x} ds), \quad (2.20)$$

from which the crack driving force can be found through

$$J = G = \frac{K^2}{E}. \quad (2.21)$$

In eq. (2.20), W is the strain energy density, T_i is the stress vector, u_i is the displacement vector and ds is an increment along a contour surrounding a crack tip.

In commercial FE software, such as ANSYS and ABAQUS, the J-integral is calculated by adding a number of patches, typically at least six for computing a satisfactory result [67]. Here, the first patch is smallest and the following patches increase in size, often by a radius. For the first patch, the computed stress field will be inaccurate since the crack tip contains a singularity. Thus, in order to obtain an accurate result in general, the results from the first patch, and sometimes also those from the second patch, are typically disregarded. The final result is then calculated as the mean of the results from the remaining patches.

The accuracy of J-integral result also depends on other FE-related factors, such as the mesh surrounding the crack tip. The mesh needs to be distributed such that it facilitates valid representation of the crack front stresses, which are proportional to $1/\sqrt{a_r}$. In ANSYS Workbench, this is often done by using

rings of collapsed quadratic quadrilateral elements [3], but actually a more suitable element exists. This element is the so-called singularity element, or quarter-point element, in which the mid-side node is shifted to the quarter points, see fig. 2.7, hereby improving the representation of the stress field. In practice, however, the quadratic quadrilateral elements are commonly used since these can provide an acceptable representation of the stress if the element size is very small.

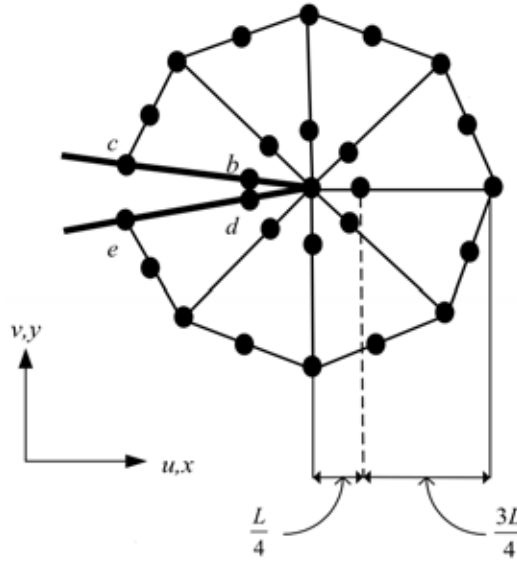


Fig. 2.7: A typical arrangement of the natural triangle quarter-point elements around a crack tip. Permission by [59]

Shih et al. [72] describe a domain integral what where usable for evaluation the stress intensity factor in domain e.g., in area/volumes. This domain integral is based on the line-integral expression for the energy release rate also known as the J-Intergral but is expanded by a domain expression so it abels evaluation of the energy release rate along a three-dimensional crack front. Such evaluation occur by pointwise computation of the values [89].

6 The equivalent stress intensity factor

Loading of a crack at mode 1, as shown in fig. 2.4, is relatively simple. Sometimes, the loading is more complex, meaning that K_2 and K_3 contribute significantly to the crack growth and, hence, the total stress intensity factor. In such cases, K_2 and K_3 should be included in the analysis, for instance as done

6. The equivalent stress intensity factor

by use of the equivalent stress intensity factor proposed by Tanaka [80]:

$$\Delta K_q = \left(\Delta K_1^4 + 8\Delta K_2^4 + \frac{8\Delta K_3^4}{1-\nu} \right)^{0.25}, \quad (2.22)$$

by which the mixed mode conditions can be simplified to a single value of stress intensity. It is noticed that numerous other methods for including K_2 and K_3 have been proposed. Some of these can be found in [53,58].

Chapter 3

Applied Fracture Mechanics

1 Cracks in materials and use of a fracture mechanics approach

When examining fatigue damage from a fracture mechanics point of view, several methods are available for inspecting the damage such various crack-related phenomena can be identified. Typically, phenomena such as trans- and intercrystalline crack growth, shear lips and beachmarks can be observed. These observations contribute to the understanding of the specific fatigue damage and, thus, clarify the condition of the material. For example, intercrystalline crack growth, as depicted in fig. 3.1, is a typical sign of corrosion fatigue.

In general, by understanding the particularities of a fatigue damage, it is possible to remove or reduce the source that causes the fatigue damage, e.g. environmental conditions such as seawater. As an addition, observations are also practicable for determination of crack growth rate and crack formation.

As mentioned in section 1, the S-N method is often applied for computing the fatigue life. The use of this method is beneficial in many cases, particularly for estimation of the total fatigue life. However, if a crack is discovered in the structure, the S-N method does not provide the necessary degree of details, making it insufficient in these cases. Instead, it is necessary to employ another method for evaluating the fatigue life; typically in the form of a fracture mechanics approach where parameters such as critical crack size and crack growth rate are utilized. In order to enhance the reliability of the fatigue life estimation, inspection of the structure, with regards to crack growth, can be conducted.

Every structural material contains imperfections and flaws. Usually, these are inconsiderable in size compared to the structural elements. However,

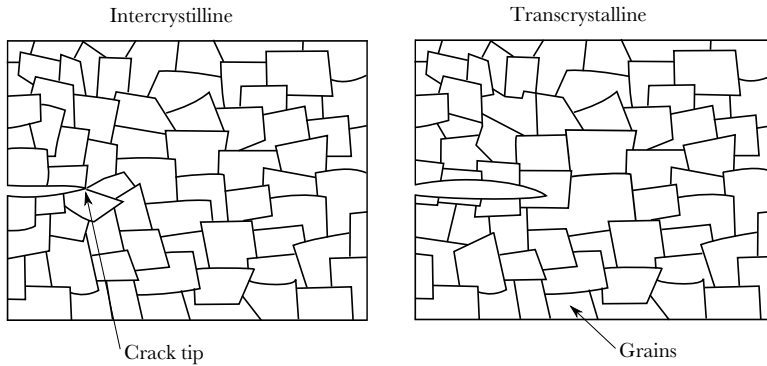


Fig. 3.1: Illustration of the transcrystalline and intercrystalline crack growth.

it is important to keep in mind that small flaws have a significant impact on the strength, see section 1, and hereby the fatigue resistance. If a crack arises at a stress concentration spot, its growth rate will be increased such that the critical size will be reached even faster. Such a stress intensity spot can, for instance, be found in welded joints, see fig. 3.2, where the issue is of huge importance. For the specific case depicted in fig. 3.2, the weld toe has a wedge-like shape, which weakens the joint due to a reduction in the capability to resist cracking. Furthermore, this joint has an inclusion in the material, and this is also critical in proportion to fatigue cracking. Thus, it is evident that the welding is produced with low requirements to the welding quality. However, in the present case, the joint is actually usable as it is subjected to a load which is far below what generates crack growth [48,49].

The fracture mechanics approach is also applicable for investigation of more specific crack growth issues. This can, e.g., be seen in [50] where the impact on the crack growth from a patch repairing is investigated. The investigations were conducted numerically on the basis of a model containing an edge crack repaired by use of a surface layer of coating, as depicted in fig. 3.3. A patch repairing is often used in cases where replacement of damaged components is infeasible, as is often the case in the aircraft industry [67]. The patch repairing technique can stop or slow down the crack propagation in a damaged component because of the resulting decrease in stress intensity factor. For the model in fig. 3.3, the stress intensity factor is difficult to compute analytically due to combination of different materials, hence emphasizing the general applicability of FEA.

1.1 Fracture failure in structures and components

Typically, a fracture mechanics approach is applied in two cases; namely when real cracks are detected in a structure and in preliminary studies where

1. Cracks in materials and use of a fracture mechanics approach

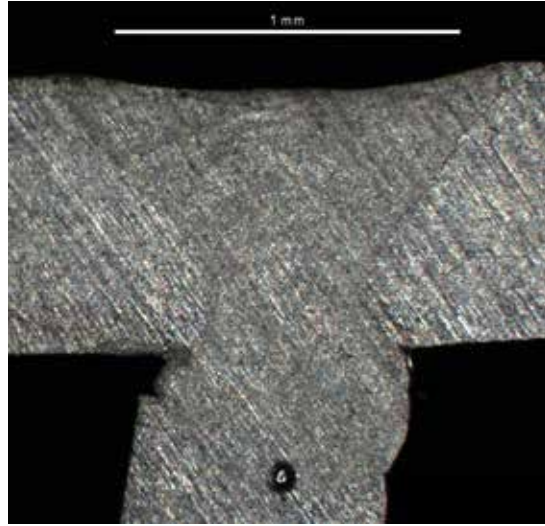


Fig. 3.2: Laser-welded T-Joint with imperfections in the form of inclusion and wedge-formed welding toe.

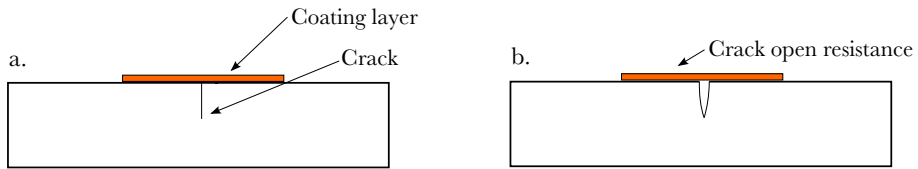


Fig. 3.3: Patch repairing for surface crack. (a) Non-loaded surface crack with a layer of coating. (b) Loaded crack with coating [50].

an imaginable crack is considered. For the former case, by introducing inspections of the crack growth rate and then adjusting the calculated values based on the observation, fatigue estimation is improved, hence increasing the structural reliability, and modification of the inspection intervals or further initiatives can be incorporated. In the second case, the approach is to place an imaginable crack in the structure and subsequently apply a fracture mechanics-based evaluation. Such method depends on engineering judgment because the engineer must consider where cracking will occur. In order to do this properly, the engineer must have basic knowledge about fracture mechanics and understand why cracks in structures are critical when it comes to safety.

Normally, material failure is associated with high level of strains, which generally leads to ductile failure. For such failure type, relatively large deformations are introduced, thus it is uncomplicated to discover and detect an overload. Contrary to ductile failures, fatigue failures occur suddenly with

no warning, making these extraordinary dangerous. In order to illustrate the impact of a crack on the maximum load capacity, a value for this capacity can be computed by the yielding criterion for the undamaged case and by a fracture mechanics approach for the damaged case. In this way, comparison of the derived values will yield a measure of the impact of introducing a crack. Additionally, the Failure Assessment Diagram (FAD) can be utilized as a more systematic comparison approach.

Example: Crack influence on the load capacity and deformation of a beam

In this example, the T-beam depicted in fig. 3.4 is studied numerically. The beam is subjected to 4-point bending and analyzed with regards to deformations and load capacity for, respectively, and undamaged and cracked configuration of the beam. The beam is assigned a material model corresponding to aluminum 7075-T651, with a yielding strength of 503 MPa and $K_c = 790 \text{ MPa}\sqrt{\text{mm}}$.

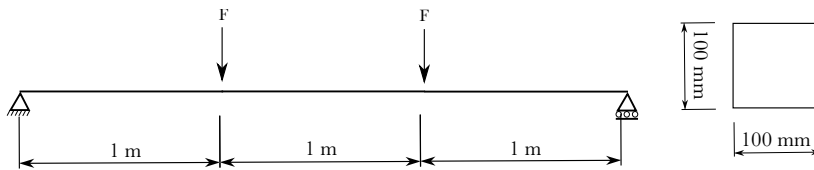


Fig. 3.4: T-Beam setup and the cross section.

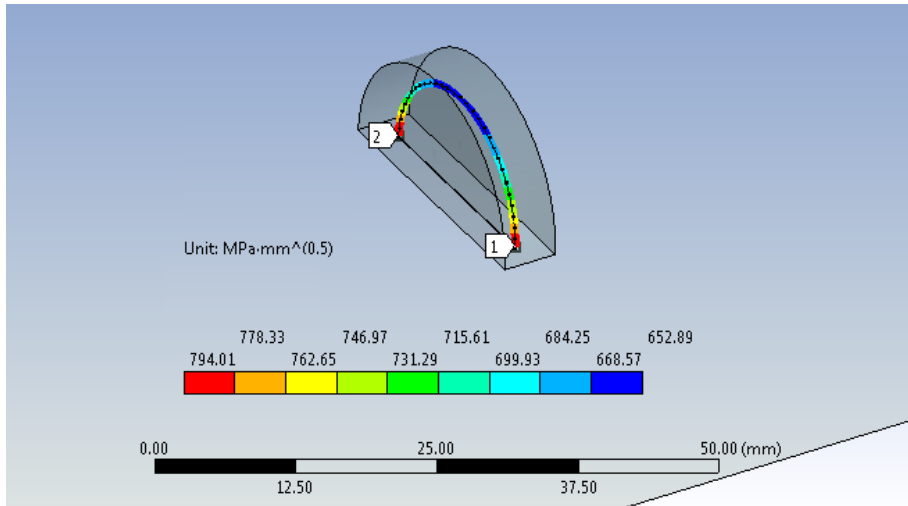


Fig. 3.5: Plot of the stress intensity factor for a semi-elliptical surface crack.

ANSYS Workbench is used to compute the deformations and the stress

1. Cracks in materials and use of a fracture mechanics approach

intensity factor. The crack added to the beam is a semi-ellipse with a wide and depth of 10 mm, leading to the stress intensity factor results seen in fig. 3.5. For the undamaged configuration, the load capacity inducing yielding is found to be 84 kN, while the analogous result for the cracked beam is found, through the fracture toughness, to be 35 kN. Thus, the crack introduction yields a substantial reduction of load capacity. By calculating the deformations associated with the found load capacity for the undamaged configuration, the crack-induced stiffness changes can be examined. Here, it is found that the deformations increase insignificantly from 56.253 mm to 56.286 mm, making it difficult to discover a crack by studying the deformations.

Fatigue failure process and fracture surface

When a failure occurs as a direct consequence of fatigue, it can be of use to study the fracture surface since this provides a lot of information regarding the failure. For instance, in some cases, the fracture surface shows phenomena such as inclusions, hydrogen cracks, shear lips, beach marks, striations and final fracture area. Additionally, the fracture surface can clarify the load history, start point and failure point of the crack, hereby outlining the history of the created fatigue failure.

Several of the characteristic fatigue fracture signs are visible and can be studied quite easily without any equipment. This is exemplified in fig. 3.6 which illustrates a fracture surface where the three phases composing the fatigue failure process, namely initiation, crack growth and final fracture, are visible. Other marks and phenomena are minuscule and are as such not visible to the naked eye, hence in general laboratory devices must be used for observations of the fracture surface. Often, a microscope is used for these observations as it makes details visible down to the level of sizes of steel grains. In rare cases, a standard microscope is not sufficient since few phenomena, e.g. striations, are of the size of few microns, thus a more advanced microscope, namely an electron one, must be employed.

In the failure process, the crack initiation constitutes the first phase. When the crack obtains a specific size, the growth mechanism changes to phase 2 in which the crack grows regularly. If reaching a size where the crack becomes unstable, the third phase, i.e. final fracture, is attained. Investigation of these phases have been conducted in a countless number of scientific papers, see e.g. [13,76,81]. Common for these studies is that the stress intensity factor is used to define how intensive a crack is loaded.

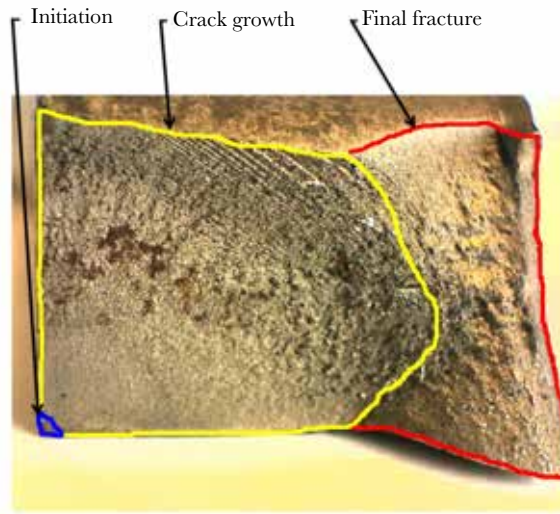


Fig. 3.6: The fracture surface of a steel specimen, with the three stages of fatigue fracture being visible.

2 Phase 1: Crack initiation

In the crack initiation phase, the crack develops in the maximum shear plane and will mainly initiate at nucleations as large inclusions or dislocations. Thus, crack initiations occur when no or only small defects, less than 1 mm, exist in the material. Typically, slip planes down to the size of a grain are developed in the phase; slip planes which, when subjected to an oscillating load, grow together to form a crack. fig. 3.7 shows a microscope view of the early stage of slip plane growth. Notice how the surface roughness changes as the material has been loaded.

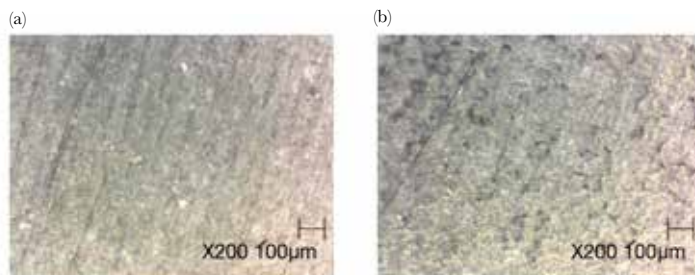


Fig. 3.7: Macroscopic view of AISI 304 steel surface. (a) Surface before loading. (b) Surface after loading, with visible slip planes.

The crack initiation is of particular interest since the majority of the total

2. Phase 1: Crack initiation

fatigue life, in case of high cycle fatigue, lies within this phase, as illustrated in fig. 3.8. Therefore, the main focus is dedicated to this phase in cases where the aim is to improve the fatigue life. Contrary, for low cycle fatigue, it is seen in fig. 3.8 how the initiation phase only composes a small part of the total fatigue life. Instead, the crack growth phase is predominant here.

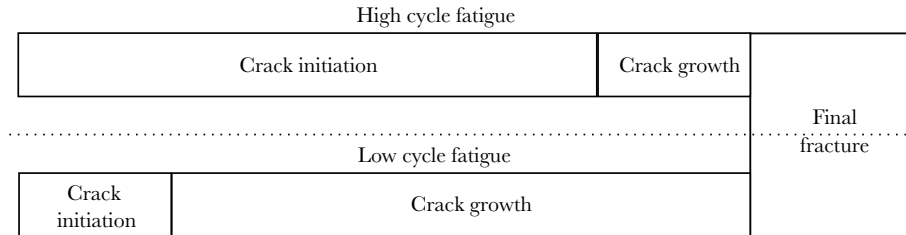


Fig. 3.8: Illustration of the three phases of fracture mechanics cracking in case of high and low cycle fatigue.

2.1 Redistribution of dislocations and its influence on crack initiation

The crack initiation process is affected by the nature of the crystal structure. In the case of steel, there is a considerable amount of dislocations inside the material, which have significant influence on the resistance towards initiation of fatigue cracks. When adding an oscillating load to a steel structure, two mechanisms with relation to dislocations may occur. Firstly, loading can trigger a redistribution of the dislocations, resulting in strain softening. Here, the dislocations are organized in such a way that the crystals are firmly fixed and hereby locking each other. In this way, local softening arises when an oscillating load is applied, since the dislocations redistribute to a less fixed position. The opposite occurs if the dislocations are organized in a less fixed position, meaning that hardening behavior can occur if an oscillating load is applied such that the dislocations are interlocked. Generally, materials with softening properties have good resistance towards crack initiation, whereas materials with hardening behavior will become more brittle, meaning that the resistance towards crack initiation is reduced.

2.2 Slip bands and crack initiation in AISI 304

The description given in section 2.1 is relatively simple and does not sufficiently cover AISI 304, since this material has a more complex behavior. As in other steel materials, slip bands are observable in the early stages of the fatigue process, as shown in figs. 3.7 and 3.9. Notice how deformation of the crystals makes each grain structure visible. Especially for the highly

deformed case, i.e. the one depicted in fig. 3.9(c), the grain structures are conspicuous.

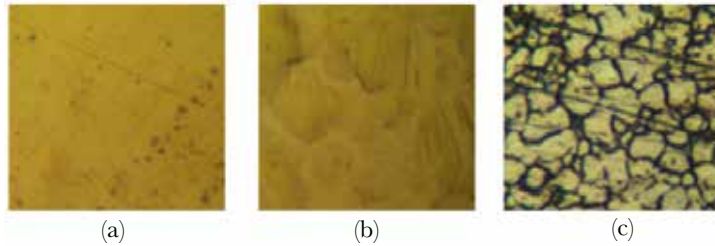


Fig. 3.9: Microscopic view of AISI 304 steel surface. (a) Surface before loading. (b) Surface when a relatively small oscillating load has been added. (c) Surface when an intensive plastic deformation has been introduced.

Other processes, which enhance the formation of cracks, are typically also present in AISI 304. One of these processes is twinning-induced plasticity (TWIP), which is a change in the nature of the metallurgical structure, as seen in fig. 3.10. In [48], TWIP was found in a welded joint subjected to an oscillating load. It should be noticed that twin transformation and dislocation gliding are to separate processes and as such they have different effects on the crack initiation. In the latter, a separation of the bindings occur which is not the case for twin transformation. When inspecting a crack surface, the two processes can look similar since they both occur at the maximum shear plane.

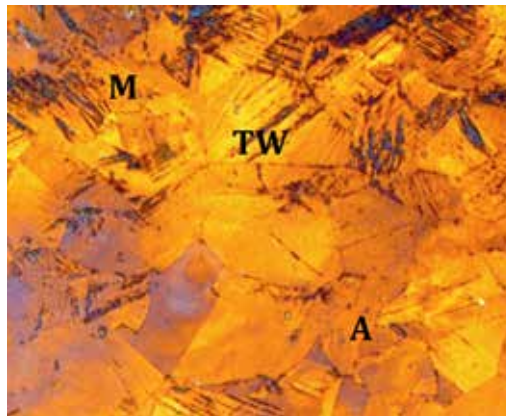


Fig. 3.10: Etching of AISI304 with LB1. Austenite (A), martensite (M) and TWIP (TW) formation are present. [49]

2. Phase 1: Crack initiation

2.3 K_{th} according to BS7910

The transition from phase 1 to 2 occurs when a threshold value for the stress intensity factor, K_{th} , is exceeded. Determination of this threshold value is complex since numerous factors, e.g. the material, affect the value, and as a result, no general rule covering all conditions and materials exists at present. Besides the material, the threshold value strongly depends on two factors, namely environmental conditions and the stress ratio [29]. For the former factor, this is exemplified in table 3.1 where the threshold value for steel is presented for two different environmental conditions [74]. Notice that austenitic steels, such as AISI 304, deviate from other steels when protected in marine conditions.

Table 3.1: Recommended fatigue crack growth threshold values, K_{th} , for assessing welded joints [74].

Material	Environment	K_{th} [MPa $\sqrt{\text{mm}}$]
Steels, including austenitic	Air ^a	63
Steels, excluding austenitic	Marine ^b	63
Steels, austenitic	Marine ^b	0
Steels, including austenitic	Marine, unprotected	0

^a and other non-aggressive environments up to 100 °C

^b with cathodic protection, up to 20 °C.

Regarding the influence from the stress ratio, scenarios in which tension-tension loading is present will be unfavorable. As shown by eqs. (3.1) to (3.3), introduction of compression stresses increases the threshold value.

$$\Delta K_{th} = 63 \quad \text{for } R \geq 0.5, \quad (3.1)$$

$$\Delta K_{th} = 170 - 214R \quad \text{for } 0 \leq R \leq 0.5, \quad (3.2)$$

$$\Delta K_{th} = 170 \quad \text{for } R < 0, \quad (3.3)$$

where R is the stress ratio found by eq. (4.17). The presented values are applicable in cases where, respectively, the initiation by slip bands are examined and cracks already exist in the structure. Due to this widespread applicability, the presented values are extraordinary conservative for some cases of cracking. If requesting an exact value, it is necessary to introduce experimental testing, e.g. crack tip opening displacement (CTOD), in accordance with the recommendations in ASTM E1681 - 03(2013) and BS ISO 12108.

3 Phase 2: Crack growth

Conventional crack growth occurs when a crack reaches a so-called physical size. Here, the metallurgical composition is essential as the crack needs to obtain a size that is considerable compared to the size of the grains. If the crack size is about the size of a grain, the phase 1 mechanisms are dominating the crack development, as described in section 2.

Since a crack surface displacement occurs, it is relatively simple to monitor damage by observing the crack growth rate. A supervision of the crack size is beneficial because it improves the reliability of the structure and the fatigue estimation. Hence, by increasing the number of inspection intervals, the structural reliability is improved, particularly since cracks can be identified at an early stage. Often, such inspections are carried out by visual observations, making them rather uncomplicated to complete. However, in some cases, the crack is not visible; for instance, when dealing with embedded cracks. In these cases, ultrasound or X-ray surveillance is employed to clarify the cracks size, growth and location, see e.g. [17,91].

It is normal that a structure contains several cracks, of which some are actively growing in size. To observe these cracks, an inspection schedule based on the expected crack growth is outlined, thus it is crucial to be familiar with the crack growth parameters of the material in question.

3.1 Crack growth by Paris' law

In 1961, P.C. Paris introduced a crack growth classification based on a power law relationship between the crack growth rate, $\frac{da}{dN}$, and the stress intensity factor range, ΔK , see [62]. Mathematically, Paris' law is given by

$$\frac{da}{dN} = A(\Delta K)^n \quad (3.4)$$

where ΔK is found through eq. (2.9), while A and n are parameters depending on the material, environment, temperature and stress ratio, respectively. table 3.2 presents the values for A and n for some of the frequently applied materials, see e.g. [8,22,71,75].

Table 3.2: Material parameters for the Paris' law.

Steel	$A \left[\frac{\text{mm}}{\text{cycle}} \right]$	n
S235 [71]	$1 \cdot 10^{-8}$	3.0
S690 [71]	$5 \cdot 10^{-8}$	2.3
AISI 304L [8]	$2 \cdot 10^{-8}$	3.0

3. Phase 2: Crack growth

In fig. 3.11, a log-log plot of crack growth according to Paris' law is presented. Here, the first axis represents the oscillating stress intensity factor, while the second axis is the incremental crack growth length per cycle. K_c is the critical stress intensity level and K_{th} is the threshold value. Specifically, Paris' law describes the linear portion in the log-log plot between the crack propagation and the ΔK , as is evident from eq. (3.4).

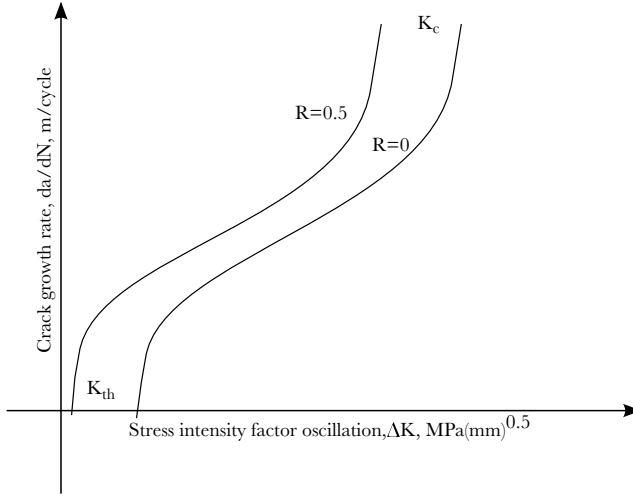


Fig. 3.11: Illustration of crack growth rate in log-log plot.

Paris' law is relatively simple and only includes few parameters. Consequently, the BS7910 "Guide to methods for assessing the acceptability of flaws in metallic structures" suggests using other models, which are based on two slopes instead of the one used in Paris' law.

fig. 3.11 shows that the stress ratio affects the crack growth rate, just as in the case of initiation. Often, an estimation of the number of load cycles to generate a particular amount of crack growth is requested, for instance when determining the inspection intervals. This estimation is obtained directly by integrating eq. (3.4) with respect to crack size growth, yielding

$$N_{if} = \frac{a_f^{1-\frac{n}{2}} - a_i^{1-\frac{n}{2}}}{A(F\Delta\sigma\sqrt{\pi})^n(1-\frac{n}{2})}, \quad (n \neq 2), \quad (3.5)$$

in which, as denoted previously, ΔK is expressed as done in eq. (2.9), and $F = f(\frac{a}{w}) = \text{Constant}$ includes the influence from the geometry, as explained in section 3. In eq. (3.5), a_i and a_f are the start crack size and the final crack size, respectively. Notice that F is constant, hence the stress intensity factor is not affected by the crack growth. This assumption will be invalid if the

crack reaches a considerable size compared to the structure in question. In such cases, the solution can be obtained by introducing steps in which F is updated.

3.2 Crack grow direction

Most structural components contain joints, holes, cutouts and/or other forms of geometric variation that affect the stress distribution. Since the stress field changes, the effect from these geometric variations also contributes to changes in growth rate and direction of nearby cracks. In fig. 3.15, an example of a welding-induced change in the growth direction is presented. This change in direction is of great interest as it significantly increases or decreases the fatigue life. The direction of the propagation is orthogonal to the direction of the maximum hoop stress, which is defined by [26]

$$\cos \frac{\theta}{2} (K_1 \cos^2 \frac{\theta}{2} - \frac{3}{2} K_2 \theta) = 0. \quad (3.6)$$

Today crack growth models are included in FE software, facilitating more complex analysis of the crack growth patch, see e.g. [14, 24, 57].

3.3 Environmental impacts on the crack growth rate

Generally, the environmental conditions affect the crack growth rate. Especially corrosion has a negative effect on the fatigue life due to the induced increase in crack growth rate [18]. An increase in corrosion can be caused by seawater, which in general rushes the corrosion process and thereby causes further attacking on the newly developed crack surface [70]. This emphasizes the potential adverse effects of the surrounding environment and, thus, the need for taking this into account when calculating the crack growth. This is exemplified in figs. 3.12 and 3.13 where the effects of having introduced corrosion is illustrated by showing the crack growth and initiation in normal air conditions and in vacuum. Evidently, the initiation is more severe in air which is due to the introduction of corrosion.

The load frequency also has an impact on the crack growth rate. Indirectly, the frequency influence is related to the environmental conditions, since the newly developed crack surface is open and thereby exposed to corrosion attack for a longer period of time when the load frequency is low. This will, of course, lead to an increase in crack growth rate. It should be noticed that the corrosion itself may introduce cracking, also known as stress-corrosion cracking.

3. Phase 2: Crack growth

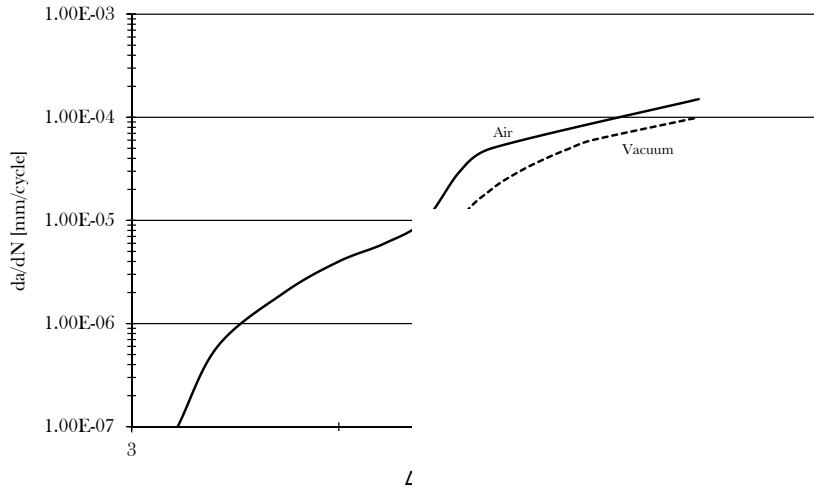


Fig. 3.12: Crack growth in the material Ti-6Al-4. The curves are based on data points from [39].

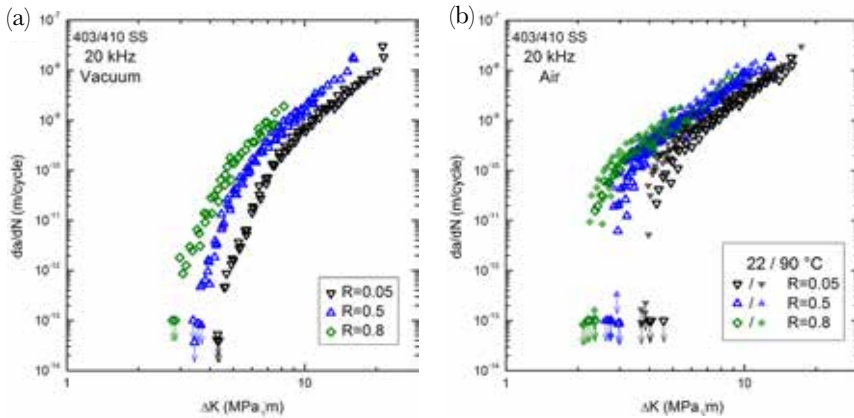


Fig. 3.13: Crack initiation under different environmental conditions. (a) Tested in air at 22 °C. (b) Tested in air at 90 °C [70]. Permission given from author.

3.4 Metallurgical effects in the crack growth rate

The metallurgical composition influences the characteristic crack growth rate. For instance, a crack grows faster in austenitic stainless steel, as AISI 304, compared to martensitic steel. Each material has specific appurtenant crack growth properties. For instance, the crack growth properties for a steel material are typically well-defined on the basis of the exact metallurgical com-

position, i.e. whether it is austenitic, ferritic or martensitic. For other materials and compositions, experiments are needed to clarify the properties. In [49], an example of a mixed metallurgical composition that affects the crack growth is presented. Here, a laser-welded joint of stainless steel, AISI 304, is subjected to an oscillating stress until final fracture occurs. Subsequently, the crack growth is determined by studying the fracture surface, see fig. 3.14, and growth patch, see fig. 3.15. In the current case, the crack initiates at the edge of the specimen and grows towards the area next to the corner of the welding. Afterwards, the grow direction changes and further crack development occurs at the border of the HAZ. This crack growth behavior is, i.a., caused by the higher concentration of martensite in the welded area, which is generated as austenite transforms into martensite in the welding process [49]. In this way, the crack grows faster in the boundary of the HAZ due to a pure austenite composition. Besides the welding, the high rate of stress and strain around the crack tip also introduces a transformation, which is further amplified because of the presence of residual stresses. It should be noticed that this stress- and strain-induced transformation can only occur in a specific temperature interval, cf. [46, 49]. Due to the numerous factors impacting the crack growth, an exact value for this growth is difficult to define, particularly for steel materials such as AISI 304.



Fig. 3.14: Fracture surface of a specimen of AISI 304 laser welded T-joint.



Fig. 3.15: Illustration of crack growth patch, marked by a red, dashed line.

3.5 The influence from the mean stress level and crack closing effect

The mean stress level has influence on the crack growth, see fig. 3.11, especially in cases where the crack is loaded by a tension-tension stress oscillation.

3. Phase 2: Crack growth

Such influence from the stress ratio, R , can significantly change the fatigue life. For instance, $R = 0$ loading increases crack growth compared to $R = -1$ since the former is constituted of only tensile stresses. When loading a crack by tensile stresses, the crack surfaces separate from each other, and the stress intensity factor increases with the load. Conversely, by adding a compression load, the surfaces establish contact with each other and the crack tip experiences no or low change in stress intensity factor, hence emphasizing the importance of the stress ratio. In the present subsection, a method to include such effect in the crack growth analysis is documented.

Methods to estimate the load ratio influence on the crack growth

It is known that the material characteristics have an impact on the influence of the stress ratio. Generally, this impact is bigger for materials with ductile behavior than for brittle materials. Later in the chapter, the phenomenon that causes this influence on the crack growth behavior is presented.

The mean stress effect has been extensively studied [8, 77]. One of the accepted methods for compensating for the mean stress level is the Walker relationship, given by [55]

$$\frac{da}{dN} = \frac{A(\Delta K)^n}{(1 - R)^{n(1-\lambda_R)}}, \quad (3.7)$$

where A and n are material parameters based on Paris' equation [7], R is the stress ratio, see eq. (4.17), and $\lambda_R \in [0.2, 1]$ is a material constant which is frequently set to 0.5 for steel materials [21].

Besides the Walker relationship, several methods for including the stress ratio in the crack growth calculation exist. For instance, the Donahune et al. law [20]

$$\frac{da}{dN} = C(\Delta K - \Delta K_{th})^m, \quad (3.8)$$

which takes into account K_{th} and hereby includes the behavior from the initiation phase. This is preferable when estimating the crack growth rate for small cracks.

In case of large cracks, the Forman equation, i.e. [28]

$$\frac{da}{dN} = \frac{C_f \Delta K_f^n}{(1 - R)K_c - \Delta K}, \quad (3.9)$$

can be applied when estimating the crack growth in the K_c region. Here, it is noticed that C_f and n_f are material constants of the same types as those in the Paris' law, but of different values [11].

The Elber Crack closure method, primarily developed to predict fatigue crack growth under flight simulation loading [43], can also be applied [25]. This is given by

$$\frac{da}{dN} = C\Delta K_{\text{eff}}^m, \quad (3.10)$$

in which ΔK_{eff} is the effective stress intensity factor based on the crack closure mechanism.

In fig. 3.16, the effect of using the Walker relationship (eq. (3.7)) and the Donahue et al. law (eq. (3.8)) compared to Paris' law (eq. (3.4)) is exemplified for different load cases. Notice that the growth behavior by Donahue et al. law includes the K_{th} and therefore also describes the initiation phase. Additionally, it is seen that a crack grows slower when loaded with a ratio of $R = -1$.

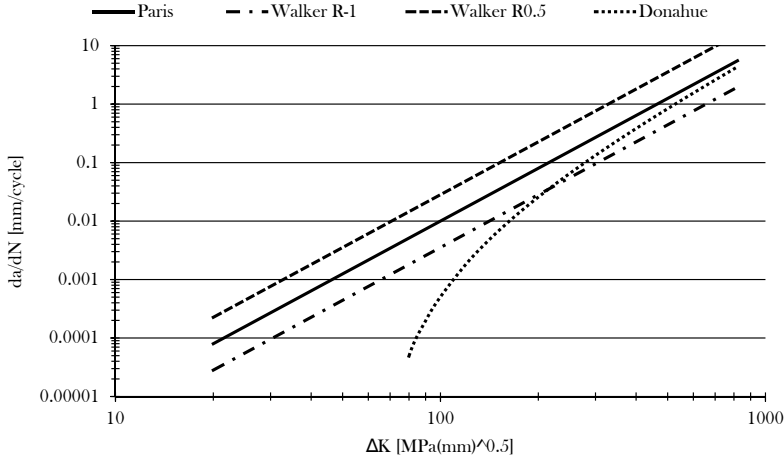


Fig. 3.16: Fatigue crack growth rate vs ΔK according to different laws.

4 Fracture toughness K_c , K_{Ic}

As described in section 2, a crack can become unstable in accordance with the energy criterion. Here, K_c is introduced as the value to designate this transition between stability and instability. Thus, when K_c is exceeded, final fracture of the structure or component in question occurs. Normally, when such failure occurs, the structure or component loses the ability to operate. Therefore, this stage of the fatigue damage has extensive consequences, for instance if a member in a structure fails by fracture which, potentially, can

4. Fracture toughness K_{Ic} , K_{Ic}

lead to a total collapse of the structure. This final stage of crack growth is often the only one associated with fracture mechanics as a term, despite that a cracking progress has taken place in a while before the failure.

The ability of a material to resist fracture failure, in the form of unstable crack growth, is known as fracture toughness. Here, the fracture toughness is related to the impact energy. In proportion to the value of the fracture toughness, the general conception is that hard materials have low toughness and materials with low hardness have high toughness.

Besides the material hardness, the environmental conditions, especially the temperature, also affect the fracture toughness. This temperature dependency is illustrated in fig. 3.17 where it is noticed that a transition temperature interval exists. In this temperature interval, the fracture toughness changes dramatically when the temperature changes slightly, thus it is essential to use material data which are obtained under the same conditions as expected for the practical applications. Fracture toughness data can be obtained in literature such as [22,35,75]. Additionally, it is advantageous to determine the fracture toughness by experiments covering crack tip opening displacement (CTOD) testing. As a last measure, the fracture toughness can be calculated by use of norms such as ASTM E399, BS 7448 and BS EN ISO 12737.

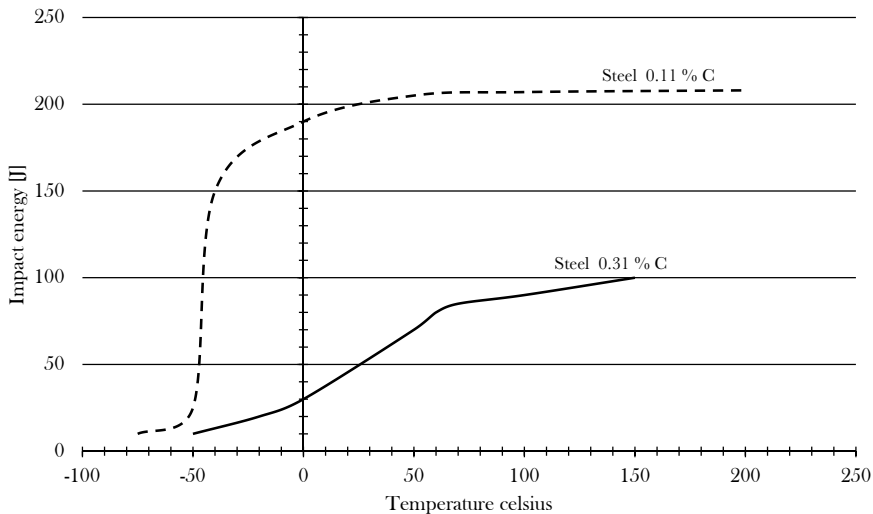


Fig. 3.17: Impact energy vs temperature for steels with different content of carbon.

Two stages of limited material capacity cause the failure mechanism; either brittle or ductile failure. As mentioned previously, materials can fail due to the accumulated energy, hence characterizing a brittle failure. Occasion-

ally, the stress level at the crack tip may introduce extensive plastic strains, hereby leading to a ductile failure. Furthermore, failure can also be a combination of the two mechanisms, i.e. as in a mixed mode condition. This mode frequently occurs in practical fracture mechanics, leaving a fracture surface with a slant plane, indicating ductile failure, and also a flat plane, indicating brittle failure.

Another factor that affects the fracture toughness of a specimen is its thickness. This is due to the variability in stress condition, i.e. whether there is plane stress or plane strain at the crack tip. Plane stress condition always occurs at the surface and the area next to the surface since $\sigma_{33} = 0$. In the case of a relatively large plate thickness, plane strain condition, i.e. $\epsilon_{33} = 0$, arises at the crack tip. In fig. 3.18, the thickness-dependency of the fracture toughness is depicted.

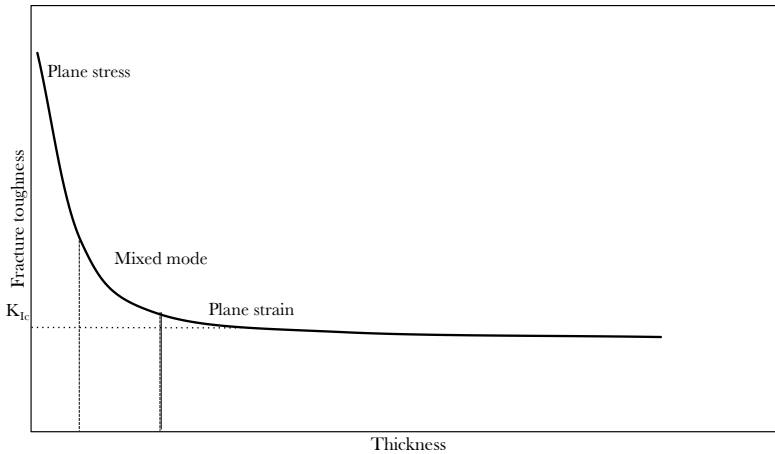


Fig. 3.18: Thickness-dependency of the fracture toughness.

Due to the different mechanisms of the crack tip stresses, a dissimilar yielding zone occurs in plane stress conditions compared to plane strain conditions. Consequently, the critical size of a crack depends on the thickness. Therefore, a critical stress intensity factor is often presented as K_{Ic} , which is the fracture parameter in condition of pure plane strain. Frequently, the K_{Ic} is applied as K_c because it is a conservative estimation of the risk for failure.

In the case of material testing, linear elastic fracture mechanics (LEFM) condition has to be satisfied. This requires that the dimensions of the specimen should be substantially larger than the yielding zone, as defined by

4. Fracture toughness K_c , K_{Ic}

[22,23]

$$B \geq 2.5 \left(\frac{K_{Ic}}{\sigma_y} \right) \quad \text{and} \quad a \geq 2.5 \left(\frac{K_{Ic}}{\sigma_y} \right). \quad (3.11)$$

Here, B is the specimen thickness and a is the crack length. These boundaries for using LEFM are based on the limited plastic zone at the crack and shall be regarded as a guideline. Generally, it is a question of whether a crack causes yielding of the material before fracture or causes brittle fracture before yielding. As presented earlier, the shape of the crack tip stress depends on whether plane strain, i.e. a triaxial stress stage, plane stress, i.e. a biaxial stress stage, or a mixed mode condition is present.

The yielding zone can be illustrated by von Mises multiaxial yield criteria and the stress field equations, see eqs. (2.17) to (2.19). In fig. 3.19, the plastic zone is shown with visualization of the plane stress and plane strain conditions at the yield zone. These yield zone conditions can be estimated by

$$r_p(\theta) = \frac{K_1}{4\pi\sigma_{ys}^2} \left[\frac{3}{2} \sin^2 \theta + (1 - 2\nu)^2 (1 - \cos \theta) \right]; \text{ for Plane strain} \quad (3.12)$$

and

$$r_p(\theta) = \frac{K_1}{4\pi\sigma_{ys}^2} \left[1 + \frac{3}{2} \sin^2 \theta + \cos \theta \right]; \text{ for Plane stress.} \quad (3.13)$$

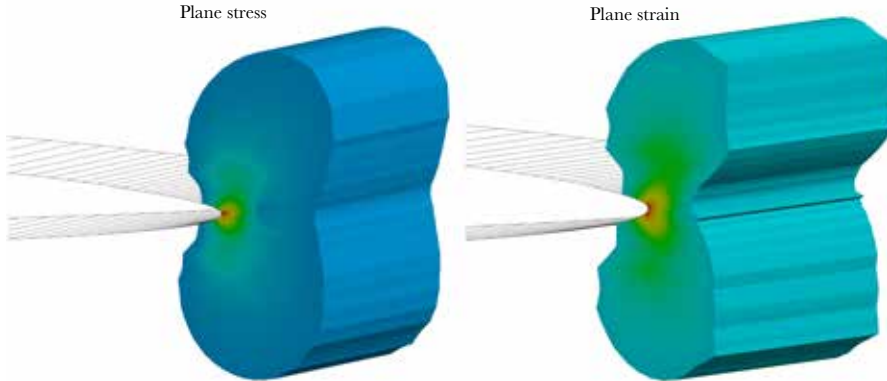


Fig. 3.19: The plastic zone in condition of plane stress and plane strain.

4.1 Estimation of the fracture toughness by V-notch testing

If fully testing of the fracture toughness is infeasible, the fracture toughness can be estimated on the basis of a Charpy V-notch test. The impact energy from the V-notch is related to the fracture toughness by

$$K_{\text{mat}} = \left[(12\sqrt{C_v} - 20) \left(\frac{25}{B} \right)^{0.25} \right] + 20, \quad (3.14)$$

where K_{mat} is the fracture toughness in $\text{MPa(m)}^{0.5}$, B is, as mentioned previously, the material thickness, and C_v is the result from the Charpy V-notch test in joules. Due to the temperature-dependency of the fracture toughness (increase in temperature yields increase in fracture toughness), it is assumed that the same temperature is present during testing and application. However, as uncertainties inherently exist in this assumption, it is recommendable to use the result obtained by eq. (3.14) in a conservative manner. If a non-conservative estimation is conducted, there will be a risk of overestimating the critical crack size.

The temperature-dependency can in fact be taken into direct account by use of

$$K_{\text{mat}} = 20 + \left[11 + 77e^{0.019(T-T_0-T_k)} \right] \left(\frac{25}{B} \right)^{\frac{1}{4}} \left[\ln \left(\frac{1}{1-P_f} \right) \right]^{\frac{1}{4}}, \quad (3.15)$$

where T is the application temperature, T_0 is the temperature for a median toughness of $100 \text{ MPa}\sqrt{\text{m}}$ in 25 mm thick specimens, see eq. (3.16) and eq. (3.17), and T_k is the temperature term that describes the scatter in the Charpy versus fracture toughness correlation. For a standard deviation of 15°C and 90 % confidence, $T_k = +25^\circ\text{C}$ [74].

$$T_0 = T_{27J} - 18^\circ\text{C} \quad (\text{standard deviation} = 15^\circ\text{C}). \quad (3.16)$$

$$T_0 = T_{40J} - 24^\circ\text{C} \quad (\text{standard deviation} = 15^\circ\text{C}). \quad (3.17)$$

This estimation is generally feasible in case of tests with ferritic steel or steel with high crystallinity ($\sim 70\%$).

Estimation of the fracture toughness by means of the impact energy from V-notch testing is an approximation. Usually, the estimates obtained by eq. (3.14) or eq. (3.15) correspond very well to the true fracture toughness.

4. Fracture toughness K_c , K_{Ic}

In order to secure that a non-conservative estimation is not conducted, the largest obtainable value for the fracture toughness can be calculated by

$$K_{\text{mat}} \leq 0.54C_v + 55. \quad (3.18)$$

Example: Calculation of K_{Ic} in a 1 mm and 25 mm plate of S235J0

In this example, the fracture toughness is estimated for two plate thicknesses, namely 1 mm and 25 mm. The material used in this example is S235J0, where the impact energy by a Charpy V-notch test is 27 joules at 0 °C. By substituting this value into eq. (3.14), the fracture toughness values for the 1 mm and 25 mm plates are found to be $114.7 \text{ MPa}\sqrt{\text{m}}$ and $62.35 \text{ MPa}\sqrt{\text{m}}$, respectively, hence emphasizing the considerable influence of the plate thickness. The maximum fracture toughness is found by use of eq. (3.18), and here the result is $69.58 \text{ MPa}\sqrt{\text{m}}$. Thus, the result of $114.7 \text{ MPa}\sqrt{\text{m}}$ is rejected as the value exceeds the maximum.

Chapter 4

Fatigue in materials and estimation of the S-N curve

1 Introduction to Fatigue

It has been observed for many years that materials can fail due to loads that oscillate. Fatigue failure was first methodically investigated in the 1840s and 1850s. At the time, it was unintelligible why some train shafts failed during ordinary operations [75]. In particular, people did not understand why a shaft failed after it had been operating for a certain distance. The breakdown was not triggered by ductile failure since the load was documented to be significantly lower than the yielding strength of the material.

At this time, the material strength was recorded on the basis of static testing and observations, thus all documentation of the shaft strength was on the basis of material parameters, such as yield strength and ultimate strength. Consequently, engineers did not take into account the rotation of the shaft, which created a fluctuation in the location of the maximum stress point. This stress oscillation develops cyclically with the rotation of the shaft, meaning that the stresses at a point on the shaft vary so that it is loaded both in compression and tension in one rotation. It has been found through experience and testing that the strength towards such fluctuating loading is significantly lower than the strength towards static loading, i.e. yield and ultimate strength. Therefore, the term fatigue strength was introduced; a strength that is determined on the basis of the number of stress oscillations and the amplitude of cyclic loading. fig. 4.1 shows a steel shaft that has failed due to fatigue. It is noticed how the fracture surface is different from a ductile failure.

In practice, the fatigue strength is determined by carrying out experi-



Fig. 4.1: Fatigue failure of a steel shaft which has been exposed to a bending moment and rotation, similar to loading of train shafts.

ments similar to the ones used to identify the yield, or ultimate, strength of a material. In the case with the train shaft, the test is established by applying a bending moment and subsequently rotating the shaft. This setup introduces stresses that will vary during the rotation, thereby creating an oscillating stress amplitude. A material loaded by oscillating stresses is bound to experience fatigue failure down to half of the ultimate strength, see eq. (4.4).

Failure caused by these comparatively low-stress oscillations were unsuspected, and this finding helped clarifying the new fatigue-associated material strength. One of the pioneers, August Wöhler, systematically scrutinised the fatigue phenomenon and thereby advanced the method to specify the fatigue strength. He invented a diagram with the relationship between stress oscillations and the number of cycles before failure occurs, also known as the Wöhler diagram. Oftentimes in modern literature, the Wöhler curve is denominated as the S-N curve, where S is the stress range and N is the number of cycles. Notice that the stress range is used instead of the stress amplitude; such representation of the second axis is commonly used in fatigue recommendations. fig. 4.2 shows an S-N diagram constituted by data points from [48].

This S-N approach provides a comparatively simple method to determine the potential of a material to resist oscillating stresses. By plotting the results from a fatigue experiment in an S-N diagram, it will be clear that there is an exponential relation between the stress amplitude and the number of cycles before failure occurs, see fig. 4.2. Thus, if adding a trend line based on the

1. Introduction to Fatigue

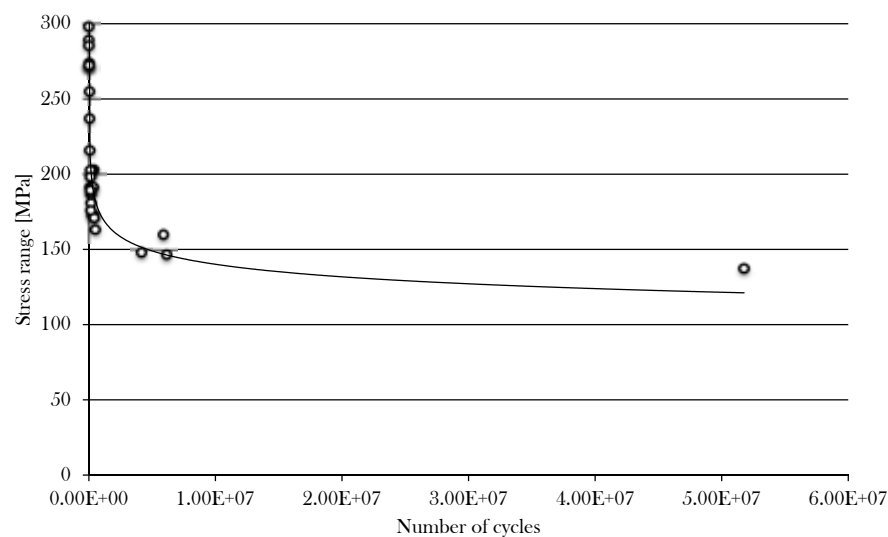


Fig. 4.2: Plot of the fatigue data points in an S-N diagram. The data points in the graph are from [48]

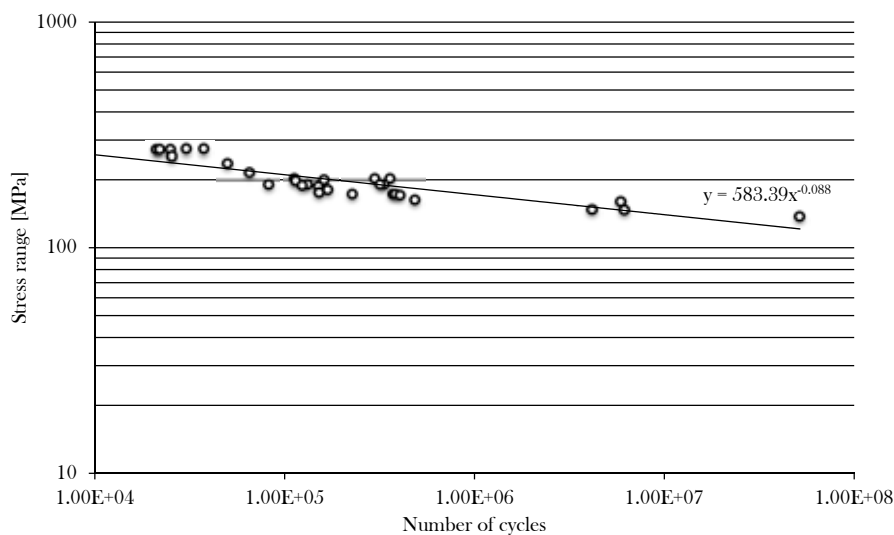


Fig. 4.3: Plot of fatigue data points in a log-log S-N diagram, with a trend line added. The data points in the graph are from [48].

experimental results in a log-log diagram, a straight line appears as showed

in fig. 4.3. Basquin introduced such line in the diagram in 1910 by use of [5]

$$S_a = A(N_f)^B, \quad (4.1)$$

where S_a is the stress amplitude, N_f is the number of cycles before failure, and A and B are the coefficients for the fitted line. However, it is an invalid approximation to use a one-slope curve to the entire range of cycles, i.e. 0 to 10^8 cycles, since different mechanisms dominate specific cycle intervals. This is, thus, taken into account by changing the slope of the S-N curve in correlation with the different regions in the diagram. In total, three regions exist, namely low- and high-cycle fatigue plus the endurance limit, cf. [75]. However, normally, recommendations present S-N curves consisting of only the two latter slopes. For more information, the reader is referred to norms such as EUROCODE 3, DNV-RP-C203 and BS7910.

2 Estimation of the fatigue life for non-welded materials

It is possible to theoretically create an S-N curve based on ordinary material data, which hereby enables estimation of the fatigue life for a specific material without conducting experiments, see e.g. [22, 60, 75]. Since the basis for creating a curve is a single material parameter, in the form of either σ_{ut} or σ_y , some deviations occur between the estimation and the actual fatigue life. Therefore, the method should be used with thoughtfulness, but usually, the method is a helpful guidance for estimating the expected fatigue life.

When theoretically creating the S-N curve, based on high cycle fatigue, an upper limit for the maximum allowable stress amplitude, denoted as S_p , is set for a number of cycles corresponding to 10^3 . In particular, this yields a point on the S-N curve that can be found by [60]

$$S_{p,10^3} = 0.9\sigma_{ut} \quad (4.2)$$

for bending loading, or by

$$S_{p,10^3} = 0.75\sigma_{ut} \quad (4.3)$$

for axial loading. Subsequently, a corresponding lower limit for the maximum allowable stress amplitude, denoted as S'_f , is determined on the basis

2. Estimation of the fatigue life for non-welded materials

of the endurance limit point, typically 10^6 cycles. For steel, S'_f is found as

$$S'_f = 0.5\sigma_{ut}. \quad (4.4)$$

However, some materials, e.g. aluminum and copper, do not have a true endurance limit. In these cases, S'_f is found at 5×10^8 cycles by use of

$$S'_f = 0.4\sigma_{ut}, \quad (4.5)$$

which is applicable in a certain range of σ_{ut} . For copper and aluminum this range is exceeded for $\sigma_{ut} > 280$ MPa and $\sigma_{ut} > 330$ MPa, respectively. In these cases, a stress amplitude of, respectively, 100 MPa and 130 MPa should be employed. It should be noticed that eqs. (4.4) and (4.5) are based on bending-rotation fatigue testing with polished specimens. Thus, the influences of surface, thickness and environment are neglected.

Adjusting of the S-N curve to the environment condition and other effects

Since eqs. (4.4) and (4.5) do not include surface- and size-induced effects, albeit they significantly affect the fatigue life, adverse errors can occur in the fatigue estimation. To overcome this, factors taken into account the aforementioned effects can be included to constitute

$$S_f = C_{load} C_{size} C_{surface} C_{temp} C_{reliab} S'_f \quad (4.6)$$

in which the factors $C_i \in]0,1]$ correlate for the following effects: load, size, surface, temperature and reliability.

Load factors C_{load} changes in accordance to the type of load subjected in the application. Below, the values are listed for bending, axial and torsional loading.

$$C_{load} = \begin{cases} 1 & \text{for bending} \\ 0.7 & \text{for axial} \\ 0.29 - 0.577 & \text{for torsion} \end{cases}. \quad (4.7)$$

As seen in eq. (4.7), bending loading does not affect the fatigue life. Contrary, it is evidenced that axial and torsional loading reduce the fatigue resistance significantly. For axial loading, the resistance is reduced by 30 %, whereas the reduction due to torsion is somewhere between 48-71 %, depending on the source. fig. 4.4 shows a torsion fracture of two shafts.



Fig. 4.4: Torsion fracture in two shafts

When combined loading cases exist, the von Mises stress criterion, see eqs. (4.8) and (4.9) for two- and three-dimensional cases, can be used to calculate C_{load} . This is done by normalizing the criterion with regards to the yielding stress, σ_y . Hereby, it can be found that torsion in a combined stress case yields $C_{\text{load}} = 0.577$ [60].

$$\sigma_{\text{eq}} = \sqrt{\sigma_x^2 + \sigma_y^2 - \sigma_x \sigma_y + 3\tau_{xy}^2} \quad (4.8)$$

and

$$\sigma_{\text{eq}} = \sqrt{\frac{(\sigma_x - \sigma_y)^2 + (\sigma_y - \sigma_z)^2 + (\sigma_z - \sigma_x)^2 + 6(\tau_{xy}^2 + \tau_{yz}^2 + \tau_{zx}^2)}{2}}. \quad (4.9)$$

Size effects As described in section 4, the thickness of the components affects the stress conditions around a crack and therefore also the fatigue life. Consequently, the thickness has to be taken into account when estimating the fatigue life. In addition to this fracture mechanical aspect, the risk for internal flaws, e.g. foreign objects, increases with a larger thickness, hereby contributing to the fatigue life reduction. By use of

$$C_{\text{size}} = 1 \quad \text{for } d < 8 \text{ mm} \quad (4.10)$$

and

$$C_{\text{size}} = 1.189d^{-0.097} \quad \text{for } 8 \text{ mm} < d < 250 \text{ mm}, \quad (4.11)$$

2. Estimation of the fatigue life for non-welded materials

the size effect is included in the fatigue life estimation. Since this size effect is based on cylindrical parts, it was suggested in [45] that an equivalent value for the diameter is found for non-circular cross sections by use of

$$d_{\text{equiv}} = \sqrt{\frac{A_{95}}{0.0766}}, \quad (4.12)$$

where A_{95} is the cross-sectional area stressed above 95 % of its maximum stress. As an example, $A_{95} = 0.05bh$ for a rectangular cross section with width b and height h . In case of other cross sections, the corresponding A_{95} can be found in [45]. It should be noticed that, as for circular cases, if the diameter is over 250 mm, the size factor is set to $C_{\text{size}} = 0.6$.

Surface factor As mentioned previously, the values used in eqs. (4.4) and (4.5) are obtained for a rotating shaft with a surface polished to a mirror finish. Under these conditions, the surface imperfections are removed such that the specimen has an extraordinary high fatigue resistance. Therefore, it is essential to adjust the fatigue resistance by use of C_{surf} , because the surfaces usually are rougher than polished to a mirror finish. Values for C_{surf} can be found in, e.g., [60,75]. In [60], the curves plotted in fig. 4.5 are applied to estimate C_{surf} based on the ultimate strength.

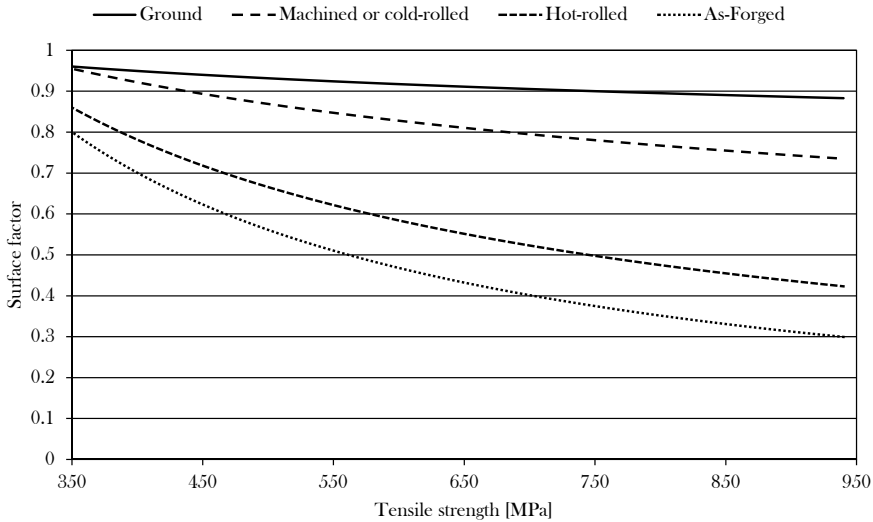


Fig. 4.5: Surface finish effects on the fatigue factor.

As shown in fig. 4.5, C_{surf} depends on the ultimate strength and also

the manufacturing process. For instance, a machined surface performs better than an as-forged surface, since the latter contains a higher amount of flaws. This emphasizes the importance of distinguishing between manufacturing process. Actually, this can be taken a step further as it is possible to differentiate between roughnesses of different machined surfaces and hereby additionally fine-tune the fatigue estimation, see [60].

Temperature Normally, most fatigue testing is conducted in room temperature, which means that the fatigue parameters only are valid in case of estimation in approximately same temperature interval. Therefore, a correlation of the fatigue data is needed in case of significant deviation between the testing temperature for the material data and the actual temperature for the application in use. In [60] it is suggested to include the temperature effect by

$$C_{\text{temp}} = 1 \quad \text{for } T < 450 \text{ }^{\circ}\text{C} \quad (4.13)$$

and

$$C_{\text{temp}} = 1 - 0.0058(T - 450) \quad \text{for } 450 \text{ }^{\circ}\text{C} < T < 550 \text{ }^{\circ}\text{C}, \quad (4.14)$$

where T is the temperature of the application. Evidently, the temperature needs to be very high before the fatigue life is substantially affected by this parameter when employing eqs. (4.13) and (4.14). This insensitivity is also stated in the norms; for instance, in DNV-RP-C203 where the fatigue data is not affected by temperature variations between the room temperature and 100 °C.

Reliability An estimated S-N curve based on the method and material parameters described in the present section yields a curve with a 50 % reliability for survival. This probability of survival is relatively low and unusable if requested, as in most cases, that the fatigue estimation is based on a safe design approach. Therefore, statistical evaluation is utilized for creating a curve in which the majority of the components survive the estimated number of cycles. Typically, a 5 % probability of failure or less is introduced to minimize the risk for failure.

In [34], it is found that the endurance strength of steel has a standard deviation of 8 %. Based on this, a table can be made for the reliability factors, as done in table 4.1.

As mentioned, table 4.1 is based solely on data from the endurance strength. The corresponding C_{reliab} factors for other cycles can, in lack of specific data

2. Estimation of the fatigue life for non-welded materials

Table 4.1: The reliability factor based on a 8 % standard deviations of the mean values.

Reliability %	50	90	99	99.9
C_{reliab}	1	0.897	0.814	0.753

for this location on the S-N curve, be calculated by use of the standard deviation for the endurance strength. This approach is useful as the assumption is conservative due to less deviation at lower number of cycles.

Example: estimation of the S-N curve for S355 and CuNi10

In this example, the S-N curves are estimated for two materials, namely construction steel S355 and a copper alloy CuNi10. The ultimate strength of S355 is $\sigma_{\text{ut}} = 530$ MPa and $\sigma_{\text{ut}} = 350$ MPa for CuNi10.

The steel application is a plate with a cross-section of 10 mm \times 100 mm, which is subjected to bending. In table 4.2, the results of the fatigue estimation of the plate are presented along with the found C factors. The equivalent diameter was estimated to 25.5 mm.

For the copper material, a similar plate, i.e. 10 mm \times 100 mm cross section, is subjected to axial loading. In table 4.3, the results are presented.

Table 4.2: The C factors (those omitted are set to 1) and the results of the fatigue estimation of a steel plate, in case of bending.

σ_{ut}	$S_{p,10^3}$	S'_f	S_f	C_{size}	C_{surface}
530 MPa	477 MPa	265 MPa	99.2 MPa	0.634	0.59

Table 4.3: The C factors (those omitted are set to 1) and the results of the fatigue estimation of a copper plate, in case of axial loading.

σ_{ut}	$S_{p,10^3}$	S'_f	S_f	C_{load}	C_{size}	C_{surface}
350 MPa	262.5 MPa	140 MPa	73.1 MPa	0.7	0.77	0.96

As an addition to direct presentation of the obtained results, see tables 4.2 and 4.3, the appertaining S-N curves, both with and without inclusion of C factors, are depicted in fig. 4.6. Evidently, the C factors affect the fatigue life significantly.

The plots in fig. 4.7 show the S-N curves for the steel plate with three other reliabilities of survival, namely 50 %, 90 % and 99.9 %. In this case, it is assumed that the standard deviation is constantly 8 % throughout the entire range of the S-N curve. The example demonstrates how to estimate an

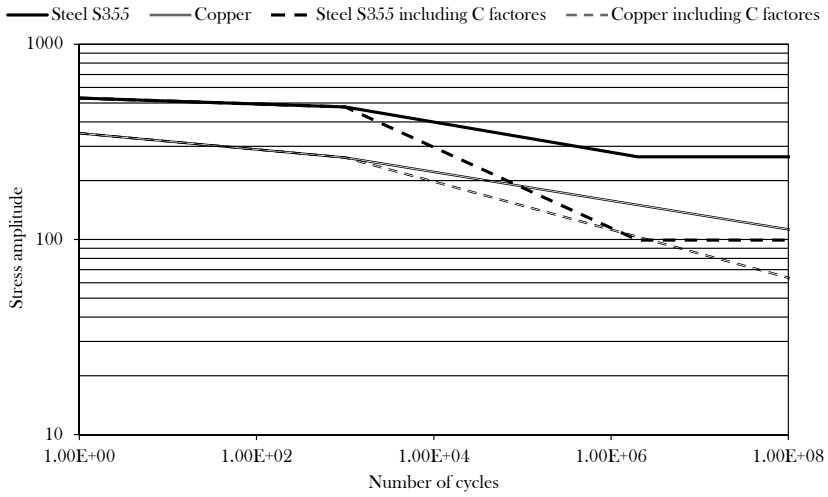


Fig. 4.6: Surface finish-governed effects on the fatigue factor [60].

S-N curve by use of standard material parameters. The presented method is applicable for computing an estimate of the fatigue in cases where a limited amount of material data is available.

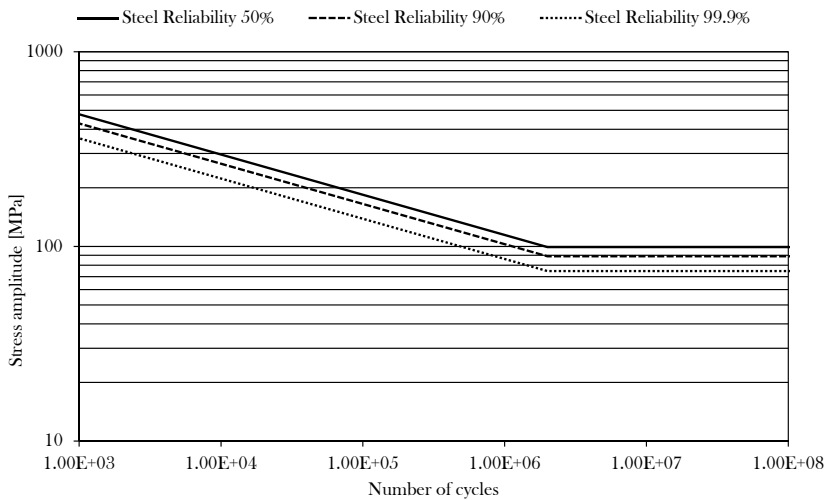


Fig. 4.7: S-N curves for a steel material with different reliabilities of survival.

3 Fatigue life estimation by norms

In common norms, the fatigue estimation is based on the S-N approach with appurtenant design categories. In the case of using the S-N approach, the procedure is to estimate the fatigue life by choosing a design category and subsequently finding the appurtenant S-N curve. Hereby, the method includes the effect from the structural detail since the curves depend on the design category. Thus, it is crucial to select a design category that matches the current structure or joint. fig. 4.8 shows a design category from DNV-RP-C203. Notice the notation of the design category which, in the present case, is C2. This represents a specific design category.

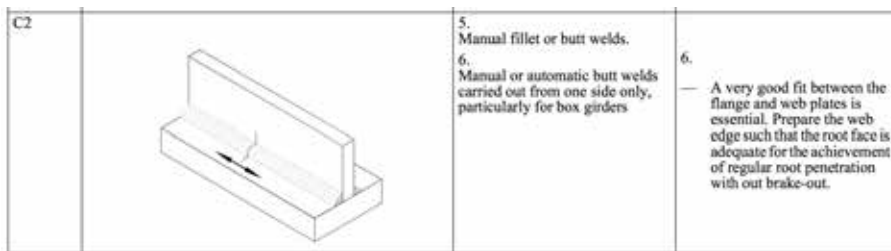


Fig. 4.8: Design category C2 with constructional details from DNV-RP-C203 [19].

The importance of choosing the correct design category is evidenced by comparing an unfavorable design category to a suitable one in proportion to fatigue. This is done in fig. 4.9, where fatigue properties are presented for the two design categories illustrated in fig. 4.10. Here, the most robust design, i.e. C1, has a fatigue limit of 10^7 cycles at a stress range of 65.5 MPa, whereas the weakest, i.e. W3, allows a stress range at only 21.05 MPa for this particular amount of cycles.

Effects of environment

The design category is the main parameter for the estimation of fatigue life, but environmental conditions also have a significant influence on fatigue life [35]. Accordingly, there are separate curves for the design category in air and seawater. Furthermore, including other factors, such as temperature, thickness effects and fabrication tolerance, improve the accuracy of the estimation, and therefore it is normally possible to compensate for these effects by use of procedures from the norms [22].

Because the factors mentioned above influence fatigue life but complicate estimation, it is essential to consider the relevance of including them in the estimation. Obviously, more sophisticated knowledge about the structural details facilitates better accuracy of fatigue life estimation.

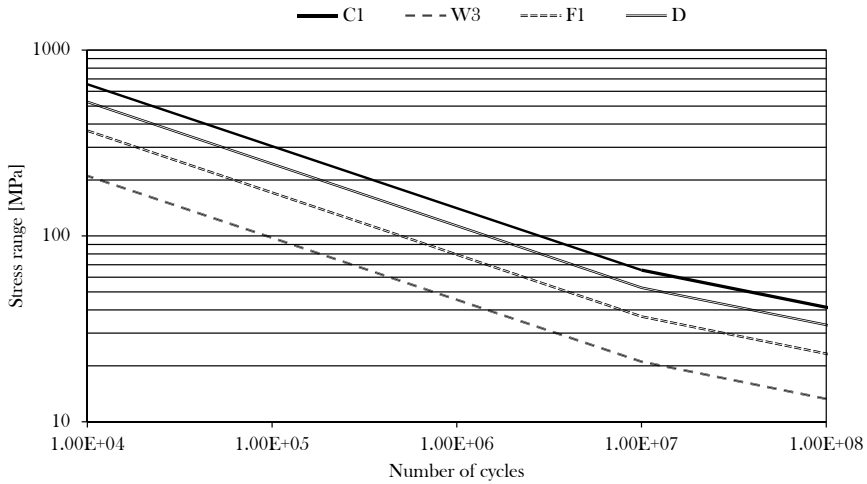


Fig. 4.9: S-N curves in air from DNV-RP-C203.

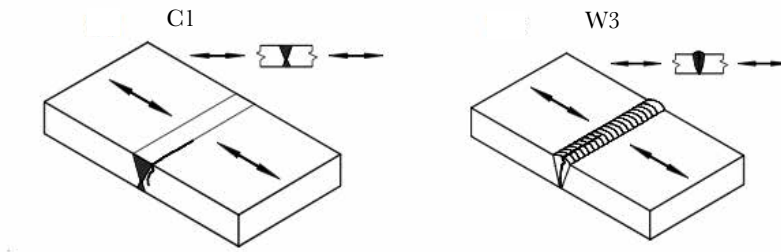


Fig. 4.10: Two design categories, namely 1) C1, a butt weld which is proved free from significant defects by non-destructive examination, and 2) W3, a butt weld made from one side only and without backing strip.

Fabrication misalignments

It is possible to compensate or set a guide for fabrication misalignments. This is done by defining fabrication rules concerning the allowed tolerances, which are useful in proportion to setting up a production line. Since fabrication normally contains misalignments, a moderate level of fabrication tolerance is already contained in the norms. An example is given when using the basic assessment from DNV-RP-C203 to estimate the fatigue life for a 10 mm butt-welded plate. In such case, a misalignment up to 1 mm is allowed. If the fabrication errors are documented to be less than 1 mm, it is conceivable to adjust the S-N curve and thereby extend the fatigue life. This exemplifies the benefits of the available knowledge about the design and production.

4. Load Categorization in case of fatigue estimation

However, as mentioned previously, the principal factor is the design of the structural detail, thus it is essential to choose the correct design category before anything else.

Probability of failure

Besides the design category, the expectation regarding the probability of failure when estimating the fatigue life with an S-N approach must also be addressed. Producing the curve through experimental testing, and the curve being based on such a data set, will cause the curve to have a 50 % chance of failure if no further action is taken. This probability for failure is, in most cases, unacceptable. Therefore, statistical evaluation is introduced by means of providing a confidence interval and decreasing the probability of failure.

In engineering cases, failure is generally unwanted; therefore, statistical evaluation is used to produce a curve which represents a specific probability for failure, and where the risk for failure is significantly low. For instance, the S-N curves in DNV-RP-203 are produced on the basis of a 97.7 % probability of survival with at least 75 % confidence [38,88], whereas the EUROCODE 3 fulfills a 95 % probability of survival.

4 Load Categorization in case of fatigue estimation

It is common to consider structural loads as stochastic variables. First of all, fluctuations occur in the load size, depending on the load source. For example, a structure placed in an offshore environment is subjected to a large loading variation due to the wind and waves. Conversely, it is typically a more constant amplitude of loading oscillation when treating rotating machinery. Lastly, in some cases, the size of the loading variation is insignificant, for instance, in some civil buildings.

Besides the amplitude, other load parameters, such as frequency and mean stress level, may also vary. These loading factors will, thus, also affect the fatigue damage. In general, two parameters are always considered when fatigue loading is analyzed, namely the stress amplitude and the mean stress level. Norms often use the stress range, ΔS , which is related to the stress amplitude, S_a , simply by

$$S_a = \frac{\Delta S}{2}. \quad (4.15)$$

The mean stress level, S_m , is determined by

$$S_m = \frac{S_{\max} + S_{\min}}{2} \quad (4.16)$$

where S_{\max} and S_{\min} are the maximum stress and the minimum stress, respectively.

Frequently, the literature employs the stress ratio, R , in order to determine the mean stress level. This is done via

$$R = \frac{S_{\min}}{S_{\max}}, \quad (4.17)$$

thus when $R = -1$, the loading is called "fully reversed" because $S_{\max} = |S_{\min}|$, and "pulsating tension" when $R = 0$ as $S_{\min} = 0$.

5 Fatigue in polymers and composites

Polymers are used extensively in almost all fields of industries. One of the major advantages with this material type is the possibility of mass-producing rather complex components. Since polymers are utilized in a wide range of products, different material properties are demanded [51]. One of these properties is the fatigue resistance, which depends on different parameters. Thus, it is essential to understand the fatigue damage generated in polymers when designing an application. fig. 4.11 shows a fracture surface from an application that failed during cyclic loading. Notice the similarity to the steel fracture surface, see fig. 4.1.



Fig. 4.11: Polymer application with failure caused by stress oscillation.

In general, monotonic failure occurs in polymers at lower stress levels than those for steel [69], thus the allowed stress oscillation is in this respect less for polymers. In fig. 4.12, S-N curves for some polymer materials are given. Notice the significant difference in fatigue life for the presented polymer materials.

An example of a polymer application, which will be highly affected by stress oscillation, is a patch layer [2]. fig. 4.13 shows a patch layer which is applied to a surface containing an edge crack. By applying this patch layer, it most likely causes reductions in the crack growth. This reduction is obtained as the patch layer will relieve the stresses at the crack front, resulting in strains being transferred to the patch layer, which, therefore, generates

5. Fatigue in polymers and composites

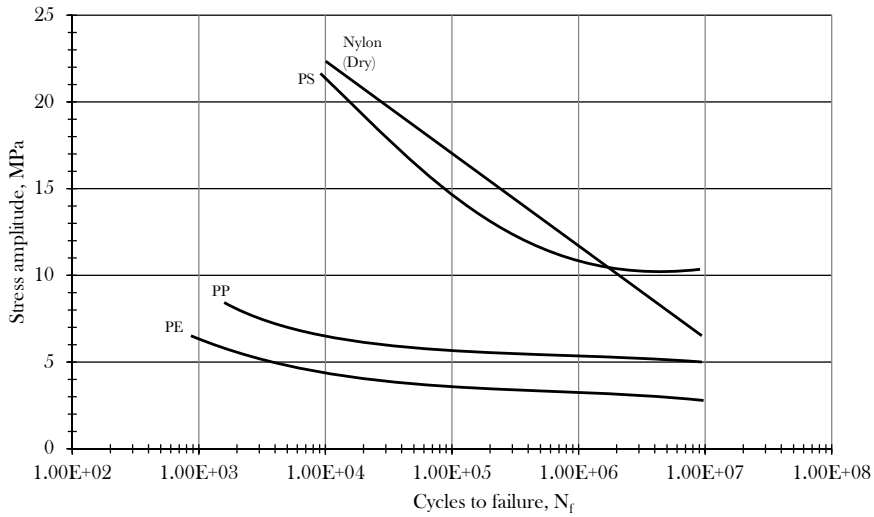


Fig. 4.12: Stress-life curves for several polymers tested at a frequency of 30 Hz. Sources [51]

damage to this polymer material. In this respect, it is crucial to use a patch layer with sufficient fatigue resistance. If this is not ensured, the patch layer might fail before it yields any noticeable impact on the crack growth. Generally, it is essential to understand in which particular cases the overall fatigue properties will benefit from adding a patch layer. This can be explored by using FEA, see [50,52]. fig. 4.13 shows a stress plot of a FEA setup of a patch layer application.

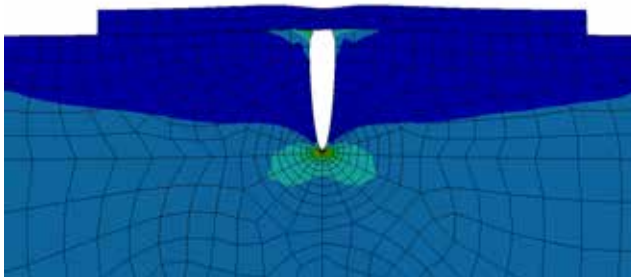


Fig. 4.13: Effect of adding a polymer patch layer to a cracked steel component [50].

5.1 The fatigue properties of polymers and environmental effect

If comparing the fatigue characteristics for steel and polymers, it can be seen that many of the same parameters affect the fatigue life. For example, the mean stress level affects the fatigue life in both steel and polymer applications. However, the magnitude of the fatigue life impact varies significantly when dealing with steel materials and polymers. This can be exemplified by studying the loading frequency affect; when considering the fatigue life in steel, the loading frequency is of relatively insignificant importance. On the contrary, this constitutes one of the main parameters when considering fatigue in polymers.

Generally, cracks in polymers have a comparatively long growth life, making this of significant importance for the total fatigue life. The growth life of cracks in polymers can, however, be influenced severely by other effects, e.g. heating. This heating weakens the material and therefore reduces the fatigue resistance, implying a correlation between the loading frequency and the generated heat at the crack front. In particular, this heating arises due to internal friction which occurs even at low loading frequencies, and since polymers in general have poor conducting properties, the heat will be accumulated locally. Thus, a material which has very low internal friction, such as polystyrene (PS), is not subjected to as much heating, meaning that the frequency dependency is low. This is shown in [69] where fatigue tests at 1600 cpm generated a temperature rise less than 2 °C. On the contrary, for materials with high internal friction, such as acrylonitrile-butadiene-styrene (ABS), the effect from the loading frequency is significant, as documented in [51]. The aforementioned study also examined the frequency-dependency of polyethylene (PE). The results are shown in fig. 4.14.

A special case of time-dependent fatigue and fracture parameters in Polyvinylchlorid (PVC)

As shown in fig. 4.14, the fatigue life occasionally depends on the speed of the applied load oscillation. Normally, higher frequency reduces the fatigue resistance of polymer materials. In the mentioned case, the load frequency introduces a change in the fatigue properties, but in some polymers, other time-dependent factors also exist that change the fatigue properties. An example of such time dependency exists in polymer materials such as Polyvinylchlorid (PVC). In this particular material, it has been observed that brittle fracture failure might occur after long-term use. fig. 4.15 shows a fracture failure in a PVC pipe where the material properties have changed due to time-dependent material changes.

Notice the nature of fracture in fig. 4.15. The fracture continues along the

5. Fatigue in polymers and composites

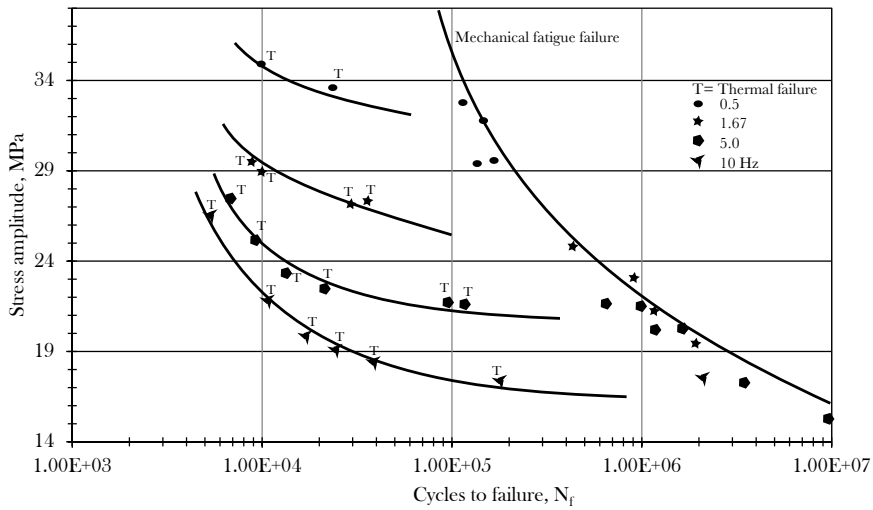


Fig. 4.14: Thermal fatigue failure and mechanical fatigue failure during reversed load cycling of acetal. Source [51].



Fig. 4.15: Failure of a $\varnothing 400$ mm PVC pipe in a water distribution system under long-terms loading by water pressure.

pipe until the crack reaches the coupler (rubber ring joints) to the next pipe section. This failure occurred even though the pipe experienced only small load variations, but under long-term use, the fracture toughness decreased to a critical size, hence yielding a very brittle material behavior. When the material becomes brittle, the critical crack size becomes smaller, thus an otherwise insignificant macro-crack can suddenly become critical. In the present case, the failure was produced by several contributory causes, for instance, the soil settlement. This settlement contains pebbles, and when these get into contact with the outer wall of the pipe, local areas with increased stress

levels arise. The change in fracture toughness occurs due to mechanical and chemical degradation. It is well known and reported all over the world that a degradation process takes place in PVC material, in particular, when this material is used in water distribution systems [12]. In [4], it is reported that the fracture toughness of the PVC decreased from a level of $4.7 \text{ MPa}\sqrt{m}$ to $2.0 \text{ MPa}\sqrt{m}$ over a two years period. Today, pipes are typically either produced by use of other materials or by use of PVC with additives to reduce the brittleness in long-terms use.

Chapter 5

Fatigue in steel and welds

Normally, materials such as steel and aluminum are used to construct mechanical parts and structures, and, often, these are assembled or partially assembled by a joining technique such as welding. Therefore, the welding process is essential to fatigue life. Generally, the welding process deteriorates the fatigue life, but the impact of the joining process and appurtenant parameters can vary. Thus, the joining configuration and welding method need adjustment, in reality, to achieve a satisfying fatigue life. First of all, one needs to understand the nature of the material. For example, steel and aluminum have many similarities in relation to fatigue life, but there are also some important differences. The main difference is that steel, unlike aluminum, has a distinct endurance limit, as seen in fig. 5.1. Such a limit also exists in steel when welds are introduced, even though a relocation of the point occurs.

The relocation of the endurance limit occurs because welding introduces residual stresses, thereby changing the local stress ratio. However, this endurance limit exists only in noncorrosive environments.

1 Impact from welds on steel structures

Manufacturing and assembly of steel structures are often conducted by use of welding. The majority of steel structures contain welds that are applied in the assembly and connection of constituent parts. Welding is a work process which is indispensable for building many modern structures such as wind turbine towers, ships and offshore drilling rigs, and its quality and reliability are important for the fatigue life of any steel structures. Since the introduction of modern joint techniques, e.g. electric arc welding, engineers have realized that welding significantly damages the welded material. Such damage influences some of the material properties, e.g., fracture toughness and

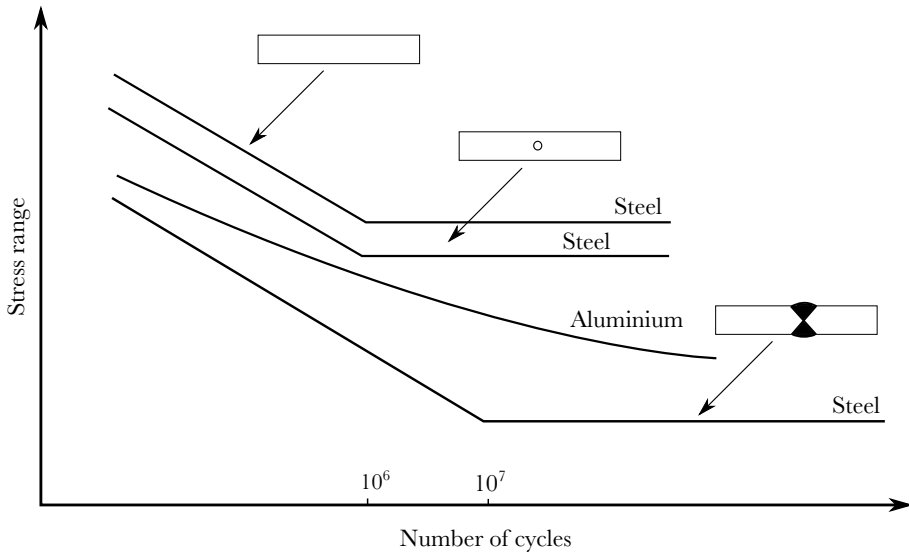


Fig. 5.1: S-N diagram showing the fatigue behavior difference between steel and aluminum. The two lowermost steel curves illustrate the effects of adding a hole and a weld.

yield strength. There are two essential factors affecting fatigue properties:

- Metallurgical transformations due to the contained carbon and hydrogen
- Geometry-related factors such as defects and imperfections

The first-mentioned effect is introduced by a reaction in the steel material when it is heated and cooled in the welding process. In the second effect, the welding process leaves geometric variations, in the form of welding toes and roots.

2 Welding influence on the metallurgy in steel

Changing of the metallurgy may cause extraordinarily high rates of impact on the fatigue resistance in the steel. For example, the Liberty ships suffered from fracture damage because of metallurgical transformations [75]. In that case, changes in the material were activated by the welding process and temperature variations. The impact on the material changed the transition temperature, and the welded zone became brittle, particularly when the ships operated in cold weather, hence leading to a sudden failure. However, today, knowledge of the consequences of welding for metallurgical composition has improved. Thus, ordinary structural steel has improved; examples include

2. Welding influence on the metallurgy in steel

S235 and S355, which have a chemical composition that is more weldable than the chemical composition of the steel used for the Liberty ships. Therefore, welding in the two aforementioned steel types is uncomplicated, and the impact of welding on the mechanical properties is significantly reduced. That said, the welding process still poses risks for metallurgical transformation, in particular in materials with a high carbon content or a special composition, such as steel with high-temperature resistance, X20CrMoV12.1, or stainless steel.

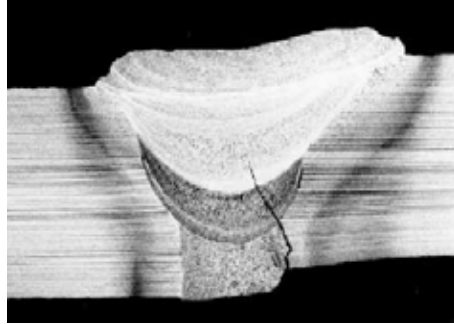


Fig. 5.2: Typical example of root HAZ hydrogen crack extending into the weld metal "Reproduced Courtesy of TWI Ltd" [63].

The heat input is the main contributor to transformation in the welding of steel components. The zone that is affected by the heat in the welding process is designated as the heat-affected zone (HAZ). In this zone, two phenomena, in the form of grain growth and hydrogen cracks, often occur. fig. 5.2 shows a HAZ from a butt weld.

2.1 Grain growth introduced by welding

The fatigue property is crucially affected by grain growth and therefore this growth should generally be avoided [56]. The amount of grain growth depends on the temperature and time in such a way that extensive heating over a certain period of time of the material increases the risk of grain growth. fig. 5.3 shows a welding with distinct grain growth and very large grains near the welds.

Further observation shows that the orientation of the grains is affected by the direction of the heat flow [10]. This affects the properties of the steel and leads to sensitivity in proportion to fatigue damage and changes the fatigue resistance.

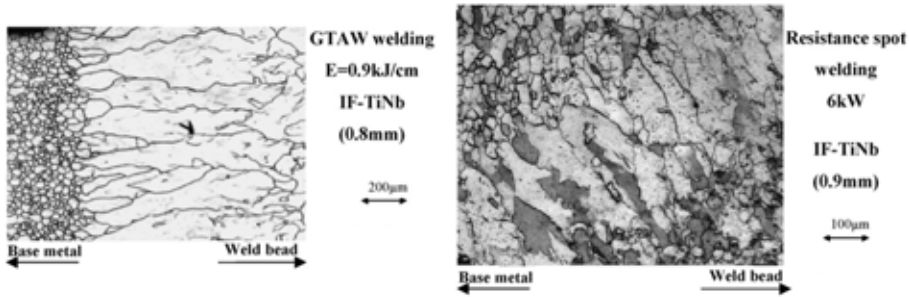


Fig. 5.3: Microstructure of an IF-Ti-Nb welded joint showing excessive grain growth zone. Got permission [6]

2.2 Hydrogen cracks introduced by welds

It is well known that welding may introduce dissolution of hydrogen into the welded material. The level of dissolved hydrogen is dominated by factors such as the welding procedure, steel type and the surrounding environment. If a significant amount of hydrogen is absorbed into the welds, the mechanical properties are changed [33]. Typically, the welded material becomes brittle when the weld contains hydrogen; a transformation known as hydrogen embrittlement [92]. As shown in fig. 5.2, this embrittlement of the material can cause cracking in the HAZ even without any loading. The occurrence of hydrogen embrittlement can be reduced by correctly managing the welding parameters and the cooling profile. Further, the hydrogen level can be reduced by heating the steel, hereby enabling precipitation of hydrogen to the air.

As mentioned previously, the environment is also important for the risk of hydrogen embrittlement. In particular, the risk for cracking of the welding increases if the material is in contact with high concentrations of hydrogen. Many failures due to high concentration of hydrogen have been reported in the oil and refining industries [92]. Accordingly, it is not recommended that these industries use a steel composition that has a tendency to absorb hydrogen. There are more suitable types of stainless steel, e.g. austenitic stainless steel.

As described in [48], the melted zone cools rapidly when using laser welding, hence yielding the potential risk for accumulation of hydrogen into the zone. However, in the aforementioned study, laser welding of austenitic stainless steel (AISI 304) was conducted, thus hydrogen embrittlement was avoided. In this way, it was proven that the combination of laser welding and austenitic stainless steel can be feasible, especially in the oil and refining industries.

3 Imperfection introduced by the welding process

An assembly process such as welding normally connects materials by butt or fillet welds. The assembling technique affects the local stress distribution and therefore also the fatigue life. In proportion to the effect from the welding, two factors are obvious. The first one is the stress concentration factor due to the transition of the loads from one part to another. The second is the creation of a non-uniform surface of the welds and also a profile that includes a welding toe. These factors are, more or less, controlled by the welding process. However, no matter how well-controlled the welding is carried out, a stress concentration factor, a non-uniform surface and a welding profile will always be generated, since the welding requires that the materials are melted together.

fig. 5.4 shows a one- and two-side welding and points out the welding toe. Additionally, D and F1 marks are provided; marks that indicate which S-N curve from fig. 4.9 is recommended for estimation of the fatigue life. Notice that the stress concentration factor in these two cases are limited due to the joint configuration. Nevertheless, by applying the weld from one side, a significant change occurs in the expected fatigue life due to lack of control in the welding process.

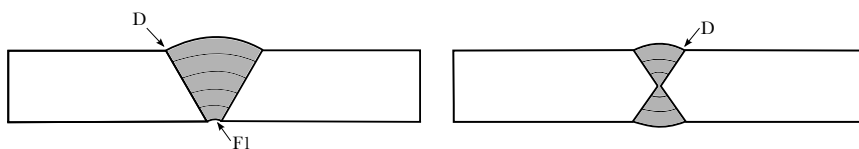


Fig. 5.4: Butt weld in a one- and two-side configuration.

fig. 5.5 illustrates the welding profile for a T-joint with, respectively, a butt weld and a fillet weld. In addition to the welding toe-induced reduction of the fatigue life, a root failure may also be introduced in such configuration. Generally, other local errors and imperfections may also be introduced when applying a welding. Since most weldings are carried out in an open process, inclusion of slag or foreign objects might be melted into the joint. Such foreign objects will result in a significant reduction of the fatigue life.

As described in chapter 2, local micro-errors reduce the strength significantly. Therefore, the characteristic strength and fatigue properties of the joint are also affected by the errors and imperfections in the weld. Often, these welding-induced imperfections can reach a size of 0.1-2 mm, which is larger than the local micro-errors discussed in chapter 2.

The fatigue properties are highly affected by the quality of the welding. S-N curves from norms, e.g. DNV-RP-C203, are based on a certain level of geometric variation in order to make them applicable under most condi-

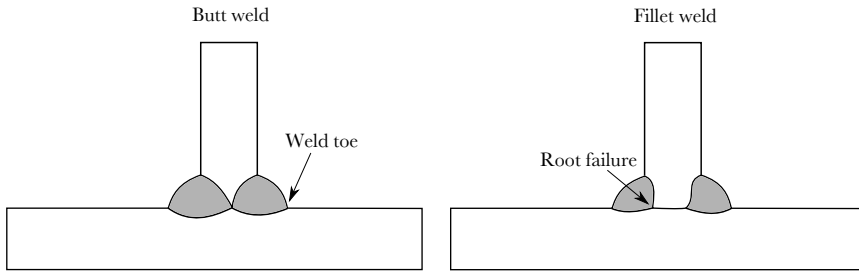


Fig. 5.5: Illustration of a fillet weld and a butt weld in a T-joint configuration.

tions. In this way, there is a recommendation for the production and welding procedure, namely DNV-OS-C401. If the welding component contains, for example, a large welding toe, it will be necessary to compensate for this in the fatigue estimation. Such compensation can be implemented by using FEA and the Hot Spot method.

3.1 Imperfection in laser welded joints of AISI 304

An example of a welding performed with a low quality is shown in [48]. Here, plates of stainless steel AISI 304 are laser-welded into a T-joint configuration. In the present case, several errors are introduced, which diverge from good practice of welding. For example, there is a deviation in the alignment of the plates, in the position of the laser, and in the distance between the two plates. These errors enhance other deviations, for instance a lack of material, and in general this cumulative effect results in a weld that contains a high amount of errors. fig. 5.6 shows a cross-sectional view of the laser welding in question, where some of the errors are visible (notice the flaws at the corners).

Even if a welding has a limited quality, it performs well in proportion to fatigue resistance. The explanation given in [48] is that a redistribution of the stress field arises; a redistribution which is beneficial for the characteristic fatigue strength. Another factor, namely the plate thickness, may also reduce the impact a potentially poor welding.

4 Improvement of the fatigue property in case of imperfections

In reality, it is unavoidable that some errors and geometrical variations will be developed when applying a welding process. Since these errors are unwanted and have an impact on the fatigue life, it is desirable to minimize the quantity. A reduction of errors may be achieved by conducting the welding with the highest possible quality. However, a high welding quality, of

4. Improvement of the fatigue property in case of imperfections



Fig. 5.6: Laser welding of AISI 304 in a T-joint configuration.

course, increases the price of the process. And still, a high-quality welding will contain elements that generally reduce the fatigue life, e.g., a welding toe always arises by welding. Therefore, it is often feasible to apply finishing of the welding to improve the fatigue life.

Normally, a well-performed welding has a shape that is slightly convex or concave, see fig. 5.7. Such welding profile will be acceptable when using norms as DNV-RP-C203 for the fatigue estimation. A convex shape of the welding will improve the fatigue resistance because of the appertaining reduction of the local stress concentration factor.

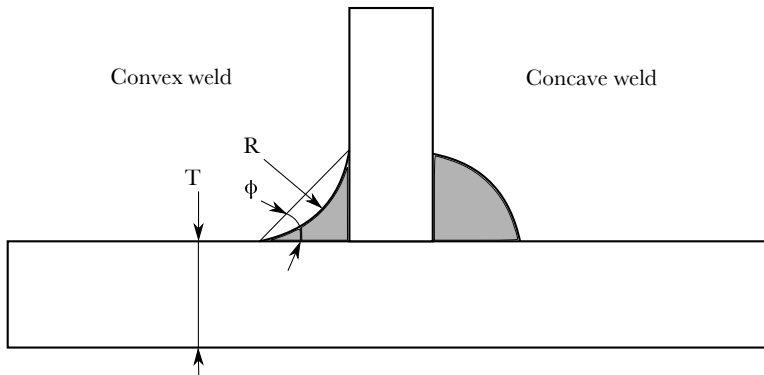


Fig. 5.7: Illustration of the shape of a welding profile, i.e. convex or concave.

Further improvement of the fatigue life can be obtained by using some of the following methods:

- Weld grinding
- TIG dressing
- Hammer peening

When using the weld grinding method to improve the fatigue life, there are two procedures to follow; grinding of the welding profile or grinding that also removes the welding toe. The effect of grinding the welding can be evidenced by computing the reduced stresses trough

$$\sigma_{\text{Local reduced}} = \sigma_{\text{Membrane}}\alpha + \sigma_{\text{Bending}}\beta \quad (5.1)$$

where σ_{Membrane} is the membrane stress, σ_{Bending} is the bending stress, and α and β are derived from eq. (5.2) and eq. (5.3), respectively.

$$\alpha = 0.47 + 0.17(\tan \phi)^{0.25}(T_w/R)^{0.5}. \quad (5.2)$$

$$\beta = 0.60 + 0.13(\tan \phi)^{0.25}(T_w/R)^{0.5}. \quad (5.3)$$

In eqs. (5.2) and (5.3), T_w is the thickness of the plate and ϕ is the angle of the welding profile, see fig. 5.7. Notice that the maximum improvement factor from grinding only must not exceed 2, cf. DNV-RP-C203.

Instead of grinding the welding profile, the fatigue life may be improved by grinding the toe of the welding and hereby remove the geometry that reduces the fatigue life. In this approach, the recommendation is to use a diameter of 12 mm and leave a surface that is smooth, i.e. $R_a = 3.2$ or better, cf. DNV-RP-C203. Conducting the grinding is relatively simple, for instance by use of tools such as a coarse grit flapper disk. Notice that the grinding depth should not exceed 2 mm or 7 % of the plate thickness, cf. DNV-RP-C203.

Another method to improve the fatigue life is TIG dressing. This method removes the weld toe flaws by re-melting the toe [32] and is as such one of the most simple ways to improve the fatigue life. However, it is generally not as efficient as grinding, and, also, the re-melting of the welding toe can change the level of residual stresses [93].

Lastly, the fatigue life can also be improved by using hammer peening and hereby changing the mean stress level at the surface of the welding. Hence introducing compression stresses to the surface of the welding, resulting in a reduced tendency for surface cracks to develop.

With regards to changes in the fatigue resistance, DNV-RP-C203 suggests that the increase in fatigue life due to implementation of TIG dressing or hammer peening will be in the interval of $0.01f_y$ and four times the original fatigue life. For more information, see [19], Tb. 7-1.

5 Residual stresses in welds

It is common that steel components, e.g. plates and beams, contain internal stresses. Often, these stresses are denominated as residual stresses and are widely investigated with regards to their influence on the fatigue life. The level of these stresses can vary from a few MPa to stresses close to the yielding level of the material, depending on which process the component has been subjected to. Below, some of the processes that have an impact on the residual stress level are listed:

- Forming by cold or hot rolling
- Welding

Generally, steel beams contain residual stresses when there are manufactured to the final size. Therefore, steel bars and beams contain residual stresses when they are delivered to further processing. The source for these residual stresses is the shaping process, which typically is carried out by cold or hot rolling. This introduces a high level of deformation and, thus, local stress variations. However, investigations have documented that the residual stresses in a cold-formed section is different from those in a hot-formed one [90]. Furthermore, it has been well-documented that there is a presence of tensile stresses in both longitudinal and transverse direction in cold-rolled steels [30]. As a consequence, the load capacity is adversely affected [78].

The level of residual stresses introduced by cold and hot rolling is low compared to the stress level introduced by welding. The residual stresses in a welded joint can reach a size corresponding to the yield strength of the material. The source that causes these high residual stresses is the heating from the welding, which introduces an alternation in the state of the material; solid, liquid and finally solid.

Intensive heating also causes local material expansion that introduces a high rate of stress. Further, when the heat source moves, hereby adding a new constraint in the form of a butt or filled weld, and the joint cools, local stress variations are introduced. However, since the residual stresses depend on the joint and cooling process, these parameters are essential for the location of the stresses. Therefore, the level of residual stresses can be reduced by, e.g., preheating the joint before welding [1,83]. Additionally, simple welding procedures such as backstep welding may dramatically change the level of residual stresses.

An example of the residual stress distribution in a welded joint is shown in fig. 5.8, where two plates are connected through a butt welding. In this case, the welding is accomplished in a continuous process from one side to the other. If this welding was carried out in steps from both sides, the stress

profile would change dramatically. As shown in [27], the backstep welding may be the optimal welding approach in some cases, but in other cases, the effect on the residual stress level vanishes. Therefore, it is impossible to establish a general rule regarding the welding procedure, although some best-practice specifications exist for certain standard joints. Additionally, FE software can simulate the residual stress level in a specific welding configuration, see e.g. [27,82].

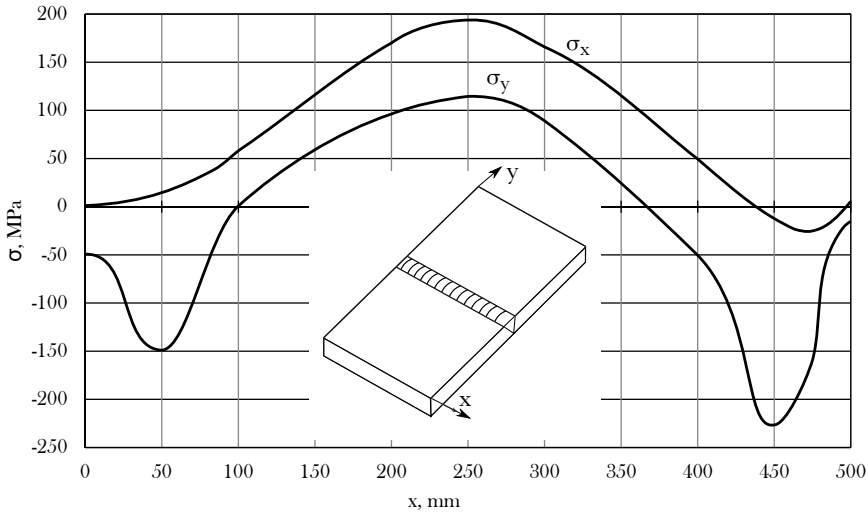


Fig. 5.8: Stress level along a butt weld. Source [44].

Another factor that influences the fatigue resistance of a joint is the welding technology. Methods such as MIG/MAG, TIG and electric welding have been used in decades, hence the fatigue resistance of joints based on these welding methods have been investigated intensively. However, further studies and investigations are requested since new welding methods and practices have been introduced.

Laser welding is becoming increasingly popular as the laser technology is now more commonly used. Up until now, the equipment and operational costs associated with laser welding have been extraordinary high, and therefore the method has previously only been applied in a limited number of cases, e.g., high-end jobs in the aerospace industry. Today, it is more common to apply the laser welding method, for example in joining of stainless steel, see e.g. [48,49].

The laser welding method applies the heat input more intensive compared to the traditional methods, resulting in another distribution of the heat and cooling profile in the joint. Thus, the temperature gradient is different

6. Residual stresses and their impact on the S-N curve

compared with those obtained by use of the traditional welding methods. Since higher temperature gradients occur in the welding process, changes in the magnitude of the residual stresses are generated; yielding an impact on the fatigue properties. This cooling rate and concentration of the laser power have been reported to have a significant influence on the fatigue properties [87].

The understanding of the concept of effect from the residual stresses on the fatigue properties is essential when designing components that are subjected to a fatigue load. Yet, as mentioned previously, the residual stress level is difficult to predict, and therefore attention is not always paid to this when estimating the fatigue life.

6 Residual stresses and their impact on the S-N curve

Residual stresses in a specimen will change the stress ratio locally. Thus, some of the material in a welded joint will experience a stress ratio of $R > 0$, i.e. tension-tension, meaning that the fatigue life is lowered in such cases. This implies that welded and non-welded specimens, loaded with the same fatigue load, have different fatigue properties. This is evidenced in fig. 5.9.

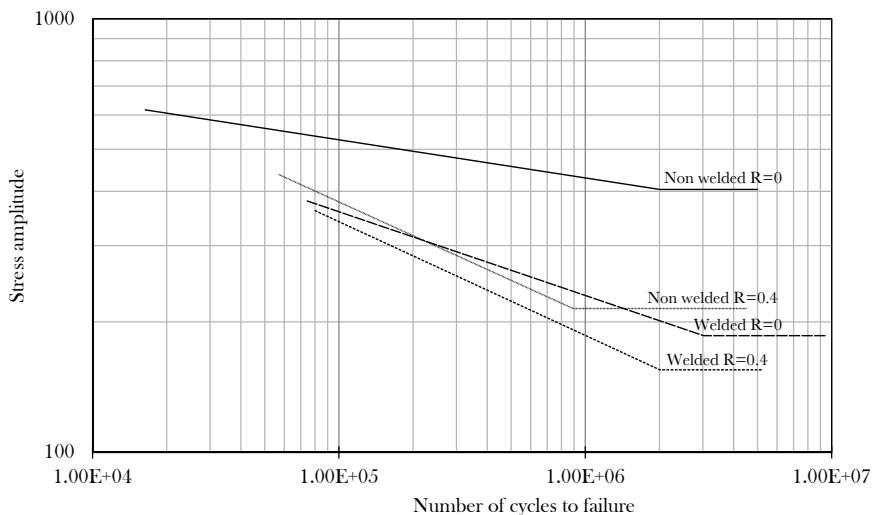


Fig. 5.9: S-N curves for welded and non-welded specimens. H13 steel: $R = 0$ and $R = 0.4$, Source [16].

The loading stress ratio has, as seen in fig. 5.9, more effect on a non-

welded specimen than a welded one. This behavior is related to the welding process as this introduces both local tension-tension stress conditions and local compression-compression stress conditions. Normally, the residual stresses from the welding process are included indirectly in the fatigue estimation by use of norms, such as EUROCODE 3 and DNV-RP-C203, because they are based on experimental results where residual stresses are contained. If the residual stress level is requested, the hole-drilling method and/or X-ray diffraction (XRD) produce reliable results in measuring the level of residual stresses.

Chapter 6

Determination of structural capacity by non-linear FEA methods

1 Introduction to fatigue estimation by FEA

For decades, the load capacity of structures has been studied extensively to avoid failure by approving the structural dependability. In specific, fatigue failure has been avoided by using such a high rate of safety margin that introduction of estimation errors has been acceptable, of course to a certain level. This is also the case when estimating the fatigue damage by use of the S-N and ϵ -N methods. Since the nature of fatigue is difficult to understand, it is crucial that a high safety margin is implemented in order to provide the necessary structural safety. Due to their high rate of safety, the two aforementioned methods have been widely accepted as the method for calculating the fatigue life in cases of low cycle fatigue. However, this high rate of safety results in a conservative estimate, which, again, leads to use of an unnecessary amount of material. Therefore, the need for a method that provides a better foundation for the fatigue estimation is evident. Such method can be obtained by applying FEA in which plastic strains can be analyzed.

1.1 Local plastic strain and nonlinear material

In a structure, local plastic strain may occur under extreme circumstances such as overloading. Especially the areas of stress concentrations are exposed to plastic strains, and since almost all structures contain these areas, in the form of geometric changes, the risk of inducing local plastic strain

is present [36]. The actual level of plastic strain is complicated to determine analytically since the material stiffness changes, hereby composing non-linearities. Additionally, it is troublesome to determine the level of plastic strain through experiments, i.a., due to scaling effects. This clearly emphasizes the applicability of FEA in which these non-linearities can be treated, albeit with a comprehensive amount of computational time.

When examining non-linear material behavior by use of FEA, the cyclic stress-strain curve of the material must be incorporated. This curve can be described by the Ramberg-Osgood relation [64,73]

$$\epsilon = \frac{\sigma}{E} + \left(\frac{\sigma}{K'} \right)^{n'/10} \quad (6.1)$$

where K and n are material-dependent constants. The Ramberg-Osgood relation fits the behavior of materials such as steel [9] and is therefore often employed in FEA involving such materials to describe the cyclic stress-strain curve. However, the Ramberg-Osgood relation may not validly describe the behavior of materials such as polymers [37].

Regarding the cyclic stress-strain curve it is important to keep in mind that this differs from a curve generated through tension tests. This is illustrated in fig. 6.1 where the two different curves are illustrated. Evidently, the stress-strain curve from the tension lies above the cyclic stress-strain curve.

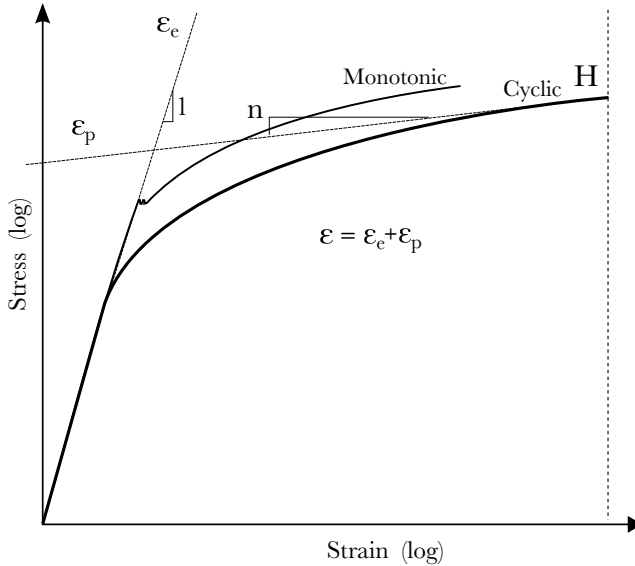


Fig. 6.1: Stress-strain curves obtained from monotonic tension testing and cyclic testing.

1. Introduction to fatigue estimation by FEA

1.2 Fatigue damage generated by plastic strain

When introducing fluctuating strain into a component, the risk of damage initiation arises. The criticality of this damage can be estimated by means of the S-N method, as described in chapter 4. However, when plastic strain is introduced in the total strain amplitude, the S-N method does not provide the necessary data since it does not account for plasticity. Therefore, a method that takes this into account must be employed. Such method can be found in DNV-RP-C208 where the material and fatigue properties are separated into welded joints and base material. These properties are described through

$$\frac{\Delta\epsilon_{hs}}{2} = \frac{\sigma'_f}{E}(2N)^{-0.1} + \epsilon'_f(2N)^{-0.5} \quad (6.2)$$

and

$$\frac{\Delta\epsilon_{hs}}{2} = \frac{\sigma'_f}{E}(2N)^{-0.1} + \epsilon'_f(2N)^{-0.43} \quad (6.3)$$

for the welded joints and the base material, respectively. In eqs. (6.2) and (6.3), $\Delta\epsilon_{hs}$ is the allowed strain amplitude to a number of cycles, N , while σ'_f and ϵ'_f are fatigue parameters relating to stresses and strains.

By use of this method, the two strain components, namely the elastic and plastic parts, are treated separately. The estimation of the elastic strain can be conducted relatively simple, whereas the estimation of the plastic strain level is rather complicated since the material stiffness changes with the amount of straining. Hence, it is necessary to supplement with a method that allows stiffness to change by a number of increments; a feature which can be fulfilled with high accuracy by FEA, also in complex design cases.

1.3 Details of estimation by DNV-RP-C208

In June 2013, DNV released the document "Determination of Structural Capacity by Non-linear FE analysis Methods", also known as the DNV-RP-C208. This recommendation is in particular based on limit state calculations, i.e. ultimate limit states and accidental limit states. Contrary to fatigue estimation by DNV-RP-C203, the DNV-RP-C208 centers around the levels of load that introduce plasticity, for instance, ultimate limit states. However, estimation of the maximum load carrying resistance not only depends on the ability to endure plastic strain, but also the ability to carry the buckling load. Description of the calculation of such buckling load is also included in DNV-RP-C208, but in the present thesis, the focus is on the damage induced by plastic strain. To clarify the application of the DNV-RP-C208, two cases are examined in the

following sections. The first case is an assembly detail of tubular joints and the second is a plate with a hole subjected to oscillating displacement.

2 Low cycle fatigue analysis of tubular joint subjected to out-of-plane loading

Jacket structures are used widely in the offshore industry and are, as such, subjected directly to wave and wind loads. Therefore, it is of great importance to determine the load capacity of jacket structures. Normally, such calculations only involve elastic strain as the loads do not introduce plastic strain. However, when a ship hits a structure, deliberately or accidental, or if extreme sea state occurs, the loading can become so high that plastic strain arises. Needless to say, it is necessary to include the total straining in the estimation of the fatigue life of the structures. Such overloading scenario is treated in this chapter where the low cycle fatigue life of a simple structure is analyzed on the basis of the recommendation from DNV-RP-C208. The structure consists of a brace and a chord, imitating a joint in a jacket structure.

2.1 The setup of the brace and chord model

The brace and chord are connected perpendicularly to each other by means of a welding. In fig. 6.2, a sketch of the connection is shown with the appertaining dimensions.

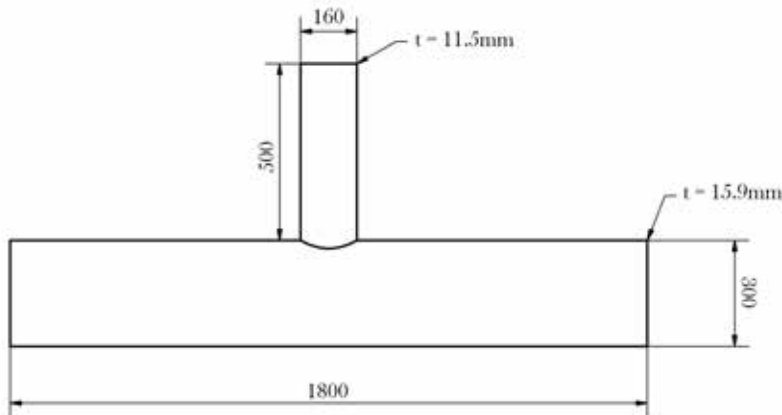


Fig. 6.2: Brace and chord-joint with appertaining dimensions.

The model is analyzed in ANSYS Workbench 15 where the module "ANSYS DesignModeler" is used to build the geometry. It is noticed that a model

2. Low cycle fatigue analysis of tubular joint subjected to out-of-plane loading

of this size can be analyzed on an ordinary computer, but in the case of a larger model, it will be necessary to include an HPC to achieve acceptable computational time.

In order to simulate the behavior of a real jacket structure, a proper setup for the submodel of the jacket structure must be established. In the present case, this is done by constraining both endpoints with the condition that no translational movement occurs while local rotation about the centerline is allowed. This constraining may affect the result negatively by restricting against local out-of-plane bending. In such case, an undesirable overestimation, with potentially catastrophic consequences, occurs. Therefore, the cut-out of the global system is made with appropriate distance to the joint, hence allowing local buckling and stability problems despite the inordinate constraining. The final evaluation of the validity of this approach is done on the basis of engineering judgment.

Boundary conditions

In the present example, the cut-out distance is around three times the pipe diameter, when measured from the center of the joint. Regarding the additional boundary conditions, it is noticed that a load is added in the out-of-plane direction on the top of the brace, as shown in Fig. 6.3. This load is sinusoidal with an amplitude of 60 kN which ensures introduction of plastic strain. Due to this, the stability of the hysteresis loop has been examined, and here it has been found that one and a half load cycle is sufficient for reaching stability. It is noticed that in other cases it may be necessary to run more cycles to get the stable hysteresis loop.

Model discretization

Since both material and geometrical non-linearities are simulated, the computations are time-consuming. Therefore, it is particularly important to discretize the model by use of a well-distributed mesh without using unnecessary elements. According to the recommendations in DNV-RP-C208, it is advised to use higher-order elements, and therefore 8-noded, second-order shell elements, "SHELL281", are employed.

Regarding Hot Spot analysis, the DNV-RP-C203 dictates that the two hot spot points needed for stress extrapolation are located at distances

$$a = 0.2\sqrt{rt} \quad (6.4)$$

and

$$b = \frac{\pi R}{36} \quad (6.5)$$

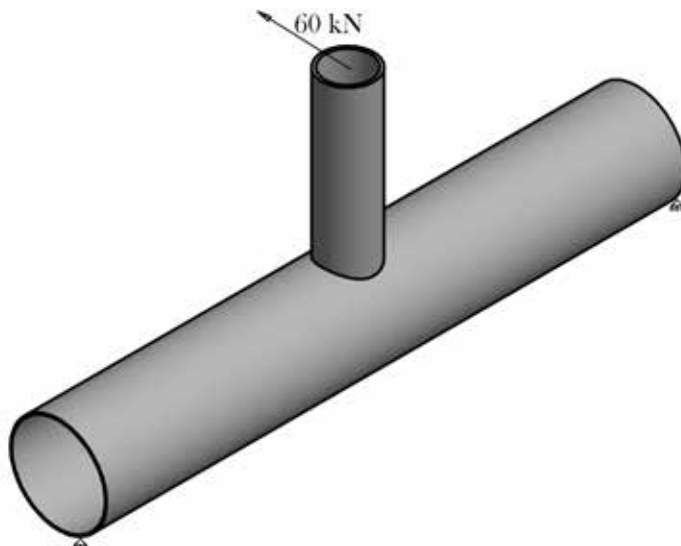


Fig. 6.3: Model of brace and chord-joint with indication of boundary conditions.

from the actual hot spot, with r , R , and t being the brace radius, chord radius, and material thickness, respectively.

When using FEA to determine the stress level at the hot spots, the stress result from the midpoint of the element is used. In the present example, the first element size is 12.2 mm and the second 0.9 mm, thus the second ring of elements surrounding the interface is very small, see fig. 6.4, and does not fulfill the requirement of a well-distributed mesh size. Use of such inapplicable element ratio will not be accepted in the quality control of the FE solution. Instead, it is necessary to diverge from the commonly acceptable principles and use the end node of the element for Hot Spot analysis. In this case, the first element size is then 6.1 mm and the second is 7 mm, which is an allowable ratio of the element distribution. In order to obtain a mesh composed of rectangular elements, which generally yield the best results, each element ring surrounding the interface is divided into 62 elements. In ANSYS Workbench, these divisions of elements are implemented by using the command "Inflation" in the setup, with the settings "First layer thickness = 6.1 mm" and "Growth rate = 1.1475". This yields the local mesh depicted in fig. 6.6.

Setup of the material model

As mentioned previously, local plastic strain occurs in the joint, and therefore both elastic and plastic strain contribute to the final strain amplitude. In the

2. Low cycle fatigue analysis of tubular joint subjected to out-of-plane loading

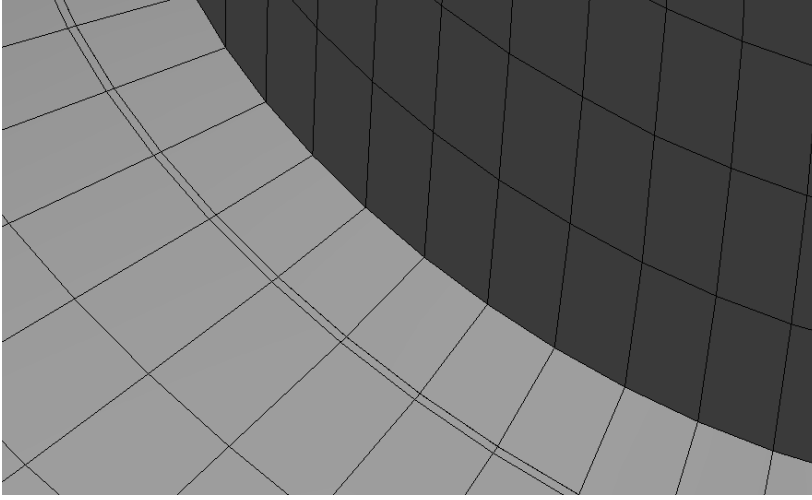


Fig. 6.4: Mesh distribution where the elements in the second ring are very small.

calculation of the low cycle fatigue life, the total cyclic strain from the FEA of the joint is used.

Assuming that the joint is made of construction steel, the utilized material model must facilitate description of the cyclic strain hardening which occurs since construction steel changes stiffness when it is exposed to cyclic and plastic straining. According to eq. (6.1), the Ramberg-Osgood material model facilitates this. In table 6.1, the recommended Ramberg-Osgood parameters are presented.

Table 6.1: Ramberg-Osgood parameters for the FEA of braces and chords.

	K' [MPa]	n'
Chord	731.7	0.096
Brace	699.5	0.108

In the material model, a hardening rule must be chosen. Here, the kinematic hardening rule is applied, such the Bauschinger effect is included. It should be noticed that kinematic hardening is useful when analyzing steel materials, whereas isotropic hardening is applicable for polymers.

The modulus of elasticity for the utilized steel is 207 GPa. In Fig. 6.5, the cyclic stress-strain curves for the brace, chord and the S355 material are presented. Evidently, the brace and chord have higher elastic capacity than S355, even though they might be constructed in S355. Furthermore, the materials also have a significant plastic strain capacity according to the criterion in DNV-RP-C208. Here, the maximum principal plastic critical strain level is

at 0.12.

Numerically, the high amount of plastic strain necessitates a considerable number of substeps in order to obtain convergence in the iterative solver. In fact, the analysis is divided into 90 substeps; each in which the stiffness is updated, cf. the nonlinear nature of the analysis.

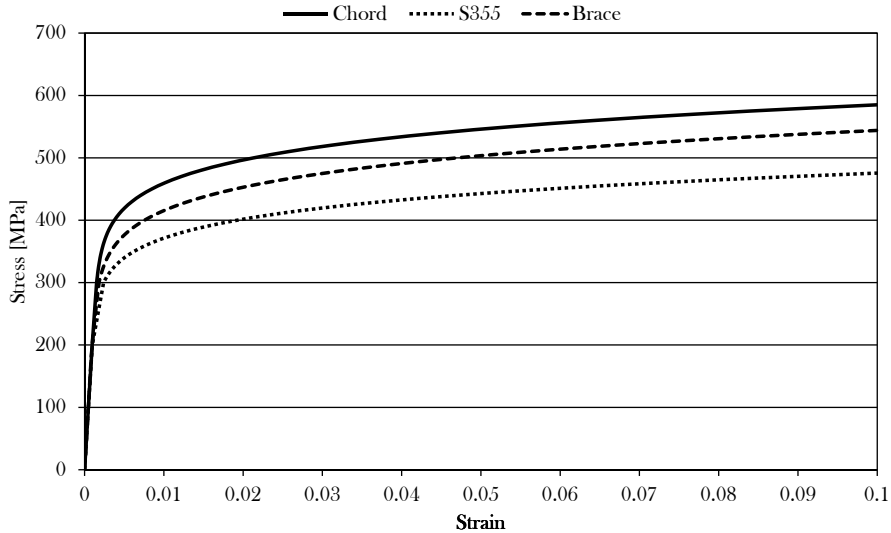


Fig. 6.5: Material behavior for the brace, Chord and S355.

2.2 Strain level obtained by the FE model of the brace and chord model

After completing the FEA, the total strain range can be found from the strain amplitude in the stable hysteresis loop. In other words, by obtaining the stable strain range from the two extrapolation points, the hot spot strain can be found. Fig. 6.6 shows the strain distribution in the joint.

In the present case, the maximum and minimum strain values are found when the load changes from -60 kN to $+60$ kN. As mentioned in Sec. 2.1, the loop already reaches stability in the second load cycle. Hence, by subtracting the minimum strain value found in the second cycle from the maximum counterpart, the strain range is found. The results are presented in Table 6.2.

After determining the strain range from the two hot spot points, the cal-

2. Low cycle fatigue analysis of tubular joint subjected to out-of-plane loading

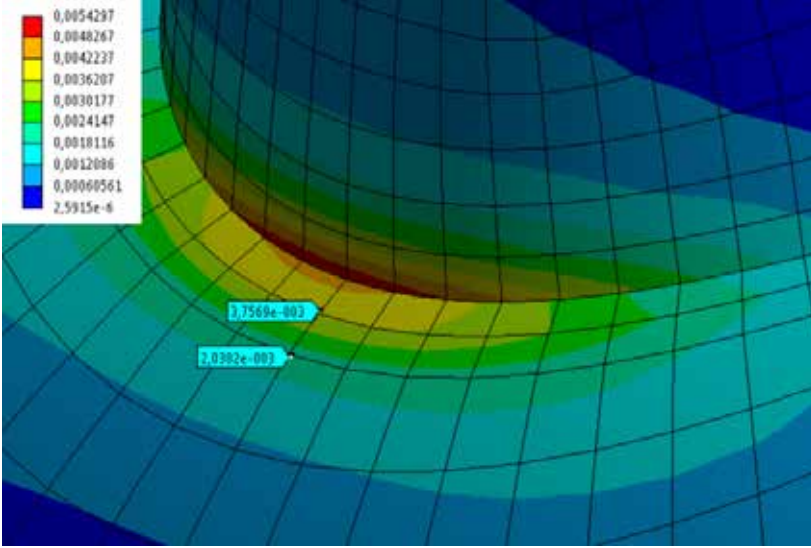


Fig. 6.6: Maximum principal strain in the chord.

culuation of the hot spot strain ranges can be carried out by use of

$$\Delta\epsilon_{HotSpot} = \Delta\epsilon_a - \left(\frac{a}{b-a} \right) (\Delta\epsilon_b - \Delta\epsilon_a) = 0.0106, \quad (6.6)$$

where a and b are the distances to the hot spot points while $\Delta\epsilon_a$ and $\Delta\epsilon_b$ are the appurtenant strain ranges.

When the hot spot strain ranges are found by Eq. (6.6), the fatigue life can be found through Eq. (6.2) such

$$\frac{0.0106}{2} = \frac{731.7}{210000} (2N)^{-0.1} + 0.096(2N)^{-0.5} \Rightarrow N = 1230. \quad (6.7)$$

Evidently, the calculation estimates a fatigue life of the joint corresponding

Table 6.2: Total principle strain levels in the brace and chord connection.

	Minimum strain	Maximum strain
Point a (step 2)	$-3.08 \cdot 10^{-3}$	$3.76 \cdot 10^{-3}$
Point b (step 2)	$-1.50 \cdot 10^{-3}$	$2.03 \cdot 10^{-3}$
Point a (step 3)	$-3.82 \cdot 10^{-3}$	$3.15 \cdot 10^{-3}$
Point b (step 3)	$-2.08 \cdot 10^{-3}$	$1.56 \cdot 10^{-3}$

to 1230 cycles with a fully reversible load. It is important also to investigate the fatigue life of the brace section. However, in the present example this is omitted as the calculations required are identical to the ones presented for the chord section.

3 Low cycle fatigue analysis of other structural details

When introducing fatigue damage by plastic straining, the fatigue estimations by the usual recommendations are inapplicable, for instance, when using DNV-RP-C203. In this recommendation, the restriction is that the maximum stress level must not exceed 80 % of the yielding stress.

Normally, the engineer designs the structural component in such a way that only elastic strain occurs in ordinary load situations. But in case of extraordinary high loads, plastic strains may be introduced, typically near geometric variations. Since plastic strain also causes fatigue damage, it is imperative to identify the amount of damage from the plastic straining. For example, the number of overloading, including plastic straining, cycles is important when estimating the total fatigue life of a structural component. As shown in section 2, the DNV-RP-C208 presents a specific method to calculate the fatigue damage in tubular joints in cases where both elastic and plastic straining occur. The aforementioned recommendation also enables general low cycle fatigue estimations. This is shown in the following example where a plate with a circular hole is exposed to overloading.

3.1 Example: estimation of the low cycle fatigue life for a plate with a circular hole

In the present example, the plate depicted in fig. 6.7 is treated. The plate is subjected to a cyclic displacement with an amplitude of 1.0 mm.

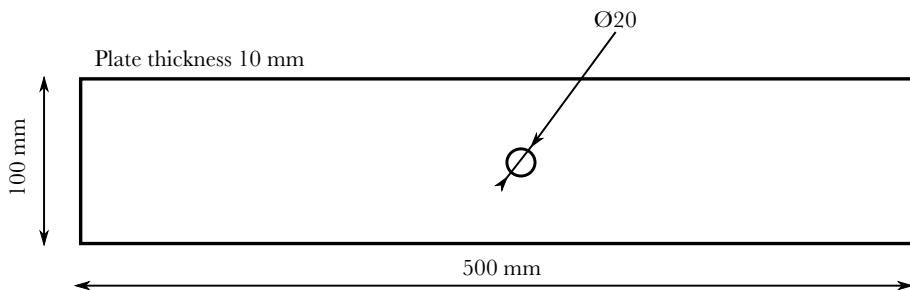


Fig. 6.7: Plate with a hole subjected to cyclic displacement.

3. Low cycle fatigue analysis of other structural details

The model is discretized by use of "SHELL181" elements. The mesh is obtained by slicing up the geometry, yielding the eight lines shown in fig. 6.8. Each of these lines are discretized into 10 elements and assigned a bias factor of 5 to refine the mesh around the hole. Additionally, the hole is divided into 48 elements, also seen in fig. 6.8. This provides the final mesh, consisting of 1080 shell elements, illustrated in fig. 6.9.

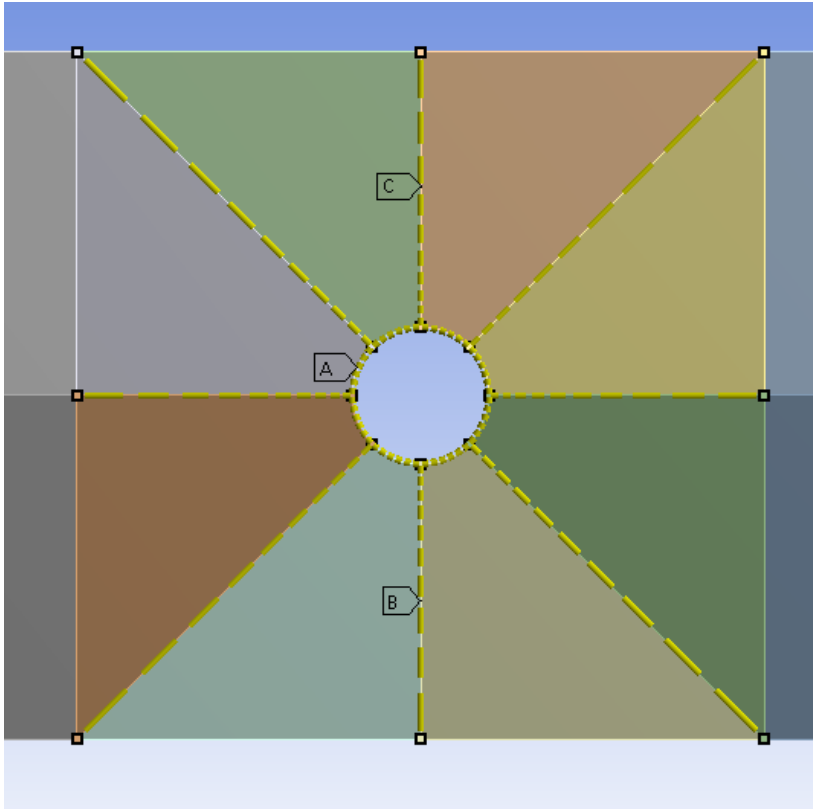


Fig. 6.8: Setting up the discretization of the plate.

As previously described, the model is loaded by cyclic displacement with an amplitude of 1.0 mm. To ensure proper introduction of hardening effects, the plate analysis is carried out for six full load cycles. In fig. 6.10, the plate model is depicted with the existing boundary conditions and displacement, denoted as δ .

The material used in the analysis is steel S355. The cyclic hardening parameters, K' and n' , are set to 600 and 0.1, respectively, and substituted into eq. (6.1).

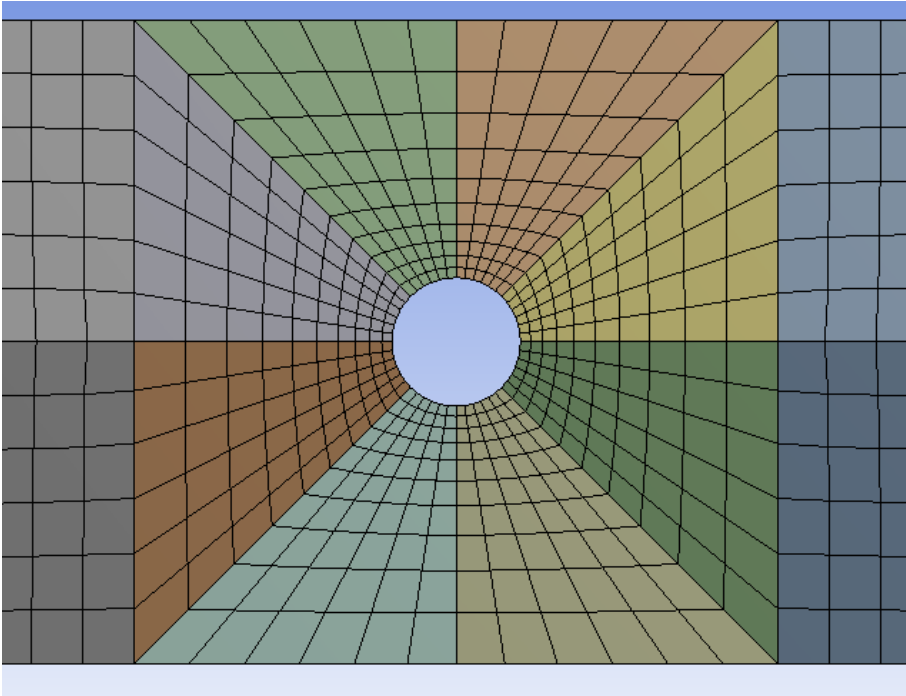


Fig. 6.9: Final mesh of the plate.

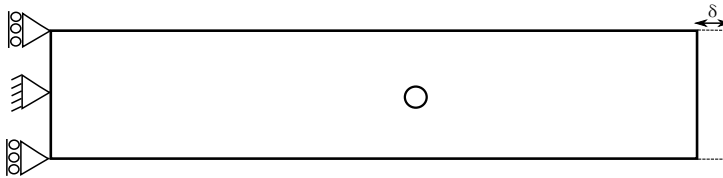


Fig. 6.10: Plate model with boundary conditions and displacement.

The stress results

As expected, the maximum strain level arises in the area around the hole, where plasticity is reached. fig. 6.11 shows the zone where the plastic straining occurs.

Since the configuration is set to displacement mode, redistribution of the stresses is allowed, hereby enabling local compression stresses.

As stated earlier in this example, the plate is analyzed for six full load cycles in order to properly introduce the hardening effects. In particular, these effects are properly introduced when the strain hysteresis loop is stabilized, as seen in fig. 6.12. The first load cycle introduces a high level of strain into

3. Low cycle fatigue analysis of other structural details

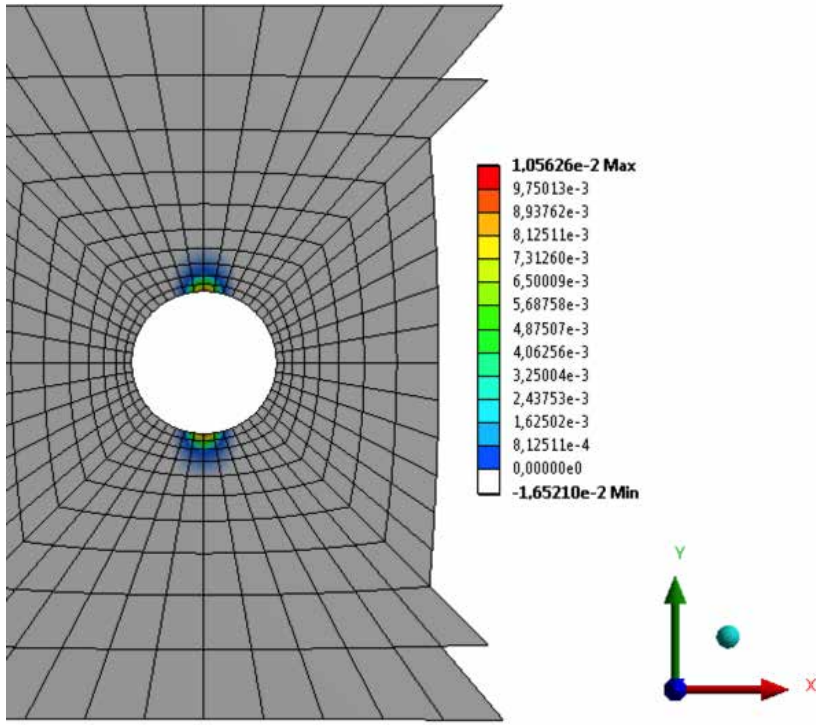


Fig. 6.11: Plot of the total strain variation in the area around the hole.

the material around the hole, and the following load cycles will behave as a hysteresis loop with elastic and some plastic strain. As shown in fig. 6.12, the loop is relatively stable, and therefore it is unnecessary to include further load steps. Hence, the maximum total strain range in this example is $\Delta\epsilon = 0.0105$, and in such case, the low cycle fatigue life is then 85 load cycles. The fatigue life calculation is conducted by use of eq. (6.3).

This example shows a case which is relatively simple in proportion to geometry. Nevertheless, the estimation of the total strain range requires considerable CPU power, hence demonstrating the comprehensive extent of such calculations.

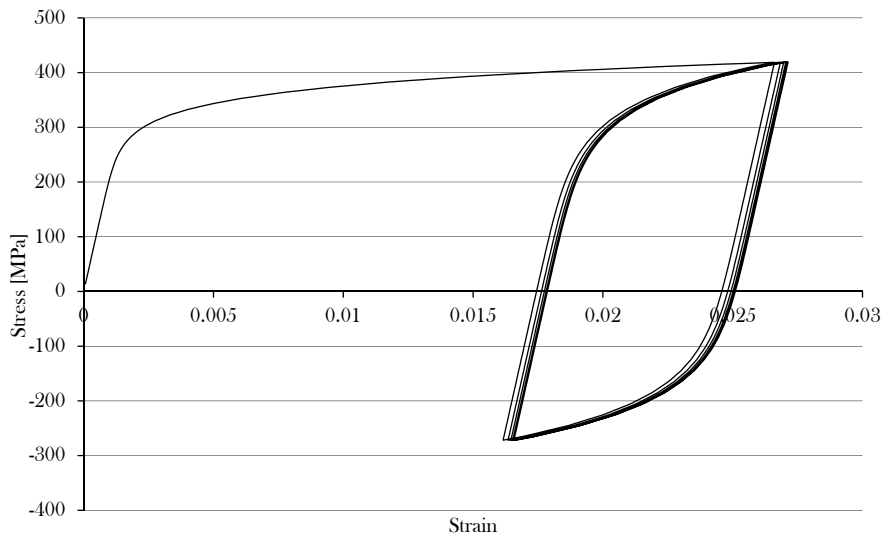


Fig. 6.12: Plot of the stress and strain relation (showing the hysteresis loop).

Chapter 7

Conclusion

This thesis is about fatigue and fracture mechanics with focus on materials such as steel, stainless steel, copper, aluminum and polymers. The thesis presents scientific work with relation to fatigue and fracture, and the theoretical background is presented as assistance for the statements. Generally, the thesis treats four overall subjects, namely 1) fatigue analysis of copper (CuNi10) tubes, 2) fatigue analysis of laser welded T-joints designed in stainless steel (AISI 304), 3) metallurgical investigations of the aforementioned T-joints, and 4) investigations of using coating layer as a patch repairing method for steel and aluminum structures. As an addition, the use of numerical tools, i.e. FEA, to estimate the low cycle fatigue life in accordance with the new recommendation DNV-RP-C208 is treated. The latter has been included since the author of this thesis has been involved in developing the specific DNV recommendation.

Documentation of the fatigue properties is found experimentally for CuNi 10 tubes. Here, the setup is based on the strain variation generated in a ship heat exchanger when the temperature fluctuates. The test results show low spreading of the data, thus a narrow band can represent most of the data points. The experimental testing shows good fatigue resistance of the pipes, and by applying a statistical evaluation, an ϵ - N curve that is usable in design cases is developed. The curve is developed in such a way that an application has high probability for survival based on a specific confidence interval. On the basis of the developed ϵ - N curve, it is concluded that the risk for failure is minimal in the case of fatigue damage generated by thermal strains in a ship engine.

In the study of laser welded T-joints of stainless steel AISI 304, the fatigue properties are found for a thin-walled application. Here, the experimental results are plotted in S-N curves, hence facilitating comparisons with fatigue estimations by recommendations, namely DNV-RP-C203 and EUROCODE 3

EN-1993-1-9. It is found that the fatigue lives estimated by use of recommendations are larger than what was obtained in the experiments. In addition to testing of the AISI 304 T-joints, testing of AISI 304 specimens without welds have been tested to establish a reference for investigation of the impact from the welding.

Investigations of the metallurgical structure and the transformation introduced as a result of the laser welding process have been carried out for the aforementioned T-joints. Such investigations are conducted by use of Lichtenegger and Bloech color etching, ferritescope, XRD and Vickers hardness. The conclusion is that the location of a smaller amount of martensitic phase is observable at the weld, but this low concentration does not significantly affect the crack growth. However, loading of the specimens can generate higher concentration since stress and strain can trigger a transformation in an area that already contains a martensite concentration. In particular, a transformation can be introduced in the welded area since this area contains both residual stresses and stress concentration factors.

Investigations of using a patch repairing method, in the form of a coating layer that applies a closing effect to surface cracks, have demonstrated limited effect on the crack growth. This effect is marginal due to the low elastic strength and modulus of elasticity of the surface layer and the high modulus of elasticity for the repaired materials, namely steel and aluminum. This has been evidenced in a study where a 5 % crack extension has been introduced, and based on this, the fatigue effect of using pure epoxy as surface repairing has been found to be insufficient.

References

- [1] Heshmat A. Aglan, Sudan Ahmed, Kaushal R. Prayakaraao, and Mahmood Fateh. Effect of preheating temperature on the mechanical and fracture properties of welded pearlitic rail steels. *Engineering*, 5:837–843, November 2013.
- [2] J.S. Ahn, P.K. Basu, and K.S. Woo. Analysis of cracked aluminum plates with one-sided patch repair using p-convergent layered model. *Finite Elements in Analysis and Design*, 46:438–448, February 2010.
- [3] V.S Ajay Krishna, G.S. Mahesh, and H.V. Lakshminarayana. Mixed mode fracture of a nuclear reactor steam generator helical coil tube with arbitrarily oriented and located through wall crack. *International Conference on Recent Advances in Engineering Sciences*, 2(1):59–66, September 2014.
- [4] Chalasai Eurtivong Axtell and J. G. Williams. Fracture of pvc pipes. *Journal of the Science Society of Thailand*, 18:53–65, April 1992.
- [5] O. H. Basquin. The exponential law of endurance tests. *ASTM*, Vol. 10(Part 2):P.625, 1910.
- [6] E. Bayraktar, D. Kaplan, L. Devillers, and J.P. Chevalier. Grain growth mechanism during the welding of interstitial free (if) steels. *Journal of Materials Processing Technology*, 189(Issues 1–3):114 – 125, 2007.
- [7] S. M. Beden, S. Abdullah, and A. K. Ariffin. Modeling of fatigue crack growth under constant and variable amplitude loading. *International Journal of Mechanical and Materials Engineering (IJMME)*, 4(2):131–135, 2009.
- [8] M. Benachour and N. Benachour. Effect of mean stress on fatigue crack growth behavior of stainless steel 304l. *World Academy of Science, Engineering and Technology*, 5:984–987, 2011.
- [9] Frøydis Boge, Torgeir K. Helland, and Stig Berge. Low cycle fatigue of t-tubular joints with out-of-plane bending loading. In *ASME 2007*

- 26th International Conference on Offshore Mechanics and Arctic Engineering, volume 4: Materials Technology; Ocean Engineering of ISBN: 0-7918-4270-3, pages 107–115, San Diego, California, USA, June 10–15 2007.
- [10] Zakaria Boumerzoug, Chemseddine Derfouf, and Thierry Baudin. Effect of welding on microstructure and mechanical properties of an industrial low carbon steel. *Engineering*, 2:502–506, 2010.
 - [11] Howard E. Boyer, editor. *Atlas of Fatigue Curves*. Number ISBN-13: 978-0-87170-214-2, ISBN: 0-87170-214-2. The American Information Society, 1986.
 - [12] J. Breen. Expected lifetime of existing pvc water distribution systems. Technical report, TNO Science and Industry, De Rondom 1, 5600 HE Eindhoven, May 15 2006.
 - [13] Luis R. Carney and JR John J. Mecholsky. Relationship between fracture toughness and fracture surface fractal dimension in aisi 4340 steel. *Materials Sciences and Applications*, 4:258–267, 2013.
 - [14] B. J. Carter, P. A. Wawrzynek, and A. R. Ingraffea. Automated 3-d crack growth simulation. *International Journal for Numerical Methods in Engineering*, November 2003.
 - [15] Xi Chen, He Ren, , and Cees Bil. Inspection intervals optimization for aircraft composite structures considering dent damage. *Journal of Aircraft*, 51(1):303–309, 2014.
 - [16] J.M. Costa, J.T.B. Pires, F. Antunes, J.P. Nobre, and L.P. Borrego. Residual stresses analysis of nd-yag laser welded joints. *Engineering Failure Analysis*, 17(1):28–37, January 2010.
 - [17] MO Culjat, RS Singh, ER Brown, RR Neurgaonkar, DC Yoon, and SN White. Ultrasound crack detection in a simulated human tooth. *Dentomaxillofacial Radiology*, 34:80–85, 2005.
 - [18] M. de Freitas, F. Romeiro, and M. da Fonte. The environment effect on fatigue crack growth using a new chamber of vacuum. *Anales de Mecánica de la Fractura*, 2, 2006.
 - [19] DNV. *RECOMMENDED PRACTICE DNV-RP-C203 FATIGUE DESIGN OF OFFSHORE STEEL STRUCTURES*, APRIL 2010.
 - [20] R.J. Donahue, H.M. Clark, P. Atanmo, R. Kumble, and A.J. McEvily. Crack opening displacement and the rate of fatigue crack growth. *Int. J. Fract. Mech.*, 8:209–219, 1972.

References

- [21] N. E. Dowling. Mean stress effects in strain-life fatigue. *Fatigue and Fracture of Engineering Materials and Structures*, 32:1004–1019, September 2009.
- [22] Norman E. Dowling. *Mechanical Behavior of Materials*, volume Third Edition of ISBN 0-13-225609-06. Pearson, 2007.
- [23] DS/EN ISO 15653. *Metallic materials - Method of test for the determination of quasistatic fracture toughness of welds*, 1 edition, May 08 2010.
- [24] A. Dunbar, X. Wang, W.R. Tyson, and S. Xu. Simulation of ductile crack propagation and determination of ctod in pipeline steels using cohesive zone modelling. *Fatigue and Fracture of Engineering Materials and Structures*, 37(6):592–602, June 2014.
- [25] W Elber. Fatigue crack closure under cyclic tension. *Eng. Fract. Mech.*, 2:37–45, 1970.
- [26] F. Erdogan and G.C. Sih. On the crack extension in plates under plane loading and transverse shear. *ASME Journal of Basic Engineering* 85D, pages 519–527, 1963.
- [27] Ding fa FU, Chang qing ZHOU, Can LI, Guan WANG, and Luo xing LI. Effect of welding sequence on residual stress in thin-walled octagonal pipe-plate structure. *Transactions of Nonferrous Metals Society of China*, 24:657–664, 2014.
- [28] R. G. Forman, V. E. Kearney, and R. M. Engle. Numerical analysis of crack propagation in cyclic-loaded structures. *R. G. Forman, V. E. Kearney and R. M. Engle*, 89(3):459–463, Sep, 1967 *Journal of Fluids Engineering*.
- [29] S.C. Forth, M.A. James, and W.M. Johnston. Fatigue crack growth thresholds in d6ac steel. In *Advanced Fracture Mechanics for Life and Safety Assessments*. ECF15, 2004.
- [30] M. De Giorgi. Residual stress evolution in cold-rolled steels. *International Journal of Fatigue*, 33(Issue 3):507–512, March 2011.
- [31] A. A. Griffith. The phenomena of rupture and flow in solids. *Philosophical Transactions of the Royal Society of London*, 221:163198, January 1921.
- [32] P. J. Haagenzen and S J. Maddox. Iiwr recommendations on post weld improvement of steel and aluminium structures. Technical Report XIII-1815-00, The International Institute of Welding IIW Commission XIII, 4 July 2001.

- [33] Simo-Pekka Hannula, Hannu Hänninen, and Seppo Tähtinen. Influence of nitrogen alloying on hydrogen embrittlement in aisi 304-type stainless steels. *Metallurgical and Materials Transactions A*, 15(12):2205–2211, November 1984.
- [34] E. B. Haugen and P. H. Wirsching. Probabilistic design for random fatigue loads. *Journal of Engineering Mechanics Division*, 99:1165–1179, 1973.
- [35] Kåre Hellan. *Introduction to Fracture Mechanics*, volume 1. McGRAW-HILL, April 1984.
- [36] J.H. Heo, J.K Kim Kang, Y. Yoo, Y.S. Kim, and K.S. Urm. Study on the design guidance for low cycle fatigue in ship structures. In *9th Symposium on Practical Design of Ships and Other Floating Structures.*, Germany, 2004.
- [37] L.C Hollaway, M. K. Chryssanthopoulos, and S. S. J. Moy. Advanced polymer composites for structural applications in construction. In *ACIC2004*, volume 1 of ISBN 1 85573 736 1, page 277. Woodhead Publishing Limited.
- [38] ASTM International. *Standard Practice for Statistical Analysis of Linear or Linearized Stress-Life (S-N) and Strain-Life (e-N) Fatigue data*. West Conshohocken, e739-10 edition, June 2013.
- [39] P.E. Irving and C. J. Beevers. The effect of air and vacuum environments on fatigue crack growth rates in ti-6al-4v. *Metallurgical Transactions 5A*, 5(2):391–398, 1974.
- [40] G.R. Irwin. Analysis of stresses and strains near the end of a crack traversing a plate. *J. Appl. Mech.*, 24(3):361–364, 1957.
- [41] Michael S. Jepsen, Lars Damkilde, Niels A. Hansen, and Bendt Aarup. Increasing durability and lowering the overall cost of wave energy converters using ultra high performance concrete. In *European Wave and Tidal Energy Conference Series Proceedings of the 10th European Wave and Tidal Energy Conference*, volume 10th. Technical Committee of the European Wave and Tidal Energy Conference, 2013.
- [42] Michael S. Jepsen, Søren Heide Lambertsen, and Lars Damkilde. Design of ultra high performance fiber reinforced concrete shells. In *Proceedings of the 26th Nordic Seminar on Computational Mechanics*, 2013.
- [43] S. U. Khan, R.C. Alderliesten, J. Schijve, and R. Benedictus. On the fatigue crack growth prediction under variable amplitude loading. *Computational and experimental analysis of damaged materials*, pages 1–21, 2007.

References

- [44] Y. Kudryavtsev. Application of the ultrasonic method for residual stress measurement. In *Development of fracture toughness requirement for weld joints in steel structures for arctic service*, pages 62–76, 1985.
- [45] R. Kuguel. A relation between theoretical stress concentration factor and fatigue notch factor deduced from the concept of highly stressed volume. *Proc. ASTM*, 61:732–748, 1961.
- [46] Ashok Kumar and L. K. Singhal. Effect of temperature and strain distribution on martensitic transformation during uniaxial testing of aisi 304 stainless steel. *Metallurgical Transactions A*, 19(4):1021–1026, April 1998.
- [47] Søren Heide Lambertsen, Lars Damkilde, and Michael S. Jepsen. Fatigue of thin walled tubes in copper alloy cuni10. *Ships and Offshore Structures*, December 2014.
- [48] Søren Heide Lambertsen, Lars Damkilde, Anders Schmidt Kristensen, and Ronnie Refstrup Pedersen. Estimation of fatigue life of laser welded aisi 304 stainless steel t-joint based on experiments and recommendations in design codes. *World Journal of Mechanics*, 3:178–183, June 2013.
- [49] Søren Heide Lambertsen, Lars Damkilde, and Martin Dalgaard Ulrikson. Experimental quantification of metallurgy changes induced by laser welding in aisi 304 stainless steel. *Studies in Engineering and Technology*, 1(2):29–37, June 2014.
- [50] Søren Heide Lambertsen, Michael S. Jepsen, and Lars Damkilde. Investigation of patch coatings influence on the stress intensity factor for surface cracks. In Anders Logg, Kent-Andre Mardal, and André Massing, editors, *Proceedings of the 26th Nordic Seminar on Computational Mechanics*, number 26 in ISBN 978-82-92593-12-7, pages 210–213, 23-25 October 2013.
- [51] Steve Lampman, editor. *Characterization and Failure Analysis of Plastics*. ISBN: 978-0-87170-789-5. ASM International, 203.
- [52] Tong Lei, Li Shiqiu, and Xiong Junjiang. Material parameter modeling and solution technique using birth-death element for notched metallic panel repaired with bonded composite patch. *Chinese Journal of Aeronautics*, 27(2):445–452, 2014.
- [53] Liming Liu. *Modeling of Mixed-Mode Fatigue Crack Propagation*. May, Faculty of the Graduate School of Vanderbilt University, 2008.
- [54] Majbritt D. Lund. *Tensile strength of Glass Fibres*. Ph.d. dissertation, Section of Chemistry Department of Biotechnology Chemistry and Environmental Engineering Aalborg University, November 2010.

- [55] T. Mann, B. W. Tveiten, and G. Härkegård. Fatigue of welded aluminium t-joints. Stockholm, Sweden, Aug 11-13,, 2004. The 15th European Conference on Fracture, Advanced Fracture Mechanics for Life and Safety Assessments.
- [56] Peter Maranian. *Reducing Brittle and Fatigue Failures in Steel Structures*. American society of civil engineers, isbn 978-0-7844-1067-7 edition, 2010.
- [57] Matthieu Mazierea and Bernard Fedelicha. Simulation of fatigue crack growth by crack tip plastic blunting using cohesive zone elements. *Procedia Engineering*, 2(1):2055–2064, April 2010.
- [58] M.A. Meggiolaro, A.C.O. Miranda, J.T.P. Castro, and L.F. Martha. Stress intensity factor equations for branched crack growth. *Engineering Failure Mechanics*, 72:2647–2671, 2005.
- [59] Souiyah Miloud, A. Muchtar, A. K. Ariffin, Malek Ali, M. I. Fadhel, and Basem Abu Zneid. Finite element model of crack growth under mixed mode loading. *International Journal of Materials Engineering*, 2(5):67–74, 2012.
- [60] Robert L. Norton. *Machine Design*. ISBN 0-13-202012-2. Pearson International Edition, third edition edition, 2006.
- [61] Jeom Kee Paik and Anil Kumar Thavamballi. *Ultimate Limit State Design of Steel-Plated Structures*. Number ISBN: 978-0-471-48632-9. WILEY, 2003.
- [62] P.C. Paris, M. Gomez, and W.E. Anderson. A rational analytic theory of fatigue. *Trend Engineering*, 13:9–14, 1961.
- [63] Proc. 1st International Conference. *Weld Metal Hydrogen Cracking in Pipeline Girth Welds*, Australia, March 1999. Published by Welding Technology Institute of Australia (WTIA).
- [64] Walter Ramberg and William R. Osgood. Description of stress-strain curves by three parameters. Naca technical note no. 902, National Advisory Committee For Aeronautics, Washington DC., 1943.
- [65] JR. Reinier Beeuwkes. Determination of fracture stress and effective crack tip radius from toughness (K_{IC} and yield strength(σ_y)). Report AD-A274 014, Army Research Laboratory, 1993.
- [66] J.R. Rice. Mechanics of crack tip deformation and extension by fatigue. *Fatigue Crack Propagation, ASTM STP 415, Soc. Testing Mats*, page 247, 1967.
- [67] Michael Robert Roy. *Stress Intensity Factors for ship details*. Doctor of philosophy, Heriot-Watt University, 2009.

References

- [68] David Roylance. Introduction to fracture mechanics. Technical report, Department of Materials Science and Engineering Massachusetts Institute of Technology Cambridge, MA 02139, June 14 2001.
- [69] J.A Sauer and G.C Richardson. Fatigue of polymers. *International Journal of Fracture*, 16(6):499–532, December 1980.
- [70] Bernd M. Schönbauer and Stefanie E. Stanzl-Tschegg. Influence of environment on the fatigue crack growth behaviour of 12% cr steel. *Ultrasonics*, 53(8):1399–1405, 2013.
- [71] Mira Shehu, Peter Huebner, and Mimoza Cukalla. The behaviour of fatigue-crack growth in shipbuilding steel using the esacrack approach. *Materials and technology*, 40(5):207–210, 2006.
- [72] C.F. Shih, B. Moran, and T. Nakamura. Energy release rate along a three-dimensional crack front in a thermally stressed body. *International Journal of Fracture*, 30:79–102, October 1986.
- [73] R.P. Skelton, H.J. Maier, and H.-J. Christ. The baushinger effect, mas-ing model and the ramberg–osgood relation for cyclic deformation in metals. *Materials Science and Engineering: A*, 238(2):377–390, November 1997.
- [74] BRITISH STANDARD. *Guide to methods for assessing the acceptability of flaws in metallic structures*. BS 7910.
- [75] Ralph I. Stephen, Ali Fatemi, Robert R. Stephens, and Henry O. Fuchs. *Metal Fatigue In Engineering*, volume Second Edition. John Wiley and Sons, INC., 2001.
- [76] C.-M. SUH, M.-S. SUH, and N.-S. HWANG³. Growth behaviour of small surface fatigue cracks in aisi 304 stainless steel. *Fatigue and Fracture of Engineering Materials and Structures*, 35:22–39, August 2011.
- [77] L. Susmela, R. Tovo, and P. Lazzarin^b. The mean stress effect on the high-cycle fatigue strength from a multiaxial fatigue point of view. *International Journal of Fatigue - Cumulative Fatigue Damage Conference - University of Seville 2003 Cumulative Fatigue Damage Conference*, Volume 27(Issue 8):928–943, August 2005.
- [78] József Szalai and Ferenc Papp. A new residual stress distribution for hot-rolled i-shaped sections. *Journal of Constructional Steel Research*, 61:845–861, December 2005.
- [79] Hiroshi Tada, Paul C. Paris, and George R. Irwin. *The Stress Analysis of Cracks Handbook*. ISBN-10: 1860583040. Professional Engineering Publishing, third edition edition.

- [80] Keisuke Tanaka. Fatigue propagation from a crack inclined to the cyclic tensile axis. *Engineering Fracture Mechanics*, 6 Issue 3(doi:10.1016/0013-7944(74)90007-1):493–498, October 1974.
- [81] José R. Tarpani, Maria H.P. Braz, Waldek W. Bose Filho, and Dirceu Spinelli. Microstructural and fractographic characterization of a thermally embrittled nuclear grade steel: Part ii - quenching and tempering. *Materials Research*, 5(2):365–371, 2002.
- [82] Tso-Liang Tenga, Peng-Hsiang Changb, and Wen-Cheng Tsengc. Effect of welding sequences on residual stresses. *Computers and Structures*, 81(5):273–286, March 2003.
- [83] Tso-Liang Tenga and Chih-Cheng Lin. Effect of welding conditions on residual stresses due to butt welds. *International Journal of Pressure Vessels and Piping*, 75:857–864, 1998.
- [84] S. P. Timoshenko and J. N. Goodier. *Theory of Elasticity*, volume Third Edition of *Engineering Mechanics Mechanics Series*. McGRAW-HILL International Editions, 1970.
- [85] James R. Varner and Marlene Wightman. *Fractography of Glasses and Ceramics VI: Ceramic Transactions*, volume 230. The American Ceramic Society, isbn 978-1-118-27272-9 edition, 2012.
- [86] B K Venkatesha, K P Prashanth, and T Deepak Kumar. Investigation of fatigue crack growth rate in fuselage of large transport aircraft using fea approach. *Global Journal of Researches in Engineering Mechanical and Mechanics Engineering*, 14(1), 2014.
- [87] J. M. VITEK and S. A. DAVID. The effect of cooling rate on ferrite in type 308 stainless steel weld metal. *Welding Research*, pages 95–102, May 1988.
- [88] Ronald E. Walpole, Raymond H. Myers, Sharon L. Myers, and Keying Ye. *Probability and Statistics for Engineers and Scientists*, volume Eighth Edition. Pearson International Edition, 2007.
- [89] Matthew C. Walters, Glaucio H. Paulino, and Robert H. Dodds(Jr). Interaction integral procedures for 3-d curved cracks including surface tractions. *Engineering Fracture Mechanics*, 72:1635–1663, January 2005.
- [90] C. C. Weng and Teoman Pekoz. Residual stresses in cold-formed steel members. In *Ninth International Specialty Conference on Cold-Formed Steel Structures*, St. Louis, Missouri, U.S.A, November 8-9 1988.

References

- [91] J. Xu, T. Liu, X.M. Yin, B. S. Wong, and Syahrom B. Hassan. Automatic x-ray crack inspection for aircraft wing fastener holes. *2nd International Symposium on NDT in Aerospace*, Mo.5.A.4:1–8, 2010.
- [92] Chunjie Yea, Wenbin Kana, Yongfeng Lib, and Hongliang Pana. Experimental study of hydrogen embrittlement on aisi 304 stainless steels and rayleigh wave characterization. *Engineering Failure Analysis*, 34:228–234, December 2013.
- [93] Kun Zhou, Chun Yuan Shi, and Cheng Jin. Influence of cooling intensity on residual stress state of tig dressing zone for t-joint welded toe. *Applied Mechanics and Materials*, 148-149(10.4028/www.scientific.net/AMM.148-149.1289):1289–1294, December 2011.
- [94] Andrew S. Zurkinden, Søren H. Lambertsen, and Lars Damkilde. Structural modeling and analysis of a wave energy converter. In *Proceedings of the 25th Nordic Seminar on Computational Mechanics*, 2012.
- [95] Andrew S. Zurkinden, Søren Heide Lambertsen, Lars Damkilde, Zhen Gao, and Torgeir Moan. Fatigue analysis of a wave energy converter taking into account different control strategies. In *ASME 2013 32nd International Conference on Ocean, Offshore and Arctic Engineering: Ocean Renewable Energy*, volume 8 of ISBN 978-0-7918-5542-3, France, 2013 June 9–14. American Society of Mechanical Engineers.

Papers

Paper A

Fatigue of thin walled tubes in copper alloy CuNi10

Søren Heide Lambertsen, Michael S. Jepsen and Lars Damkilde

The paper has been published in the
Ships and Offshore Structures Accepted: 25. Nov 2014 Published online: 01.
April 2015

The layout has been revised.

Fatigue of thin-walled tubes in copper alloy CuNi10

Søren Heide Lambertsen*, Lars Damkilde and Michael S. Jepsen

Department of Structural Engineering, Aalborg University Esbjerg, Esbjerg, Denmark

(Received 3 June 2014; accepted 25 November 2014)

The current work concerns the investigation of the fatigue resistance of CuNi10 tubes, which are frequently used in heat exchangers of large ship engines. The lifetime performances of the exchanger tubes are greatly affected by the environmental conditions, where especially the temperature fluctuations and the harsh chloride environment cause fatigue and corrosion problems, respectively. A failure of the tubes will trigger an instantaneous shutdown of the engine. Thus, the paper will focus on a model for fatigue life estimation of the CuNi10 material. In the current case of a ship engine, the temperature fluctuations occur when the engine starts and stops. The difference in temperature at cool down or warm up between the exchanger and the exchange media will cause straining of the tubes. To investigate this phenomenon, a series of strain-based fatigue tests are carried out. Results are evaluated by means of the ASTM E739 guideline and one-sided tolerance limits factor method. The tests show good fatigue resistance and the risk for a failure is low in aspect to the case of a ship heat exchanger.

Keywords: strain-based fatigue; CuNi10 tubes; temperature fluctuation

1. Introduction

If a strain fluctuation generates damage in a structural component, the damage accumulation is governed by a ε - n relation (Bai et al. 2014) and this is generally conducted in cases where local plastic damage occur (Hasegawa et al. 2007; Liu et al. 2001). A plate with a hole, subjected to an in-plane force, can conveniently illustrate this phenomenon. Due to the stress concentration around the hole, when the elastic limit is reached, a plastic zone develops (Srivatsan et al. 1997). The ε - n damage criterion is also valid in cases of limited global strain plasticity, which can take place when temperature generates high strain levels (Mughrabi and Höppel 2000). The heat exchanger of a ship engine's air inlet system where the exchanger regulates the inlet temperature of the air is a typical case where temperature generates strain in the tube components. This type of heat exchanger can be seen in Figure 1. Where the shell structure is a rigid frame and the exchanger tubes are attached to this frame.

The tubes can be considered as a structural element with fixed ends, being subjected to significant temperature-related strains, caused by the temperature difference between the shell frame and the tubes. Due to the frequency of this condition in a ship engine, fatigue is an issue. When the engine starts and stops, high strain levels will develop. The start/stop process generates significant temperature variation inside the heat exchanger, because the exhausting gas instantaneously heat up the exchanger tubes, whereas the temperature rise in the shell structure is not instantaneous.

The temperature difference between the two components is responsible for the significant straining of the exchanger tubes. High temperature differences also develop when the inlet air is compressed. The compression of the air makes the combustion more efficient, but when the air is compressed the temperature will increase, which on the other hand decreases the efficiency of the combustion process. Thus, the inlet air temperature in large ship engines are controlled by the plate fin-and-tube type of heat exchanger, see Figure 1. In this type of exchanger, the temperature difference between the shell and the tubes is significant. The heat exchanger is a critical part, because an eventual failure of the tubes causes cooling water to leak, which creates pressure drop and a loss of flow in the exchanger system. A damaged heat exchanger can also cause collateral damage. This occurs if the inlet air temperature is not cooled sufficiently, which is the case if the heat exchanger fails and this condition reduces the efficiency of the engine, thus a shutdown is inevitable. It is, therefore, of great concern to investigate the fatigue behaviour of the CuNi10 heat exchanger tubes, creating a model for fatigue damage estimation of CuNi10 heat exchanger tubes.

2. Chemical composition and fatigue properties of CuNi10

The definition of the chemical composition in copper alloys can be established by a specific recommendation.

*Corresponding author. Email: shl@civil.aau.dk

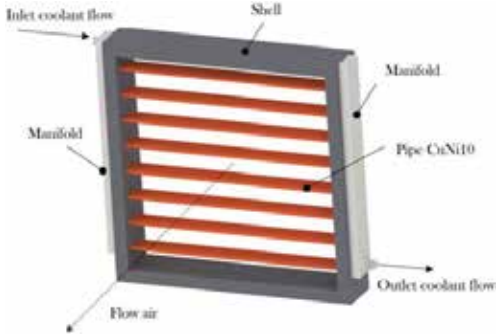


Figure 1. Illustration of the heat exchanger tubes and their location in the exchanger structure. (This figure is available in colour online.)

In the present case, the chemical composition is defined in accordance to ISO24273. Table 1 shows the chemical composition of the CuNi10 tubes.

Knowledge about the fatigue properties of the thin-walled tubes in the CuNi10 material is limited, even though several industries uses components made of CuNi10 tubes (Thompson and Wadsworth 1957). The fatigue data of this material are currently available for few structural elements such as plates, bars and Foils (CIDE. Forthcoming; Merchant et al. 1999; Jang et al. 2013). Applying these fatigue data in the design of CuNi10 tubes will be an incorrect estimate of the fatigue life. With this in mind, however, the properties of CuNi10 plates can give an indication of fatigue behaviour of CuNi10 tubes. The properties have been treated in CIDE (Forthcoming), Merchant et al. (1999) and Jang et al. (2013), and can be seen in Table 2.

In CIDE (Forthcoming), it is suggested that the fatigue resistance of CuNi10Fe1Mg can be estimated as 1/3 of the tensile strength. Here, it is important to realise that no low-cycle strain-based fatigue properties exist for the given material. Consequently, it will be the primary scope of the current work.

3. Lifetime estimation of thin-walled CuNi10 tubes

Generally, the fatigue damage estimation is based on material parameters of the non-treated base material, which also is the case for strain-based fatigue estimation (Charles et al. 2012; Henkel et al. 2010). The fatigue parameters for a given material are not reliable when the given struc-

Table 2. Known fatigue properties of CuNi10.

	$\Delta\sigma$	Run out(N)	Ref.
CuNi10Fe1.6Mn	70	10E7	(KME Forthcoming)
CuNi10Fe1.6Mn cold deformed	126	10E7	(KME Forthcoming)
CuNi10Fe1Mn	150	10E8	(CIDE (Forthcoming))

tural element contains residual stress from the manufacturing process. This residual stress obviously cause strain damage and thereby greatly affects the fatigue resistance (Lotsberg 2006; Chiou 2014). This is indeed the case of the heat exchanger tubes, which has residual stresses from the manufacturing process (Stevenson et al. 2005; Bridges et al. 2012). The strain damage is introduced due to folding, bending and other machining of the tubes. The assemblage of the final heat exchanger, connecting the tubes to the shell furthermore, causes residual stresses.

Due to the residual stresses in the tubes from the manufacturing process, it is essential to include the entire strain history in the fatigue life estimation (Agnew et al. 1999). When considering the fatigue estimation of exchanger tubes, the manufacturing process and the lifetime operations of the tubes contribute to the fatigue damage (Chiou 2014). Here, it is important to realise that when fracture occur in a given component, the accumulated manufacturing damage is often insignificant compared to the damage from the lifetime operations (Wang et al. 2014; Bai et al. 2014). Generally, the manufacturing process contributes with strain damage and the lifetime operations contribute with stress-based elastic damage.

It is common to approve a structural design if the plastic strain from the manufacturing and the elastic strain caused by ordinary operations does not cause failure. Occasionally, the fatigue life can be prolonged by introducing plastic strains in the right order compared to the loadings in ordinary operation. Introduction of plastic strains in the structural element changes the mean stress level, which as a result increases the fatigue life. The change in the mean stress level is obtainable by means of the strain history of the material. This technique is applicable in cases of local plastic strain in a component with a stress concentration but is infeasible to take advantage of in case of global plastic strain (Maier et al. 2006; Charles et al. 2012). The succeeding experiments are carried out to estimate the fatigue life of CuNi10 heat exchanger tubes, considering the entire strain history of the tubes.

Table 1. Chemical composition of CuNi10 according to ISO24273.

(%)	Cu	Fe	Mn	Ni	P	Pb	Si	C	Ti	S
CuNi10	89.8–84.9	0.5–2.0	0.5–1.5	9.0–11.0	0.02	0.02	0.02	0.02	0.1–0.5	0.05

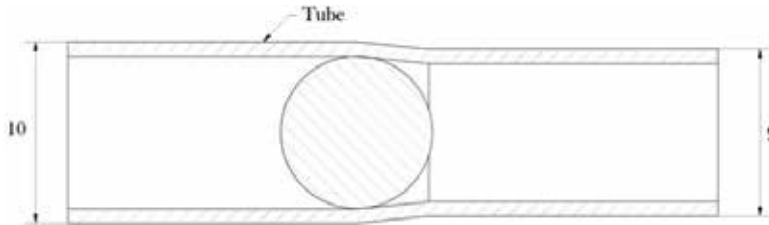


Figure 2. The deformation of the tubes in the manufacturing process. (This figure is available in colour online.)

4. Fatigue test of CuNi10 tubes – strain and damage history

The given tubes of a fin-and-tube heat exchanger have a diameter of 10 mm, and in the first step of manufacturing, they are delivered in coils to the production facility. The tubes have to be decoiled and stretched to straight elements. Thus, the decoiling process introduces plastic strain and following strain damage. In the second step, where the heat exchanger tubes have to be assembled with the shell structure, expansion of the tube is established to connect the tube and fin, causing plastic straining. The expansion is carried out by pushing a steel ball through the tube, see Figure 2. This part of the manufacturing process changes the outer diameter from 9 to 10 mm and results in a wall thickness of 1 mm. The tubes used in the current test are subjected to the exact same process to take the entire strain history into account in the fatigue testing.

4.1. Experimental set-up

The tubes used in the current test can be seen in Figures 3 and 4. The length of the tubes is 300 mm and the given length is chosen such that the free length reflects the actual tube when it is mounted in the heat exchanger. The fatigue testing is carried out by means of an MTS 858 servo hydraulic fatigue testing equipment. The machine is configured to carry out strain-controlled test with strain oscillation in the interval 0.00093–0.00187. The strain amplitude is based on the probable temperature fluctuation in the heat exchanger system. Accordingly, the temperature oscillation is in the interval 55 to 110 °C and the thermal expansion coefficient of CuNi10 is set to 1.70E-5 1/K. It is in the current set-up not possible to grip around the ends

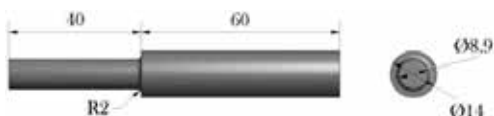


Figure 3. The bush attachment with solid gripping area. (This figure is available in colour online.)

of the specimens, due to the thin walls of the tube. In the test, a special attachment method is used, see Figure 3. The figure shows a bushing system that avoids the contact stresses introduced by a conventional gripping system (Wanga et al. 2014). Thus, to avoid the contact problem, a glued bush is used to transfer the load from the grip of the fatigue machine to the test specimen, see Figures 3 and 4.

The bushing design consists of a solid round bar with large gripping diameter and a part that fits inside the tube. The gap between the inner bush and the tube is 0.1 mm. Glue is infused in the space between the tube bush. The optimal strength of this connection is obtained by a minimum of space between the bush and the tube. The glue used for the mounting is 3M DP460 Epoxy. The curing time is 72 hours at 20 °C.

5. Method for fatigue life estimation

The measurements of the fatigue properties are stochastic in nature due to machine alignment and material imperfections. Since the preparation of the specimen significantly affects the fatigue testing result, it will be essential to conduct a standard method as ASTM E606/E606M. This guide describes the set-up of a fatigue testing experiment and also how to estimate parameters as the cyclic strain hardening exponent and the fatigue ductility coefficient. However, in the present case it is not feasible to fulfil all the particularities since the geometry is essential in this case. Thus, the test is carried out in accordance to the guide when it is possible.

To investigate the fatigue property and clarify the characteristic value for the fatigue resistance of CuNi10, statistical evaluation of the test series is needed (Baldwin and Thacker 2007). Generally, the ϵ - n curve is represented by a given probability to survive. By means of statistic evaluation of the fatigue data, it is possible to establish basis for a safe fatigue design criterion (Shama 2009). In the current case, the fatigue test results will be evaluated as strain amplitude versus fatigue life, as outlined in ASTM E730. This evaluation method is based on a confidence interval or at one-sided tolerance limit.

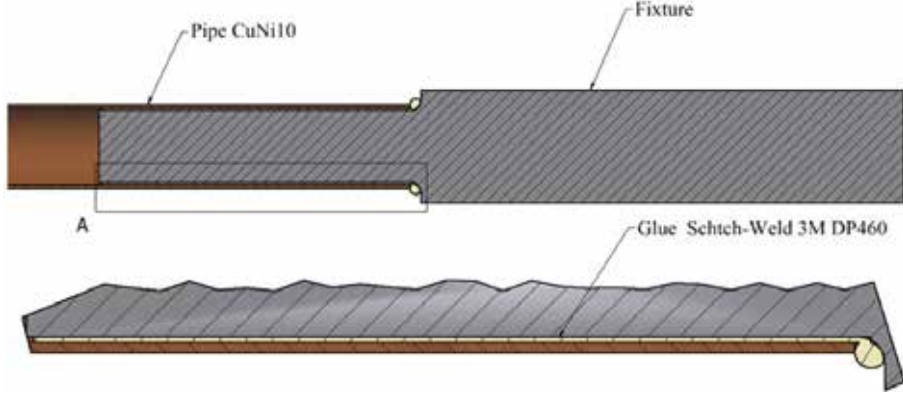


Figure 4. Glued connection between the gripping tools and the tube. (This figure is available in colour online.)

5.1. Test set-up

According to the ASTM E730 guideline, the minimum number of specimens to be tested is 12–24. In the current work, 39 specimens have been tested, which compared to ASTM E730 is a sufficient amount of specimens to get a reliable estimate of the fatigue behaviour (Sa and Razalla 2004). The first task is to determine a curve based on the results of the experiment. Accordingly, linearisation of the curve is implemented by using a logarithmic operator; $X = \log(X)$ and $Y = \log(Y)$. Subsequently, the data are presented as a linear relation, see the following equation:

$$Y = \hat{A} + \hat{B}X \quad (1)$$

Here, Y is the dependent variable in terms of number of cycles and X is the independent variable in terms of strain amplitude. \hat{A} and \hat{B} are parameters estimated by linear regression, by respectively,

$$\hat{A} = \bar{Y} - \hat{B}\bar{X} \quad (2)$$

$$\hat{B} = \frac{\sum_{i=1}^k (X_i - \bar{X})(Y_i - \bar{Y})}{\sum_{i=1}^k (X_i - \bar{X})^2} \quad (3)$$

Here, X_i is the independent variable in form of strain amplitude and Y_i is the dependent variable with represents the fatigue life. \hat{A} and \hat{B} are average values of the sample, which is represented as a median line based on the mean of the data-set. Each data-set has its individual variance and standard deviation. Thus, a diverse size of samples will generate an individual result of the parameters \hat{A} and \hat{B} . Estimation of the variance is conducted by the following equation:

$$\hat{\sigma}^2 = \frac{\sum_{i=1}^k (Y_i - \hat{Y}_i)^2}{k - 2} \quad (4)$$

where k is the total number of test specimens and $\hat{Y}_i = \hat{A} + \hat{B}X_i$. Consequently, a confidence band can be determined, which satisfy the probability that the variance and standard deviation are in the interval between the upper and lower confidence bands. ASTM E730 conducts this confidence band by producing strain-life curves by means of the Fisher–Snedecor distribution. These bands are computed by the following equation:

$$\hat{A} + \hat{B}x \pm \sqrt{2F_p\hat{\sigma}} \left[\frac{1}{k} + \frac{(x - \bar{x})^2}{\sum_{i=1}^k (x_i - \bar{x})^2} \right]^{\frac{1}{2}} \quad (5)$$

In proportion to Equation (5) correspond F_p to the confidence and the probability of survival (ASTM 1962).

Furthermore, a curve based on the one-sided tolerance limits by a normal distribution (Hall and Sampson 2007) are computed as shown in Figure 5. By Equation (6) includes the confidence interval and a probability of survival in the fatigue resistance value:

$$X = \bar{X} - k_{tol}S \quad (6)$$

Computation of this translation is based on the standard mean, standard deviation and the factor K_{tol} , where K_{tol} is the one-sided tolerance limit factor, which is based on the confidence interval and the probability of survival.

In proportion to these methods, it must be noticed that the ASTM E730 confidence band of Equation (5) takes into account the sample quality.

Consequently, the interval between the median line and the confidence band increases when moving away from the main cluster of data points as shown in Figure 5. However, when using Equation (6), the curve is translated by the sample mean value, which deteriorate the result when moving away from the main cluster of data points.

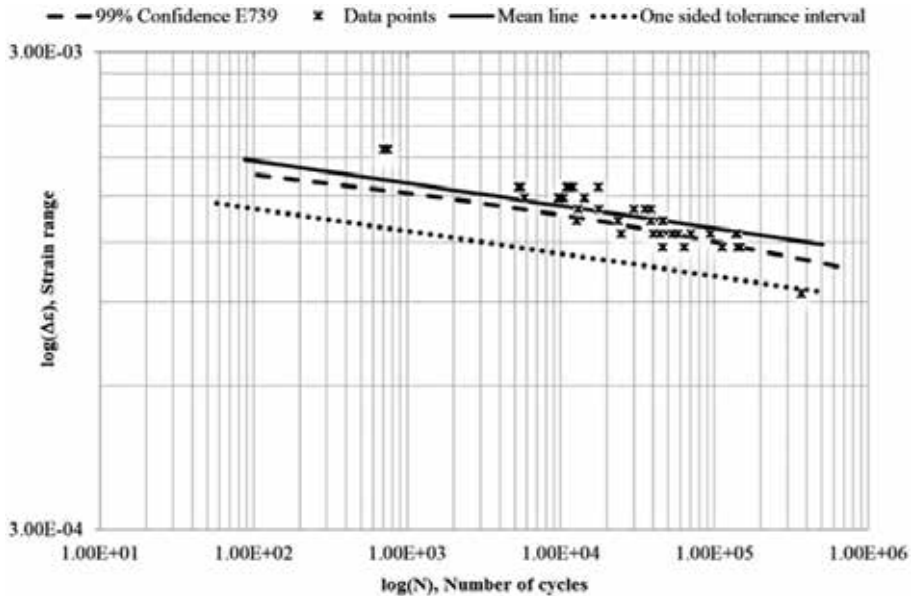


Figure 5. Regression curve and endurance limit. (This figure is available in colour online.)

6. Test evaluation

In Figure 5, the fracture surface of a given specimen can be seen. The fracture occurs in the midsection of all the specimens. The results of the fatigue testing for the CuNi10 tubes can be seen in Figure 5. The parameters in the regression analysis of Equation (1) are $A = -56.19$ and $B = -21.15$.

The 99% confidence interval based on the F distribution is shown in Figure 5 with a dashed line and the dotted line shows the one-sided tolerance limit with 90% confidence and 99% probabilities of survival.

7. Conclusion

Tubes of CuNi10 used in the heat exchanger systems of ship engines has been tested to study the material ability to resist fatigue damage originated by temperature fluctuations. The testing of the tubes has deduced a result that is consistent in the form of low spreading of the data point. Thus, a narrow band represents most of the data points. Additionally, the experimental testing reveals good fatigue resistance of the material, although the tubes are exposed to high level of deformation in the production phase. By comparing fatigue property to the value found in the literature, potential correlation is plausible. However, the literature data are based on run-outs and stress oscillation, whereas the test results in this paper are obtained by lower number of cycles and strain oscillation. Consequently, the results are not directly comparable with the literature but they indicate

a suitable correlation between the fatigue properties. To produce a curve that is appropriate in design cases, strain vs. fatigue life curves are produced. Since experimental testing involves uncertainties, a statistical evaluation is applied in the curve design. The curve produced by following the E739 guideline shows a narrow band because of consistent result in the experiment. Since the location of the data points is on both sides of the curve, fatigue estimation is non-conservative in proportion to designing of an application. The one-sided tolerance limit method is also applied in the chart depicted in Figure 5. Here, the curve is produced by probabilities for an application to survive and confidence interval limit, namely 99% and 90%, respectively. Thus, the curve proves appropriate for designing structures due to a limited probability for failure to occur in aspect to fatigue.

Disclosure statement

No potential conflict of interest was reported by the authors.

Nomenclature

$\Delta\sigma$:	Stress range
$\Delta\varepsilon$:	Strain range
Y :	Observations variable
X :	Controlled variable
\hat{A} :	regression coefficients
\hat{B} :	Regression coefficients

X_i :	Sample outcome
Y_i :	Sample outcome
\bar{X} :	Sample mean of X_i
\bar{Y} :	Sample mean of Y_i
$\hat{\sigma}^2$:	Variance
k :	Total sample size
F_p :	Statistics value based degrees of freedom
S :	Standard deviation
k_{tot} :	One-sided tolerance limit factor
N :	Number of cycles

References

- Agnew SR, Vinogradov AY, Weertman JR. 1999. Overview of fatigue performance of Cu processed by severe plastic deformation. *J Electron Mater*.28:1038–1044.
- [ASTM] American Society for Testing and Materials. 1962. Manual on fitting straight lines. Baltimore (MD): American Society for Testing and Materials.
- Bai Y, Xu W, Cheng P, Wang N, Ruan W. 2014. Behaviour of reinforced thermoplastic pipe (RTP) under combined external pressure and tension. *Ships Offshore Struct*. 9:464–474.
- Baldwin JD, Thacker JG. 2007. A strain-based fatigue reliability analysis method. *J Mech Des*. 117:229–234.
- Bridges R, Zhang S, Shaposhnikov V. 2012. Experimental investigation on the effect of low temperatures on the fatigue strength of welded steel joints. *Ships Offshore Struct*. 7:311–319.
- Charles C, Kwan F, Wang Z. 2012. The cyclic deformation behavior of severe plastic deformation (SPD) metals and the influential factors. *Metals*. 2:41–55.
- Chiou Y-C. 2014. Estimations of mechanical properties and fatigue life in pre-strained conditions. *J Chin Inst Eng*. 37:26–35.
- CIDEC. Forthcoming. Copper Data Sheet No K2, K5-K7. In Available from: http://www.copper.org/applications/marine/cuni/txt_DKI.html#13.
- Hall IJ, Sampson CB. 2007. One-sided tolerance limits for a normal population based on censored samples. *J Stat Comput Simul*. 2:317–324.
- Hasegawa S, Tsuchida Y, Yano H, Matsui M. 2007. Evaluation of low cycle fatigue life in AZ31 magnesium alloy. *Int J Fatigue* 29:1839–1845.
- Henkel S, Fischer J, Balogh L, Ungar T, Biermann H. 2010. Low-cycle fatigue behaviour and microstructure of copper and alpha-brass under biaxial load paths. The 15th International Conference on the Strength of Materials (ICSMA 15); 2009 Aug. 16–21; Dresden, Germany.
- Jang J-W, Hwangbo Y, Kim J-H, Lee H-J, Mag-isa AE, Lee S-B. 2013. Statistical characteristics of fatigue failure of copper thin films. *J Eng Mater Technol*. 135:041007-1–041007-9.
- KME. Forthcoming. Available from: http://www.kme.com/assets/uploads/files/datasheet/ri/mds_cuni10fe16mn_english.pdf
- Liu Z, Wang Y, Klein F. 2001. Cyclic deformation behaviour and fatigue crack propagation in AZ91HP and AM50HP. *Mater Sci Technol*. 17:264–268.
- Lotsberg I. 2006. Fatigue design of plated structures using finite element analysis. *Ships Offshore Struct*. 1:45–54.
- Maier HJ, Gabor P, Gupta N, Karaman I, Haouaoui M. 2006. Cyclic stress-strain response of ultrafine grained copper. *Int J Fatigue*. 28:243–250.
- Merchant HD, Minor MG, Liu YL. 1999. Mechanical fatigue of thin copper foil. *J Electron Mater*. 28:998–1006.
- Mughrabi H, Höppel HW. 2000. Cyclic Deformation and Fatigue Properties of Ultrafine-Grain Size Materials: Current Status and Some Criteria for Improvement of the Fatigue Resistance. Structure and Mechanical Properties of Nanophase Materials -Theory and Computer Simulation vs. Experiment, *Mater Res Soc Symp Proc*. 634:B2.1.1–B2.1.12.
- Sa P, Razalla L. 2004. One-sided continuous tolerance limits and their accompanying sample size Problem. *J Appl Statist*. 31:419–434. doi: 10.1080/02664760410001681710
- Shama MA. 2009. Basic concept of the factor of safety in marine structures. *Ships Offshore Struct*. 4:307–314.
- Srivatsan TS, Wei L, Chang CF. 1997. The cyclic strain resistance, fatigue life and final fracture behavior of magnesium alloys. *Eng Fract Mech*. 56:735–758.
- Stevenson ME, Barkey ME, McDougall JL. 2005. Stress in bent copper tubing: application to fatigue and stress corrosion cracking failure mechanisms. *J Fail Anal Prev*. 5:25–29.
- Thompson N, Wadsworth NJ. 1957. Structural changes and energy dissipation during fatigue in copper. *Br J Appl Phys*. 8:51–55.
- Wang F, Pan B, Shen Y, Cui W. 2014. On fracture resistance parameter from non-standard fracture test specimens of titanium alloy. *Ships Offshore Struct*. 9:177–185.
- Wanga F, Cuia W, Pana B, Shena Y, Huangb X. 2014. Normalised fatigue and fracture properties of candidate titanium alloys used in the pressure hull of deep manned submersibles. *Ships Offshore Struct*. 9:297–310.

Paper B

Experimental Quantification of Metallurgy Changes Induced by Laser Welding in AISI304 Stainless Steel

Søren Heide Lambertsen, Lars Damkilde, Martin D. Ulriksen

The paper has been published in the
Studies in Engineering and Technology Vol. 1(2), pp. 29–37, 2014.

The layout has been revised.

Experimental Quantification of Metallurgy Changes Induced by Laser Welding in AISI304 Stainless Steel

Søren Heide Lambertsen¹, Lars Damkilde¹ & Martin D. Ulriksen¹

¹Department of Structural Engineering, Aalborg University Esbjerg, Denmark

Correspondence: Søren Heide Lambertsen, Department of Structural Engineering, Aalborg University Esbjerg, Niels Bohrs Vej 8, DK-6700 Esbjerg, Denmark

Received: April 30, 2014 Accepted: May 28, 2014 Available online: June 11, 2014

doi:10.11114/set.v1i2.437

URL: <http://dx.doi.org/10.11114/set.v1i2.437>

Abstract

Laser-welded joints of stainless steel AISI304 are investigated experimentally to determine the transformation of austenite to martensite during the welding process. This transformation, which occurs in the welded region due to heating and residual stresses, can influence the fatigue and fracture properties of the affected material. Therefore, the scope of the present study is to determine the quantity of introduced martensite in the welded region and hereby clarify the influence of laser welding on the fatigue and fracture properties of welded AISI304 joints. The quantification of martensite concentration is carried out by use of four different methods, namely Lichtenegger and Bloech (LB1) etching, Ferritoscope, X-ray diffraction (XRD), and Vickers hardness. It is found that a concentration of 1-1.6 % martensite is introduced in the laser-welded area; a quantity that has insignificant influence on the fatigue properties of the joints.

Keywords: Metallurgical transformation, Martensitic phase, AISI304, Laser-welded joints.

1. Introduction

In the constant attempt to optimize the employment of joints in steel structures, various welding methods have been developed since the Second World War. One of these methods is laser welding in which the heat source yielding the melting process is generated by a laser beam. This specific welding method has a major advantage compared to other methods, as it facilitates the joining of plates in several configurations (Li et al., 2014). For instance, the keyhole technique (Li et al., 2014) makes it possible to weld perpendicular plates in one process (Morteza et al., 2007). This is illustrated in figure. 1.

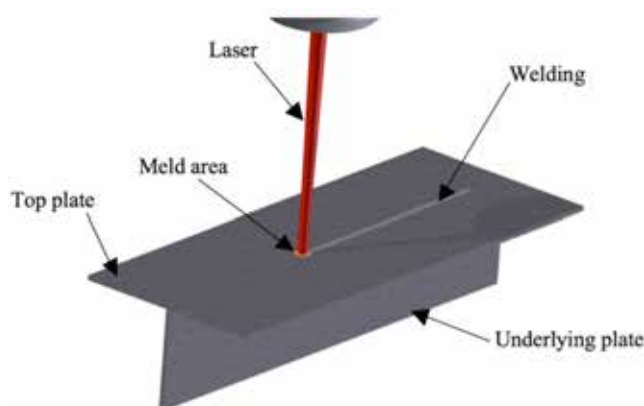


Figure 1. Illustration of the keyhole laser welding method in T-joints.

In the keyhole laser welding method, the top plate is penetrated with laser such the heat input is added to the underlying plate. Hereby, the liquid material in the heated zone will interweave and, thus, create the joint. When a welding is added

to a structure, it affects the material at both the melted area and the area next to the welding, known as the heat-affected zone (HAZ). It is well known that the HAZ is of interest with regards to the durability of welded joints. However, when using laser welding, higher temperature gradients occur compared to conventional welding methods. These higher temperature gradients affect the joint, often by reduction of the durability.

In this laser welding process, metallurgical transformations, which alter, i.e., the fatigue and fracture properties of the affected material (Müller-Bollenhagen et al., 2010; Jayaprakash et al., 2004; Rodríguez-Martínez et al., 2013), can be triggered. In stainless steel AISI304, this transformation occurs under certain circumstances; primarily when the material temperature is below 50 degrees Celsius (Rodríguez-Martínez et al., 2013). However, it is the impact from the welding that causes the transformation. In particular, accumulated stresses and/or deformations can yield a transformation from austenitic to martensitic phase (Kirk et al., 1999). The thermal variations produce no metallurgical changes in AISI304 (Roth et al., 2010; Mostafa et al., 2012), but the welding process can accumulate residual stresses that can trigger metallurgical transformations (Li et al., 2014; Mostafa et al., 2012; Mitra et al., 2004). In some cases, the residual stress level is beyond $\sigma_{0.2}$ in the welded region due to the asymmetric cooling of the structure. Consequently, plastic strains are introduced, enabling activation of metallurgical transformation in the material (Ashok et al., 1989; Paulo et al., 2013). This metallurgical transformation can only occur in a specific temperature interval. For instance, if examining a thin plate made from AISI304, the temperature interval is about 40-50 degrees Celsius, thus providing a measure by which the quantity of transformation can be controlled. This is documented in (Li et al., 2014; Mostafa et al., 2012; Smaga et al., 2008) where a significant temperature rise due to adiabatic heating suppressed the transformation.

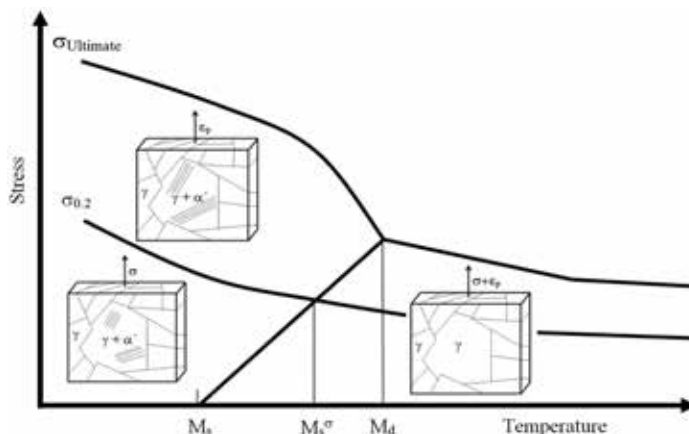


Figure 2. STT and DTT diagram of the γ - α' transformation, where γ and α' is austenitic and martensitic structure.

Figure 2 shows the correlation of Stress-Temperature-transformation (STT) and Deformation-Temperature-Transformation (DTT). M_d is the maximum temperature at which transformation by deformation occurs, and M_s is the transformation start temperature. At the $M_s\sigma$ temperature, the martensite transformation occurs when the stress level is above $\sigma_{0.2}$. For stainless steel, $M_s\sigma$ is between -10 and 50 degrees Celsius (Roth et al., 2010).

Since the transformation from austenite to martensite can result in significant degradations of fatigue and fracture properties of steel material, multiple methods have been developed to estimate the volume of generated martensite concentration. In the present study, four of such methods, namely Lichtenegger and Bloech (LB1) etching, Vickers hardness, ferritescope, and x-ray diffraction (XRD), are utilized to quantify the amount of introduced martensite in laser-welded AISI304 joints. As described in details in Section 3, each of the methods adds information about the concentration of martensite, thus by employing these four methods instead of just one, the reliability of the martensite concentration estimation is improved significantly. If the estimation is based on one method, it can be imprecise since each method has inherent shortcomings. For instance, the ferritescope measures the magnetic elements and therefore it cannot distinguish between martensite and ferrite elements in the welding.

The present study will investigate the martensite concentrations of the base material, welded zone and an oscillation load influence on the amount of martensite. The scope is to identify which influence the metallurgical changes has on the fatigue and fracture properties.

2. Experimental Procedure

In the experimental work, specimens cut out mechanically from a 1 mm thick AISI304 stainless steel plate are utilized. The chemical composition is determined by spectroscopy and the result is; 0.036 C, 0.42 Si, 1.28 Mn, 0.031 P, 0.0010 S, 18.21 Cr, 8.30 Ni, and 0.050 N.

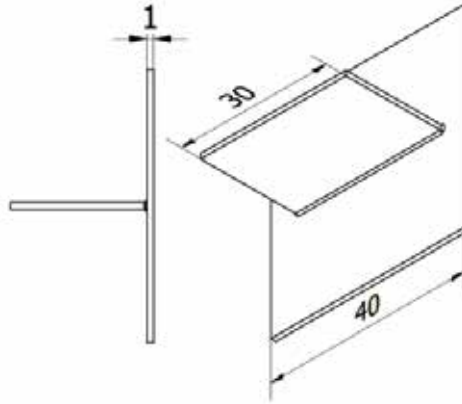


Figure 3. Sketch of specimen used in the experiments.

In figure 3, a sketch of the specimens is shown. The welding was carried out with a carbon dioxide Nd:YAG laser, which penetrates the surface with a spot size of 3 mm. The power input is 4 kW, with the laser head moving with a speed of 200 mm/min.

As stated in the introduction, the transformation from austenitic to martensitic phase can only occur in the specific temperature interval, $[M_s; M_d]$ (Kirk et al, 1999; Lin, et al., 2007; Müller-Bollenhagen et al., 2010). M_s and M_d are calculated with Eq. (1) and Eq. (2).

$$M_s (^{\circ}\text{C}) = 502 - 810(\%C) - 1230(\%N) - 13(\%Mn) - 30(\%Cr) - 12(\%Ni) - 54(\%Cu) - 46(\%Mo) \quad (1)$$

$$M_d (^{\circ}\text{C}) = 413 - 462(\%C + \%N) - 9.2(\%Si) - 8.1(\%Mn) - 13.7(\%Cr) - 9.5(\%Ni) - 18.5(\%Mo) \quad (2)$$

Evidently, the content of C and N has the highest influence on the martensite trigger temperature. In this study, M_s and M_d define when the transformation occurs.

2.1 LB1 Etching

The LB1 etching method facilitates observation of numerous metallurgical phenomena (Alexander et al., 2012). When etching AISI304, especially two of these phenomena are of interest namely transformation-induced-plasticity (TRIP), which is martensite introduced by plasticity, and twinning-induced-plasticity (TWIP) (Roth et al., 2010). It can be challenging to distinguish between TRIP and TWIP in a microscope view. This is exemplified in figure 4 where three metallurgic compositions, TRIP, TWIP, and austenite, are presented. Clearly, judgments are necessary to achieve satisfactory outline of the microscope view. However, etching will give an appraisal of the quantity of austenitic, martensitic and ferrite phase (Paulo et al., 2013). Etching should be conducted immediately after mixing to ensure that the dyeing will be sufficient.

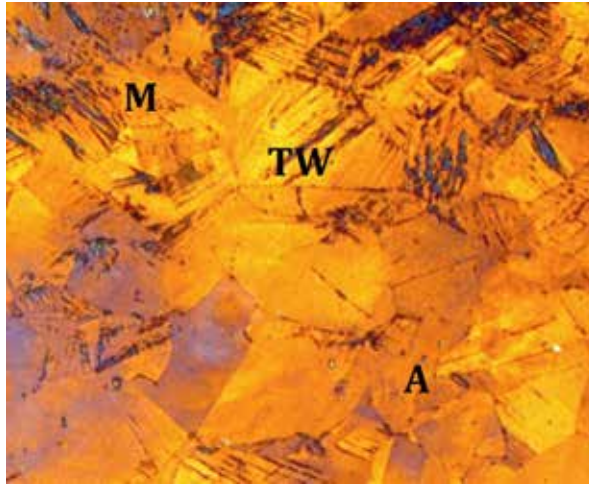


Figure 4. Etching of AISI304 with LB1. Austenite (A), martensite (M) and TWIP (TW) formation are present.

2.2 Vickers Hardness Methods

The hardness of the material in the HAZ and the far field are measured by Vickers hardness. A concentration of martensitic phase will yield a harder material, hence facilitating location of this concentration. Three locations on the joint are measured; one in the center of the welding plus one 1 mm and one 5 mm from the center of the welding. The hardness is then obtained as the mean of eight tests at each measurement point. By doing so, reliable results are obtained in a simple way.

2.3 Ferrite Scope

The ferrite scope measures the amount of ferrite magnetic elements in the welded material (Alexander et al., 2012). The measurements take place in two points, as indicated in figure 5. The results in these points are then converted to an equivalent concentration of martensitic phase via Eq. (3).

$$\text{Vol \% martensite} = 1.75 \cdot \text{Ferritescope result} \quad (3)$$

As mentioned in the introduction, the ferritescope method has a shortcoming because it cannot distinguish between different magnetic elements. This is an issue in the present study since AISI304 can contain two magnetic elements, in the form of martensite and δ -ferrite.

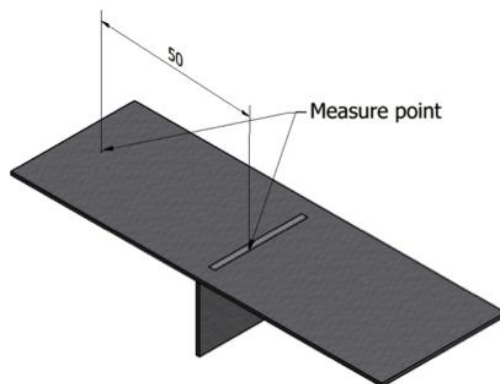


Figure 5. Ferritescope measurement points on test specimen. The point at the welding is denoted center, while the other point is denoted far field.

The presence of the latter in the HAZ is generally increased with high cooling rate (Eichelman et al., 1952). The highest concentration of δ -ferrite is located in the zone between the melted and non-melted material (Prohaska et al., 2012). Consequently, results from other methods, e.g. LB1, are a necessity to quantify the amount of martensite.

2.4 X-ray Diffraction

XRD measures the reflection from the examined material. Hereby, the distance between the atoms can be determined and the crystal types identified. This method is based on Bragg's Law of Diffraction, which measures the average spacing between layers or rows of atoms (Li et al., 2014; Ashok et al., 1989).

In this study, Philips Xpert 3kV Cu X-Ray Diffraction equipment is used to examine two types of specimens; welded and non-welded. Strain has been introduced to the non-welded specimens in accordance with four levels, namely 0%, 10%, 20% and 25% elongation. By doing so, the results can be used to analyse strain-introduced transformation in the form of martensitic phase (Kurc et al., 2013; Jayaprakash et al., 2004).

3. Experimental results

The stress and deformation transformation levels of martensite are calculated by means of Eq. (1) and (2), resulting in $M_s = -236^\circ\text{C}$ and $M_d = 42.5^\circ\text{C}$, respectively. The M_s is so low that no stress-induced transformation occurs in the weld. Since $M_d = 42.5^\circ\text{C}$, the cooling subsequent to the welding procedure can introduce small amounts of DTT by thermal deformation. The transformation can only occur in the temperature interval from 42.5°C to the surrounding temperature, thus the transformation level seems to be low such only a small concentration of martensite can be developed in the welded area. In the following, the four-presented methods for detecting metallurgical changes will be applied to examine the martensite concentration.

3.1 Application of LB1 Etching

The amount of transformation can be detected with LB1 etching (Talonen et al., 2004). The etching is used at a section cut of the welding, and hereby a microscope photograph like the one in figure 6 can be established. The blue and brown colors in figure 6 indicate martensite and austenite concentrations, respectively. Evidently, martensite concentrations are introduced in the melted area and in the middle of the plate. The highest concentration of martensite is in the joint between the two components. Additionally, the microscope photograph in figure 6 also shows a concentration of martensite at the cut surface and along the rolling lines in the middle of the plate. The transformations in these areas are caused by plastic deformations in the manufacturing process.

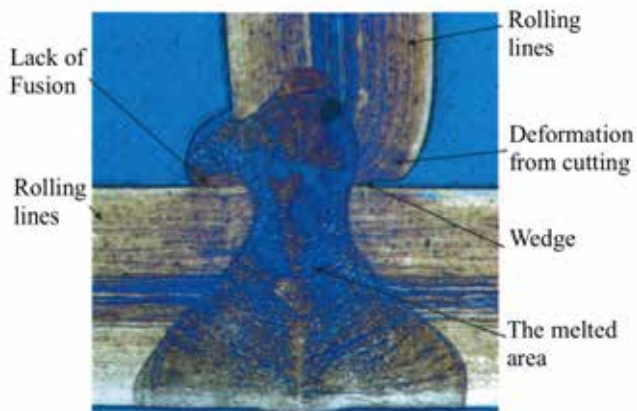


Figure 6. Etching of AISI304 with LB1 with indication of austenite, martensite and TWIP formation.

3.2 Application of Vichers Hardness

In Table 1, the results from the Vickers hardness test are presented. Here, it is seen that the maximal hardness is found at the center of the weld, with a value of 200 HV. The hardnesses found in the two adjacent points are 185 HV and 183 HV, respectively. The findings clearly indicate martensite in the welded region.

Table 1. Vickers hardness in specific distances from the welding center.

Distance (mm)	Hardness (HV)
0	200
1	185
5	183

3.3 Application of Ferritescope

The concentration of ferromagnetic elements is determined through a ferritescope. In the far field area of the welded specimen, a concentration of 0.19-0.2 ferromagnetic elements is found, while the level in the center is 0.5-0.66. The other welded specimen, which additionally has been loaded with an oscillation load, has a concentration of 0.2-0.22 in the far field area and a concentration of 0.83-0.97 in the center. By substituting these results into Eq. (3), the corresponding percentage martensitic phase concentrations are calculated. In Table 2, these calculated concentrations are given.

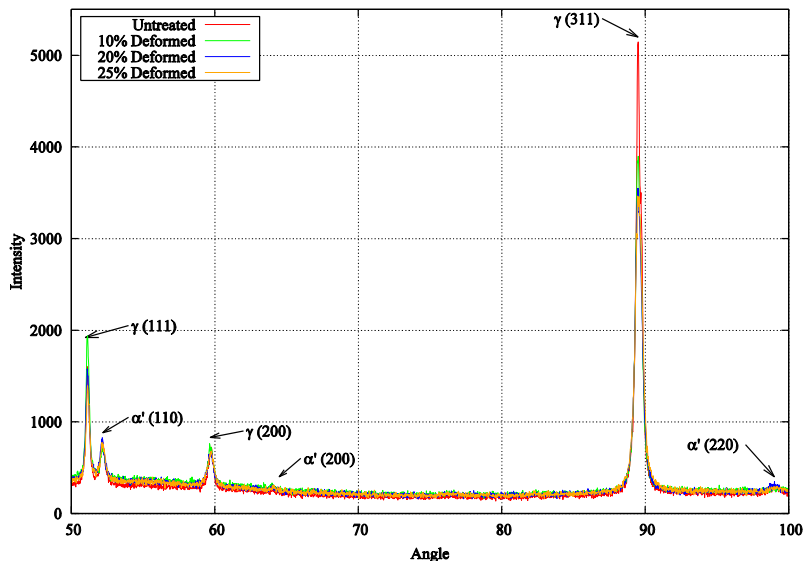
Table 2. Results of percentage martensitic phase concentration found through ferritescope test of two different specimens.

Ferritescope results	Welded	Welded and loaded (HV)
Far Field	0.34%	0.37%
Center	1.00%	1.60%

Evidently, the amount of martensitic phase is 0.66 % higher in the center than in the far field for the welded specimen. This difference increases to 1.23 % when examining the welded and loaded specimen.

3.4 Application of X-ray Diffraction

In the XRD study, references are generated for comparison with the welded specimens. The references are composed of, respectively, undeformed (i.e. untreated) and deformed non-welded specimens of the base material, AISI304. As seen in figure 7, where the XRD test results for the reference specimens are presented, the deformations lead to significant decreases in the intensity of $\gamma(311)$ and significant increases in the intensity of $\gamma(111)$. Furthermore, it is observed that the intensities of $\alpha'(200)$ and $\alpha'(220)$ increase slightly as a consequence of deformation.

Figure 7. XRD test results showing γ and α' phase in references, i.e. untreated and deformed AISI304 specimens

In figure 8, the results obtained in two analogous XRD tests of the laser-welded specimens are shown. Since the results indicate consistency, only one set of test results is compared directly to the reference specimens, see figure 9.

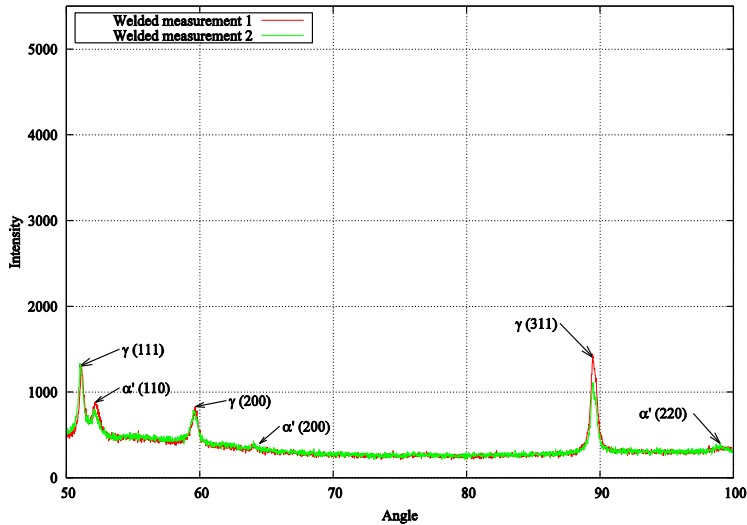


Figure 8. XRD show γ and α' phase in welded specimens of AISI304

When inspecting figure 9, it is evident that the intensities of γ (111) and γ (311) are lower in the welded specimen compared to the untreated and deformed ones. This is due to disorder from the welding process. The intensity of α' (200) is, however, highest in the welded specimen and lowest in the untreated, hence indicating a limited increase of martensite in the welded area. Regarding α' (110), it is observed that the peak is wider for the welded specimen compared to the corresponding peaks for the other specimens. This indicates that a larger amount of α' (110) is present in the welded specimen. The highest changes is γ (311) between the welded material and the untreated material. For the remaining phases, i.e. α' (220) and γ (200), insignificant changes are introduced as a consequence of welding.

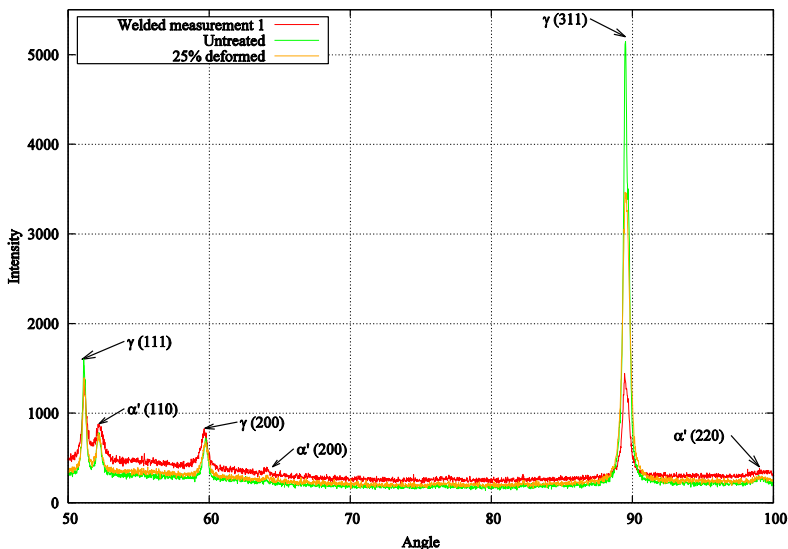


Figure 9. XRD test results showing γ and α' phase in welded, deformed, and untreated AISI304 specimens.

4. Conclusion

In this study, laser welding-induced changes in the microstructure of AISI304 specimens are investigated experimentally. In particular, the concentrations of martensitic phase have been of interest. These concentrations have been quantified by use of four different methods, namely LB1 etching, ferritescope, x-ray diffraction (XRD), and Vickers hardness, and hereby the following results have been obtained:

- LB1 etching shows a concentration of martensitic phase in the laser-welded material.
- The Vickers hardness test shows a significant increase of the hardness in the welded area. This indicates presence of a limited concentration of martensite in the welded area.
- The ferritescope result is translated to percent- tage martensitic phase concentration. In the welded specimen, the amount of martensitic phase is approximately 1 % and 0.3 % in the welded zone and at the far field, respectively. By adding an oscillation load the martensitic phase concentration increases to 1.6 % in the welded zone and 0.35 % at the far field.
- The XRD test shows a disorder in the microstructure in the melted material. Small increases in a' (110) and a' (200) are observed, hence indicating a limited increase of martensite.

The summative conclusion is that the laser welding- induced increase in martensite is less than 1 %, thus the laser welding method has limited effect on the fatigue parameter.

References

- Li, Xibin, Lu, Fenggui, Cui, Haichao, Tang, Xinhua, & Wu, Yinhua. (2014). Numerical modeling on the formation process of keyhole-induced porosity for laser welding steel with T-joint. *The International Journal of Advanced Manufacturing Technology*.
- Morteza, Z., Reza bateni, M., Poladi, A., & Jerzy, A. S. (2007). The formation of martensite during wear of AISI 304 stainless steel, *Wear*, 674–678. <http://dx.doi.org/10.1016/j.wear.2007.01.107>
- Müller-Bollenhagen, C., Zimmermann, M., & Christ, H. J. (2010). Adjusting the very high cycle fatigue properties of a metastable austenitic stainless steel by means of the martensite content. *Procedia Engineering*, 2(1), 1663–1672. <http://dx.doi.org/10.1016/j.proeng.2010.03.179>
- Jayaprakash, Sumanth Kumar, J., Sivaprasad, K., & Ganesh Sundara Raman, S. (2004). EFFECT OF GRAIN SIZE ON FRETTING FATIGUE BEHAVIOUR OF AISI 304 STAINLESS STEEL. *International Symposium of Research Students on Materials Science and Engineering*, pp. 1-8.
- Rodríguez-Martínez, J. A., Rusinek, A., Pesci, R., & Zaera, R. (2013). Experimental and numerical analysis of the martensitic transformation in AISI 304 steel sheets subjected to perforation by conical and hemispherical projectiles. *International Journal of Solids and Structures*, 50(2), 339-351.
- Kirk, D., & Payne, N. J. (1999). Transformations Induced in Austenitic Stainless Steels by Shot Peening, in ICSP, WARSAW, POLAND, pp. 15-22.
- Roth, I., Kübbeler, M., Krupp, U., Christ, H. J., & Fritz, C. P. (2010). Crack initiation and short crack growth in metastable austenitic stainless steel in the high cycle fatigue regime. *Procedia Engineering*, 941–948. <http://dx.doi.org/10.1016/j.proeng.2010.03.102>
- Mostafa, E., Abbas, Z. H., & Ali, M. (2012). An investigation into the mechanical behavior of a new transformation-twinning induced plasticity steel. *Materials & Design*, 39, 279–284.
- Mitra, A., De, P. K., Bhattacharya Sr, D. K., Srivastava, P. K., & Jiles, D. C. (2004). Ferromagnetic Properties of Deformation-Induced Martensite Transformation in AISI 304 Stainless Steel. *Metallurgical and Materials Transactions A*, 35(2), 599-605.
- Ashok, K., & SInghal, L. K. (1989). Effect of Strain Rate on Martensitic Transformation during Uniaxial Testing of AISI-304 Stainless Steel. *Metallurgical Transactions A*, 20A, 2857-2859.
- Paulo, R. M. (2013). Metallurgy and materials, INOX 2010 - 10th Brazilian Stainless Steel Conference, pp. 221-225.
- Smaga, M., Walther, F., & Eifler, D. (2008). Deformation-induced martensitic transformation in metastable austenitic steels. *Materials Science and Engineering: A*, 483–484, 394–397.
- Chi-Ming, Lin, Gen-Huey, Lai, Yu-Che, Chen, Yung-Tse, Chang, & Weite Wu. (2007). Characterization and Mechanism of 304 Stainless Steel Vibration Welding. *Materials Transactions*, 48(9), 2319 to 2323. <https://www.jim.or.jp/journal/e/pdf3/48/09/2319.pdf>

Alexander, K. A., Andreas, W., Steffen, W., & Piotr, R. S. (2012). STT and DTT Diagrams of Austenitic Cr–Mn–Ni As-Cast Steels and Crucial Thermodynamic Aspects of $\gamma \rightarrow \alpha'$ Transformation. *Steel research international*, 83(6), 576–583.

Eichelman Jr, G. H., & Hull, F. C. (1952). The Effect of Composition on the Temperature of Spontaneous Transformation of Austenite to Martensite in 18-8 Type Stainless Steel. *Transactions of A.S.M.*, 45, 77-95.

Prohaska, M., Panzenbowck, M., Anderl, H., & Kordasch, W. (2012). Influence of chemical composition and microstructural parameters on speed of sound of various materials used for high-pressure applications, in 18th World Conference on Nondestructive Testing, Durban, South Africa, 16-20 April 2012.

Li, Yongfeng, Bu, Fuming, Kan, Wenbin, & Pan, Hongliang. (2012). Deformation-Induced Martensitic Transformation Behavior in Cold-Rolled AISI304 Stainless Steels. *Materials and Manufacturing Processes*, 28(3), 256-259.

Kurc, A., & Stoklosa, Z. (2013). The effect of ($\gamma \rightarrow \alpha'$) phase transformation on microstructure and properties of austenitic Cr-Ni steels. *Archives of Materials Science and Engineering*, 41(2), 85-94.

Talonen, J., Aspegren, P., & Hnninen, H. (2004). Comparison of different methods for measuring strain induced α -martensite content in austenitic steels. *Materials Science and Technology*, 1506-1512.



This work is licensed under a [Creative Commons Attribution 3.0 License](https://creativecommons.org/licenses/by/3.0/).

Paper C

Estimation of Fatigue Life of Laser Welded AISI304 Stainless Steel T-Joint Based on Experiments and Recommendations in Design Codes

Søren Heide Lambertsen, Lars Damkilde, Anders Schmidt
Kristensen, Ronnie Refstrup Pedersen,

The paper has been published in the
World Journal of Mechanics Vol. 3(3), pp. 178–183, 2013.

The layout has been revised.

Estimation of Fatigue Life of Laser Welded AISI304 Stainless Steel T-Joint Based on Experiments and Recommendations in Design Codes

Søren Heide Lambertsen, Lars Damkilde, Anders Schmidt Kristensen, Ronnie Refstrup Pedersen

Division of Structures and Materials, Aalborg University Esbjerg, Esbjerg, Denmark

Email: shl@civil.aau.dk

Received February 11, 2013; revised April 9, 2013; accepted May 10, 2013

Copyright © 2013 Søren Heide Lambertsen *et al.* This is an open access article distributed under the Creative Commons Attribution License, which permits unrestricted use, distribution, and reproduction in any medium, provided the original work is properly cited.

ABSTRACT

In this paper the fatigue behavior of laser welded T-joints of stainless steel AISI304 is investigated experimentally. In the fatigue experiments 36 specimens with a sheet thickness of 1 mm are exposed to one-dimensional cyclic loading. Three different types of specimens are adopted. Three groups of specimens are used, two of these are non-welded and the third is welded with a transverse welding (T-Joint). The 13 laser welded specimens are cut out with a milling cutter. The non-welded specimens are divided in 13 specimens cut out with a milling cutter and 10 specimens cut out by a plasma cutter. The non-welded specimens are used to study the influence of heat and surface effects on the fatigue life. The fatigue life from the experiments is compared to fatigue life calculated from the guidelines in the standards DNV-RP-C203 and EUROCODE 3 EN-1993-1-9. Insignificant differences in fatigue life of the welded and non-welded specimens are observed in the experiments and the largest difference is found in the High Cycle Fatigue (HCF) area. The specimens show a lower fatigue life compared to DNV-RP-C203 and EUROCODE 3 EN-1993-1-9 when the specimens are exposed to less than 4.0 10^6 cycles. Therefore, we conclude that the fatigue life assessment according to the mentioned standards is not satisfactory and reliable.

Keywords: AISI304; Laser Welding; Austenite; Martensite

1. Introduction

S-N curves are based on experimental data, where traditional welding methods are adopted. Therefore, the S-N curves may not correctly represent the fatigue life, where the laser welding method and other non-traditional welding methods are applied. Nowadays the high-speed laser weld method is widely used in the industry. Hence the standards might need new S-N curves that correctly represent the fatigue life of laser welded stainless steel materials. Laser welding is commonly used to assemble small components in the biomedical, electronics and aerospace industry [1].

In these applications weldings require a very small melted area, hence small laser beams less than 1 kW are used. The Nd:YAG laser beam has been developed further and the maximum heat output is increased to 6 kW [2]. Consequently, it is possible to weld sheet components with a higher thickness. Today AISI304 sheets with a thickness up to 12 mm can be assembled with a modern Nd:YAG laser. Therefore, the application area of the

laser welding method is expanded to include traditional welding tasks and the laser welding replaces the TIG and MIG/MAG welding methods.

One of the most significant types of laser welding is the keyhole method [3], which is also used in this study. With the keyhole method it is possible to weld, in one process, perpendicular plates. Therefore, in production of perpendicular plate assemblies the keyhole welding method permits high production volume and a low manufacturing price. The possibility to weld a perpendicular assembly in one single process has been requested by the industry for many years. Therefore, the keyhole method became one of the most important welding procedures with the laser technology. However, when the keyhole welding is used higher stress concentrations are generated in the welded zone and consequently a lower fatigue life can occur. The fatigue behavior of dynamic loaded structures, where the keyhole method is adopted has not been investigated thoroughly in the literature. Therefore, it is necessary to investigate the fatigue life of T-joints exposed to dynamic loading. Laser welding is more ef-

fective compared to traditional welding methods, *i.e.*, the process is faster and more energy is supplied to a smaller welding area [4]. However, the small melted area cools down rapidly and high thermal stresses are introduced [5]. The thermal stress influences the metallurgy in the welding area and thereby the mechanical properties [6].

1.1. Guidelines

The present guidelines for fatigue assessment of different types of welded joints according to the design standards are quite general. For stainless steel the assessment is independent of several important aspects mentioned next. Geometrically, the laser welding also cause a smaller welding compared to traditional welding types. However, the smaller welding toe implies in most cases higher stress concentrations and accordingly the fatigue life is decreased. Furthermore, rotating bending fatigue tests [7] with AISI304 materials have shown that the fatigue life is sensitive to the initial defects in the material. The higher stress concentrations are not properly accounted for in the current design guidelines because they are based on experiments with relatively smooth welding's. The guidelines suggest that an averaged thickness of the sheets and an averaged size of welding toes are used in the fatigue assessment. A fatigue calculation based on these averaged values may not provide a reliable estimate of the fatigue life. The size of the welding toe is known to have a greater impact on the fatigue life in a thin sheet application compared to a situation, where a thick sheet is used [6]. The higher sensitivity in thin plates is caused by the stress concentration in the normal plane to the specimen. When the welding toe is large compared to the plate thickness the toe has a considerable influence on the fatigue life [8] and [9]. A reliable estimate of the fatigue life requires that the geometry of the welding toe is taken into account in the design guidelines.

1.2. Material

In the design standards the fatigue assessment guidelines are based on structural steel like S235JR. These types of steel do not show the same tendency in change of the microstructure under the maximum crack length is decreased. However, the crack growth rate is also decreased. The induced strains ahead of a fatigue crack tip can activate a transformation of an austenitic structure to welding process compared to stainless steel. Therefore, we do not expect that the fatigue life calculated based on the standards fit the fatigue life observed in the experiments, where thin sheets of stainless steel AISI304 are tested. In some types of stainless steel including AISI304 the microstructure is changed *i.e.* austenitic phase is transformed into a martensitic phase. This transformation is mainly controlled by plastic strain rates and the tem-

perature [10-12]. In case of low temperatures a higher amount of martensitic phase is generated [13-15]. The martensitic phase is more brittle than the austenitic phase. Therefore, the fracture toughness limit is lower and a martensitic structure [16-20]. Furthermore, this transformation also changes the volume and the expansion of the material can lead to compressive stresses. Hence deformation induced martensitic transformation increases fatigue resistance significantly and the threshold stress intensity decreases. The standard S-N curves for welded structural steel do not include the mean stress because of welding introduced residual stresses. In stainless steel the residual stresses coming from the laser welding process are often more significant compared to standard structural steel. Therefore, the higher compressive stresses in the welding zone can lead to crack propagation resistance [21-23]. However, the tensile stresses in the welding zone are increased accordingly and crack initiations are more probable.

1.3. The Study

In this study the fatigue life of welded and non-welded specimens is investigated experimentally. The welded specimens are produced with the keyhole laser welding method. The results from the experiments are compared to the results from the standards, where the S-N curves are based on structural steel and traditional welding methods. Hence this comparison and possible deviations will reveal if the guidelines for fatigue assessments in the current standards can be safely adopted when stainless steel is considered.

2. Experimental Details

The stainless steel used in the experiments is AISI304 and the sheets have a thickness of 1 mm. The welded specimen is a T-joint welded with the keyhole method by a laser and is shown in **Figure 1**. The concentration of the elements Cr, Ni, S, Mn, Mo, Si and C of the austenitic phase are determined by Electron Probe Micro Analysis. The AISI304 composition is 0.036% C, 0.42% Si, 1.28% Mn, 0.031% P, 0.0010% S, 18.21% Cr, 8.30% Ni.

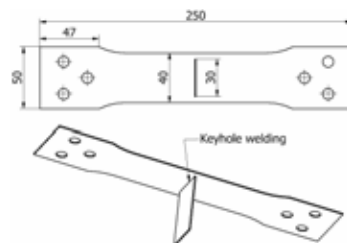


Figure 1. The geometry of the laser welded specimen in AISI 304.

The mechanical properties are $\sigma_{p0.2\%} = 279$ MPa, $\sigma_{p1\%} = 310$ MPa, $\sigma_{UT} = 635$ MPa ultimate strength and 57% elongation. Three different types of specimen are used in the fatigue tests. Two types are non-welded, where one type is cut with a plasma cutter, whereas the other non-welded type is cut with a milling cutter. The third type is a specimen with a transverse welding with respect to the load direction (T-joint). The welding is carried out with a 2 kW NdYAG laser with a speed of 40 mm per second. Argon gas is used to prevent oxidation of the steel. The steel surfaces are smooth with a maximum variation of 0.01 mm. The welded surfaces have a variation around 0.1 mm. A standard servohydraulic Instron 1255 test machine is used. The experiments are load controlled with a constant amplitude sinusoidal wave form with $R = 0.1$ and load frequencies in the interval (2 - 12) Hz. The test is completed when a final fracture occurs. The temperature in the laboratory is in the interval (19°C - 23°C). The geometry is hourglass formed with a design approximation of ASTM E466 and E468. Two different methods have been used to cut out the non-welded specimens. The different defects from this cutting process are observed and the influence on the fatigue life is established. The knowledge about these defects can be transformed to a tolerable defect size for the S-N curve.

In **Figure 2** the non-welded specimen geometry cut by the milling cutter is shown and **Figure 3** shows the geometry cut by the plasma cutter.

The missing data points do to the limit number of sample is estimated with interpolation between the low and high cycle fatigue life.

3. Results

The shape of the welding significantly influences stress concentrations. Thus the shape of the welding is an important factor in the estimation of the fatigue life. A macro photo of the cross section of the welding is shown

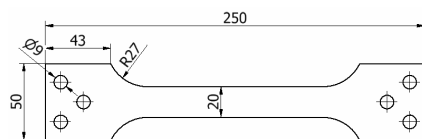


Figure 2. The geometry of the modified non-welded specimens cut out with a milling cutter.

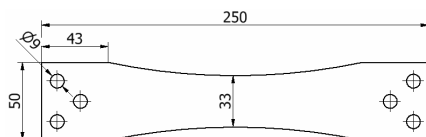


Figure 3. The geometry of the modified non-welded specimens cut out with a plasma cutter.

in **Figure 4**. The welding has clear defects, which introduce high stress concentrations. The shape is like a wedge in the area where the two parts are welded together. A crack most probably initiates at the end of the wedge shape and the fatigue life will be lower compared to a specimen with a smooth welding. No materials are added during the welding process, which explains these clear defects shown in **Figure 4**.

Figure 4 clearly reveals that the shape of the toe is non-smooth at the corner compared to a welding geometry obtained from a traditional welding method. In a standard welding procedure this geometry is not acceptable. However, in many configurations with thin sheets and laser welding's these defects are acceptable because generally these types of welding are exposed to low stress levels. The results of the fatigue test of the non-welded specimens are shown in **Figure 5**.

In the low cycle area the fatigue life is nearly identical for the two specimens. In the high cycle fatigue (HCF) area the specimens cut by the milling cutter tend to show a higher fatigue resistance. The tendency is that the fatigue resistance is low for the specimens cut by plasma compared to the specimens cut by the milling cutter. However, the difference in fatigue life for the two types of specimens is insignificant and it can be assumed that the fatigue life is identical. Furthermore, the S-N curve

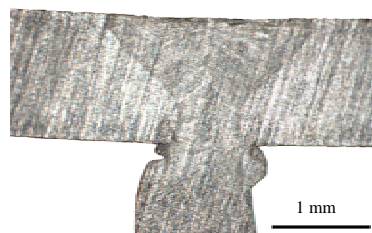


Figure 4. Transverse section view for the keyhole laser welded T-joint.

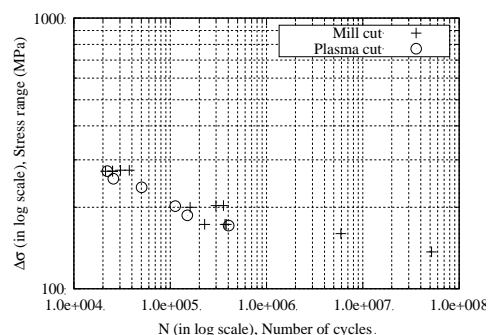


Figure 5. S-N data results of the fatigue life of mill cut and plasma cut non-welded specimens.

clearly shows a knee that starts around 1E06 cycles. The surface on the milling cut specimens is smoother when compared to the surface from the specimens cut by plasma. Generally, a smooth specimen would show a higher fatigue life. However, the results show that the fatigue life is independent of the smoothness of the surface. The heating from the plasma cutting process may affect the surface so that the stress distribution is lower at the surface. The crack initiates at the edge in all the non-welded specimens. In some of the welded specimens the crack initiates at the edge of the specimen and in the major part of the specimens the crack initiates at the welding. In **Figures 6 and 7** the two types of crack initiations are shown.

In **Figure 8** fatigue results from the welded and non-welded specimens are presented.

Clearly the difference in fatigue life is small. In **Figure 9** the fatigue life of the non-welded specimens is

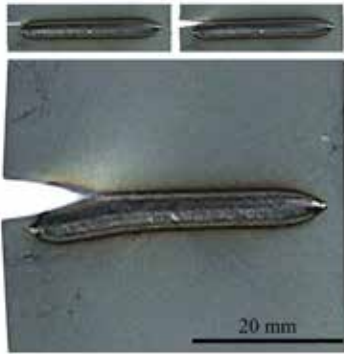


Figure 6. The edge crack growth at the laser welded specimen. The cracks tend to grow in the HAZ Zone.

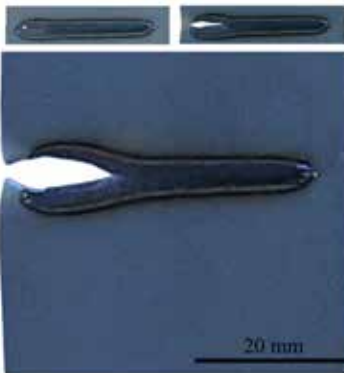


Figure 7. The center crack in the welding at the laser welded specimen. The crack grows in the pre-crack area between the two parts.

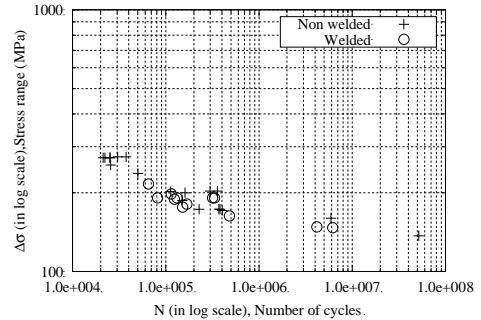


Figure 8. Plot of the fatigue life for the welded and non-welded specimens.

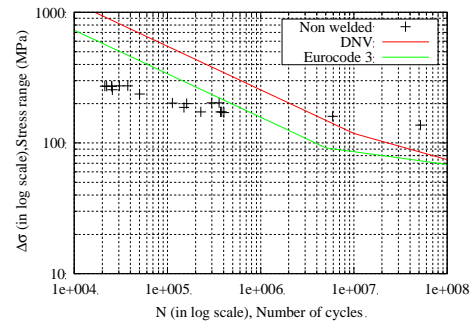


Figure 9. Plot of the fatigue life for the non-welded specimens and the estimated fatigue life based on EUROCODE 3 EN-1993-1-9 and DNV-RP-C203.

compared with the fatigue life calculated on basis of the guidelines in EUROCODE 3 EN-1993-1-9 and DNV RP-C203.

The curves in the DNV RP-C203 standard are associated with a 97.7% probability of survival, whereas the curves in the EUROCODE 3 EN-1993-1-9 standard are associated with a 95% probability of survival. Therefore, the test data should provide higher fatigue strength to compensate for the safety incorporated in the standards. In the calculations according to EUROCODE 3 EN-1993-1-9 (see Equation (1)) the detail category 125 is used, where $m = 3$ below constant amplitude limit at 5.0 1E06 cycles and $m = 5$ up to 5.0 1E08 which is the cut-off limit.

$$\Delta\sigma_R^m N_R = \Delta\sigma_c^m 2 \times 10^6 \quad (1)$$

The calculations with the DNV RP-C203 standard (see Equation (2)) are based on design curve C, where $m = 3$ and $\log(a) = 12.592$ below 1E07 cycles and $m = 5$ and $\log(a) = 16.320$ above 1E07 cycles. The thickness exponent $k = 0.15$ with a reference thickness of 25 mm.

$$\log N = \log a - m \log \left(\Delta\sigma \left(t/t_{ref} \right)^k \right) \quad (2)$$

In **Figure 10** the curve from EUROCODE 3 EN-1993-1-9 is designed from detail category 80, where $m = 3$ below the constant amplitude limit at $5.0 \text{ IE}06$ cycles and $m = 5$ up to $1\text{E}08$ cycles, which is the cut-off limit. The DNV curve is based on design curve E, where $m = 3$ and $\log(a) = 12.01$ below $1\text{E}07$ cycles and $m = 5$ and $\log(a) = 15.35$ above $1\text{E}07$ cycles. The thickness exponent $k = 0.20$ with a reference thickness of 25 mm and a structural stress concentration factor of 1.13.

It is clear from **Figures 9 and 10** that the calculated fatigue life gives a long estimate life at the HCF area. With lower cycles fatigue the fatigue life for the specimens tend to have less resistance to a dynamic load. The negligible difference in fatigue life for the welded and non-welded specimens is most probably caused by local relaxation of the material. The residual stresses from the welding process relax the material by local compression areas and thereby extend the fatigue life. Microstructural transformations can also change the fatigue life. It has been observed that AISI304 can change microstructure from austenite to martensitic and thereby change fatigue and fracture parameters like K_{IC} , K_C and crack growth speed. The residual stress and the microstructure transformation are most probable the source that influence the fatigue life so it is similar for welded and non-welded specimens.

The slope of experimental data and of the design code is not equal. The design code is based on ferritic steel and the material used in the experiments is austenitic stainless steel. In the Stainless steel a considerable amount of chrome and nickel affect the fracture parameter and microstructure. This is the reason for the variation of the slope on the S-N curve.

4. Conclusions

In this paper the experimental investigations of the fatigue life for laser welded T-joints and non-welded

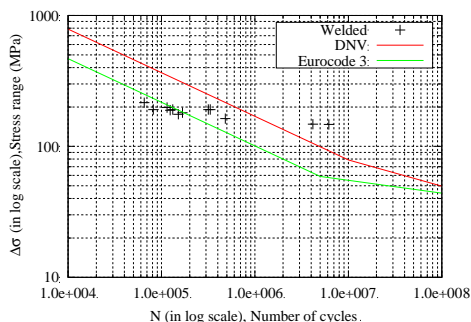


Figure 10. Plot of the fatigue life for the laser welded specimens and the estimated fatigue life based on EUROCODE 3 EN-1993-1-9 and DNV-RP-C203.

specimens made of AISI304 stainless steel are presented. Based on these experimental results the main conclusions are:

- The difference in the fatigue life of a specimen generated by plasma cut or milling cut is insignificant.
- The largest difference in the fatigue life for the plasma and milling cut shows to be in the high cycle fatigue area.
- A comparison between the fatigue life of the welded T-joints specimens and the non-welded specimens shows the tendency that the fatigue resistance is higher for the non-welded specimens.
- The results show that the fatigue life for the welded specimens is lower than the fatigue life estimation based on the standards.

Finally it can be concluded that the fatigue life estimation based on the standards does not satisfy the probability of survival below cycles $4.0 \text{ IE}06$. With cycles above $4.0 \text{ IE}06$ the standards provide lower fatigue life compared to the experiments. In the design standards the fatigue assessment guidelines are based on structural steel like S235JR. Therefore, if these standards are used in the design of stainless steel components only the high cycle fatigue area should be used. Generally, the DNV-RP-C203 standard suggests a higher fatigue life compared to the EUROCODE 3 EN-1993-1-9 standard.

REFERENCES

- [1] I. N. Nawia, Saktiotob, M. Fadhalic, M. S. Hussaind, J. Alie and P. P. Yupapinf, "Nd: YAG Laser Welding of Stainless Steel 304 for Photonics Device Packaging," *Procedia Engineering*, Vol. 8, 2011, pp. 374-379. doi:10.1016/j.proeng.2011.03.069
- [2] G. Apostol, G. Solomon and D. Iordchescu, "Input Parameters Influence on the Residual Stress and Distortions at Laser Welding Using Finite Element Analysis," *Series D: Mechanical Engineering*, Vol. 74, 2012, pp. 153-164.
- [3] B. Alderink, R. Aarts, J. Jonker and J. Meijer, "Experimental Observations of the Laser Keyhole Welding Process of AA5182," *International Conference on Applications of Lasers and Electro-Optics*, Miami, 31 October-3 November 2005, pp. 153-164. <http://doc.utwente.nl/52896/1/Wa1008.pdf>
- [4] K. Balasubramanian, N. Siva Shanmugam, G. Buvana-shekar and K. Sankaranarayanan, "Numerical and Experimental Investigation of Laser Beam Welding of AISI304 Stainless Steel Sheet," *Advances in Production Engineering and Management*, Vol. 3, No. 2, 2008, pp. 93-105. http://maja.uni-mb.si/files/apem/APEM3-2_093-105.pdf
- [5] P. Molian, "Solidification Behaviour of Laser Welded Stainless Steel," *Journal of Materials Science Letters*, Vol. 4, No. 3, 1985 pp. 281-283. doi:10.1007/BF00719791
- [6] M. S. Salleh, M. I. Ramli and S. H. Yahaya, "Study on

- Mechanical Properties and Microstructure Analysis of AISI 304L Stainless Steel Weldments," *Journal of Mechanical Engineering and Technology*, Vol. 3, No. 2, 2011, pp. 71-82.
http://jmet.utem.edu.my/index2.php?option=com_docman&task=doc_view&gid=62&Itemid=40
- [7] C. Suh, M. Suh and N. Hwang, "Growth Behavior of Small Surface Fatigue Cracks in AISI304 Stainless Steel," *Fatigue and Fracture of Engineering Materials and Structures*, Vol. 35, No. 1, 2012, pp. 22-29.
[doi:10.1111/j.1460-2695.2011.01623.x](https://doi.org/10.1111/j.1460-2695.2011.01623.x)
 - [8] J. Linder and A. Melander, "Fatigue Strength of Spot Welded Stainless Sheet Steels Exposed to 3 Percent NaCl Solution," *International Journal of Fatigue*, Vol. 20, No. 5, 1998, pp. 383-388.
[doi:10.1016/S0142-1123\(98\)00009-7](https://doi.org/10.1016/S0142-1123(98)00009-7)
 - [9] F. Karci, R. Kacar and S. Gündüz, "The Effect of Process Parameter on the Properties of Spot Welded Cold Deformed AISI304 Grade Austenitic Stainless Steel," *Journal of Materials Processing Technology*, Vol. 209, No. 8, 2009, pp. 4011-4019.
 - [10] X. Yang, J. Zhou and X. Ling, "Study on Plastic Damage of AISI304 Stainless Steel Induced by Ultrasonic Impact Treatment," *Materials and Design*, Vol. 36, 2012, pp. 477-481.
[doi:10.1016/j.matdes.2011.11.023](https://doi.org/10.1016/j.matdes.2011.11.023)
 - [11] M. C. Park, K. N. Kim, G. S. Shin and S. J. Kim, "Effects of Strain Induced Martensitic Transformation on the Cavitation Erosion Resistance and Incubation Time of Fe-Cr-Ni-C Alloys," *Wear*, Vol. 274-275, 2012, pp. 28-33.
[doi:10.1016/j.wear.2011.08.011](https://doi.org/10.1016/j.wear.2011.08.011)
 - [12] M. Jayaprakash, J. Sumanth Kumar, S. Katakam and S. G. S. Raman, "Effect of Grain Size on Fretting Fatigue Behaviour of Aisi 304 Stainless Steel," *International Symposium of Research Students on Materials Science and Engineering*, Chennai, 20-22 December 2004, pp. 1-8.
<http://mme.iitm.ac.in/isrs/isrs04/cd/content/Papers/MBM/PO-MBM-8.pdf>
 - [13] N. Rossinia, M. Dassistia, K. Benyounisb and A. Olabib, "Methods of Measuring Residual Stresses in Components," *Materials and Design*, Vol. 35, 2012, pp. 572-588.
[doi:10.1016/j.matdes.2011.08.022](https://doi.org/10.1016/j.matdes.2011.08.022)
 - [14] C. Müller-Bollenhagen, M. Zimmermann and H.-J. Christ, "Very High Cycle Fatigue Behavior of Austenitic Stainless Steel and the Effect of Strain-Induced Marten-Site," *International Journal of Fatigue*, Vol. 32, No. 6, 2010, pp. 936-942.
[doi:10.1016/j.ijfatigue.2009.05.007](https://doi.org/10.1016/j.ijfatigue.2009.05.007)
 - [15] O. Takakuwaa, M. Nishikawab and H. Soyama, "Numerical Simulation of the Effects of Residual Stress on the Concentration of Hydrogen around a Crack Tip," *Surface and Coatings Technology*, Vol. 206, No. 11-12, 2012, pp. 2892-2898.
[doi:10.1016/j.surfcoat.2011.12.018](https://doi.org/10.1016/j.surfcoat.2011.12.018)
 - [16] O. Keiji, M. Yoshio and N. Izuru, "Threshold Behavior of Small Fatigue Crack at Notch Root in Type AISI 304 Stainless Steel," *Engineering Fracture Mechanics*, Vol. 25, No. 1, 1986, pp. 31-46.
[doi:10.1016/0013-7944\(86\)90201-8](https://doi.org/10.1016/0013-7944(86)90201-8)
 - [17] M. C. Young, J. Y. Huang and R. C. Kuo, "Corrosion Fatigue Behavior of Cold-Worked 304L Stainless Steel," *Materials Transactions*, Vol. 50, No. 3, 2009, pp. 657-663.
 - [18] M. C. Park, K. N. Kim, G. S. Shin and S. J. Kim, "Effects of Strain Induced Martensitic Transformation on the Cavitation Erosion Resistance and Incubation Time of Fe-Cr-Ni-C Alloys," *Wear*, Vol. 274-275, 2012, pp. 28-33.
[doi:10.1016/j.wear.2011.08.011](https://doi.org/10.1016/j.wear.2011.08.011)
 - [19] L. Singh, R. A. Khan and M. L. Aggarwal, "Influence of Residual Stress on Fatigue Design of AISI 304 Stainless Steel," *The Journal of Engineering Research*, Vol. 8, No. 1, 2011, pp. 44-52.
 - [20] C. Müller-Bollenhagen, M. Zimmermann and H.-J. Christ, "Adjusting the Very High Cycle Fatigue Properties of a Metastable Austenitic Stainless Steel by Means of the Martensite Content," *Procedia Engineering*, Vol. 2, No. 1, 2010, pp. 1663-1672.
 - [21] L. Tsay, Y. Liu, D. Y. Lin and M. Young, "The Use of Laser Surface-Annealed Treatment to Retard Fatigue Crack Growth of Austenitic Stainless Steel," *Materials Science and Engineering*, Vol. 384, No. 1-2, 2004, pp. 177-183.
[doi:10.1016/j.msea.2004.06.010](https://doi.org/10.1016/j.msea.2004.06.010)
 - [22] A. Hascalik, E. Unal and N. Ozdemir, "Fatigue Behaviour of AISI 304 Steel to AISI 4340 Steel Welded by Friction Welding," *Journal of Materials Science*, Vol. 41, No. 11, 2006, pp. 3233-3239.
[doi:10.1007/s10853-005-5478-7](https://doi.org/10.1007/s10853-005-5478-7)
 - [23] Y. C. Chiou, "Experimental Study of Deformation Behavior and Fatigue Life of AISI304 Stainless Steel under an Asymmetric Cyclic Loading," *Journal of Marine Science and Technology*, Vol. 18, No. 1, 2010, pp. 122-129.

Paper D

Investigation of Patch Coatings Influence on the Stress Intensity Factor for Surface Cracks

Søren Heide Lambertsen, Michael S. Jepsen, Lars Damkilde

The paper has been published in the
Proceedings of the 26th Nordic Seminar on Computational Mechanics Vol. 26,
pp. 210–213, 2013.

The layout has been revised.

Investigation of Patch Coating Influence on the Stress Intensity Factor for Surface Cracks

Soren Heide Lambertsen¹, Michael S. Jepsen, Lars Damkilde,

⁽¹⁾Division of Structures and Materials, Aalborg University Esbjerg Denmark, shl@civil.aau.dk

Summary. In this paper, it is investigated how a surface layer of epoxy glue will affect the crack propagation for a surface crack. The idea is that a patch layer will reduce or stop the crack propagation for small surface cracks. When adding a patch layer to the surface with small cracks, the layer will attempt to clamp the free end of the crack. If the layer of coating clamps the free end of the crack a reduction in stress intensity factor will occur. The reduction of the stress intensity factor will consequently reduce the crack growth. The considered patch consists of a surface layer of 0.2mm 3M DP 460 Epoxy two component adhesive. Computing of the stress field distribution around the crack is achieved by finite element. The models contain five crack sizes with a patch layer on the surface. The stress intensity factor is computed by means of the J-integral and the model is setup with a nonlinear material model to establish the upper boundary for the patch stress capacity. Cracks of 3mm and 5mm are rejected due to high stresses in the patch. A reduction of the stress intensity factor about 2 % and a reduction of the crack growth by 5.4-6.1 % for crack sizes 0.5, 1, 2mm.

Key words: Patch repairing, Fatigue life, Stress intensity factor,.

Introduction

Repairing of cracks with reinforced patches is applicable for several types of repairing. The industries mostly use the reinforced patch repairing techniques where replacement of damaged components or failure is not accepted. Frequently the aircraft industry uses the patch repairing method to repair cracks. Cracks which are repaired, will normally be fully developed i.e. these cracks are about 1 mm, and in case of a surface crack it will be visible to the naked eye. The patch repairing technique is able to stop or slow down crack propagation in a damaged component. The major advantage with this technique compared with the hole-drilling method is that no additional stress concentration field is established. The patch repairing technique is therefore straightforward to implement. The patch is usually a composite of epoxy and carbon fibers, where the epoxy connects the carbon fiber to the steel or aluminum structure [1]. The epoxy connects the fiber together, and the fibers add stiffness and strength to the patch. By adding fibers to a fractured area, the patch will unload the crack front. The patch redistributes the stresses in the cracked area. Thus, the crack propagation stops or slows down.

This study investigates how a surface layer of epoxy can affect the stress intensity factor. Adding of a patch layer before adding the original painting will slow down the rate of crack propagation [2]. A patch layer at the surface can reduce the stress intensity factor because the layer will attempt to maintain the crack surface together. The modulus of elasticity of the patch controls the reduction of the stress intensity factor [3]. A limited reduction in stress intensity factor can change the crack growth significantly. Figure 1 shows a coated defect that is loaded past the coating process. Normally coatings modulus of elasticity is much lower than the component material. In such case the coating will elongate and the crack surfaces separate as shown on figure 1. Therefore, will the coating elongate and the crack surfaces separate as shown

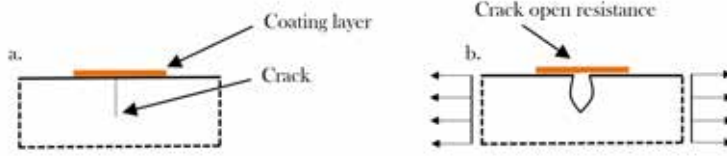


Figure 1. a. Shows a non-loaded surface crack with a layer of coating, b. Illustrates a loaded crack with coating.

on figure 1. The modulus of elasticity controls the separation of the crack surfaces. Ordinary water-based coating has a lower modulus of elasticity than epoxy-based coating. Where the epoxy-based coating also has higher strength. Consequently, it is most beneficial to use epoxy-based coating to take advantage of the higher modulus of elasticity [4]. Higher modulus of elasticity can be achieved by intermix the patch matrix with adding glass or carbon fibers. If the modulus of elasticity is infinite, no separation occur and stress intensity factor is comparable with a center crack. The stress intensity factor for a coating closed edge crack is a combination of the stress intensity factor for an edge crack and a center crack. Identification of the ratio of the patch effect on the stress intensity factor is achieved by divide the stress intensity factor for a center crack and an edge crack. Eq.1 shows the benefit of the stress intensity factor by total closed crack ends.

$$\frac{K_{I\text{Center}}}{K_{I\text{Edge}}} = \frac{\sqrt{1/2}\sigma\sqrt{a\pi}}{1.12\sigma\sqrt{a\pi}} = 0.63 \quad (1)$$

From Eq.1 the effect of the coating patch is compute to a ratio at 0.63. However, the patch is not able to obstruct separation of the free end of the crack. By using FE analysis and J-integral study of the stress intensity factor in a case where the free end of the crack is coated are investigated.

Fatigue Damage Calculation

In this case, the crack propagation is the main parameter for the fatigue damage. Variation in stress intensity factor drives the crack propagation. The stress intensity factor K is a function of the far field stress and the crack size. The stress intensity factor is given in Eq. 2.

$$\Delta K = \Delta\sigma\sqrt{\pi a\alpha} \quad (2)$$

The surface layer influence the α value and thereby the stress intensity factor. However, the stress intensity factor is calculated by J-Integral and thereby α is found. Estimation of the surface layer influence on the crack propagation, a 5 % crack propagation is used. The number of cycles to a specific crack propagates length is calculated with Eq. 3.

$$N_f = \frac{2}{(n-2)A(\Delta\sigma)^n(\pi)^{3/2}\alpha^n} \left[\frac{1}{a_i^{(n-2)/2}} - \frac{1}{a_f^{(n-2)/2}} \right] \quad (3)$$

Where a_i and a_f is the start and stop crack length and $\Delta\sigma$ are the stress variation. The material parameters used in the calculation are $A = 6.9 \cdot 10^{-12} m/cycle$ and $n = 3$.

The Finite Element Method

The study is carried out in Ansys Workbench 14.5 and computes the stress intensity factor for the coated edge cracks. A 2D model is used to determine the coating influence on the stress intensity factor see figure 2. The number of element for the 1mm crack body is 12060 and for the layer is 384 elements. The elements type used in the analysis is PLANE183 higher order 2-D element with 8-nodes. Computing of the stress intensity factor for five crack sizes are present. The crack sizes are 0.5,1,2,3 and 5mm. Adding of the layer happen when the crack is closed. Non-separate or slip will occur in the bonding between the crack surfaces and the coating. In this study, the patch coating material is 3M DP460 has limited strength about of 27.6 MPa. To include the limited strength of the layer in the FE analysis, a nonlinear material model are used. A bilinear material behavior is used and at stress levels above 27.6 MPa and the tangent

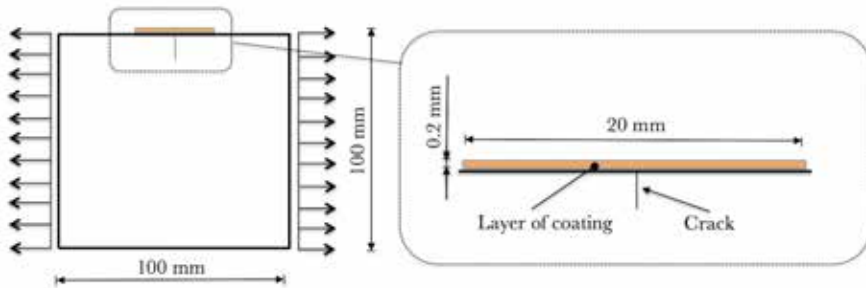


Figure 2. The crack model used for the FE analysis in Ansys Workbench.

modulus is set to 0 MPa. The elastic modulus is set to 2.7 GPa. The coating has a thickness at 0.2mm and is 30 mm wide see figure 2. The far field stress level is a tension stress state at 100 MPa. The plastic behavior is studied in 11 load cycles. The crack part is isotropic elastic material with a young modulus of 200 GPa. The mesh is shown in figure 3. The mesh

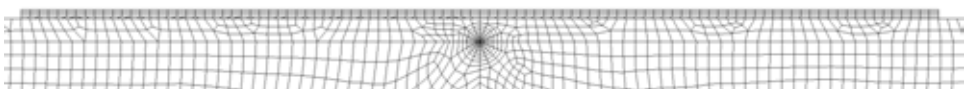


Figure 3. The mesh for the 1 mm crack with a coating layer at the surface.

of the patch layer contains four elements in thickness and the crack have six rings of elements surrounding the crack tip.

Result

Results of the FE solution are shown in table 1. The stress intensity factor has constant amplitudes in cases of a crack size 0.5,1 and 2 mm. In the following load cycles, the stress intensity factor is almost stable, and the changes are insignificant. Introduced of plastic strain into the layer is indicated by the behavior of the analysis. In the calculations with crack sizes at 3mm and 5mm, the stress intensity factor changes for every load cycle. Special in the first three load cycles the changes are significant. The strain level in the layer exceeds the elastic limit at 27.6 MPa. Then irreversible strain occur in the layer and loses its effect on the stress intensity factor. Therefore is calculations of the 3mm and 5mm crack rejected. The results of crack size 0.5, 1 and 2 mm shows a reduction in stress intensity factor at 1.7-2.0 %. The number of cycles to

Table 1. Result of the stress intensity factor with and without layer of coating on the surface.

Crack Size Coating Method	0.5mm	1mm	2mm	3mm	5mm
Coated	137.7	194.9	276.8	340.8-341	446.3-446.5
Non-coating	140.2	198.8	281.7	346.1	450.0
% changes stress intensity	1.8	2.0	1.7	1.5	0.8

Table 2. Result of changes in number of cycles with and without layer of coating on the surface.

Crack Size	0.5mm	1mm	2mm
α coated	1.0985	1.0996	1.1041
α non-coated	1.1184	1.1217	1.1237
Life coated	777614	387641	191460
Life non-coated	736840	365177	181615
% changes life	5.5	6.1	5.4

propagate the cracks 5% is calculated, and the result is shown in table 2. In case of a 1 mm crack, the number of cycles is increased by 22464 cycles or 6.1%. The α changes from 1.12 to about 1.1 in cases of a surface layer. However it is clear that the surface layer changes the stress intensity factors and thereby the α parameter.

Conclusion

The investigation shows that the potential is marginal due to the low elastic strength and low modulus of elasticity of the surface layer. However, cracks over 2 mm have local plastic strains in the surface layer. Therefore, is the crack size over 2 mm rejected. It is computed that the surface layer changes the stress intensity factor by 1.7-2 %. The changes for a crack to propagate 5% of the original length are calculated. It shows that the surface layer changes the number of cycles for the crack to grow by 5.4-6.1 %. It is concluded that the use of pure epoxy as surface repairing method is not beneficial.

References

- [1] Woo-Yong Leea, Jung-Ju Leeb, Successive 3D FE analysis technique for characterization of fatigue crack growth behavior in composite-repaired aluminum plate,
- [2] Dae-Cheol Seo, Jung-Ju Lee. Fatigue crack growth behavior of cracked aluminum plate repaired with composite patch, *Composite Structures*, Volume 57 Issues 1-4 July 2002 Pages 323-330.
- [3] S. Naboulsi, S. Mall Characterization of fatigue crack growth in aluminium panels with a bonded composite patch, *Composite Structures*, Volume 37 Issues 3-4 March-April 1997 Pages 321-334
- [4] Yaowen Yang, Bahador Sabet Divsholi, Lihua Tang, and Lei Zhang, Strain Transfer Models for Macrofiber-Composite Strain Actuators, *Materials and Manufacturing Processes*, Volume 25, 237-242, 2010

RESUMÉ

Denne afhandling omhandler udmattelse og revnemekanik i materialer og svejsninger. I selve afhandlingen gennemgås revne- og udmattelsesfænomener, og der refereres til den udførte forskning i forbindelse med Ph.D.-forløbet.

Afhandlingen omhandler overordnet set fire emner; henholdsvis 1) udmattelsesanalyse af kobberør (CuNi10), 2) udmattelsesanalyse af svejste T-samlinger konstrueret i rustfrit stål (AISI 304), 3) metallurgiske undersøgelser af de førnævnte T-samlinger og 4) undersøgelser af brugen af coating som revneforsinkelseslag for stål- og aluminiumsstrukturer. Ydermere behandles brugen af numeriske metoder, i form af finite element-analyse (FEA), til at estimere korttidsudmattelse i overensstemmelse med den nyeste norm DNV-RP-C208. Det sidstnævnte er medtaget, eftersom forfatteren af indeværende afhandling har været involveret i udviklingen af denne specifikke DNV-norm.